3-12-2009

# Laser Dot Projection Photogrammetry and Force Balance Measurement Techniques for Flapping Wing Micro Air Vehicles

David H. Curtis


# LASER DOT PROJECTION PHOTOGRAMMETRY AND FORCE MEASUREMENT FOR FLAPPING WING MICRO AIR VEHICLES

THESIS

David H. Curtis, First Lieutenant, USAF

AFIT/GAE/ENY/09-M05

**DEPARTMENT OF THE AIR FORCE**
**AIR UNIVERSITY**
***AIR FORCE INSTITUTE OF TECHNOLOGY***

**Wright-Patterson Air Force Base, Ohio**

The views expressed in this Graduate Research Project are those of the author and do not reflect the official policy or position of the United States Air Force, Department of Defense, or the U.S. Government.

AFIT/GAE/ENY/09-M05

# LASER DOT PROJECTION PHOTOGRAMMETRY AND FORCE BALANCE MEASUREMENT TECHNIQUES FOR FLAPPING WING MICRO AIR VEHICLES

THESIS

Presented to the Faculty

Department of Aeronautical and Astronautical Engineering

Graduate School of Engineering and Management

Air Force Institute of Technology

Air University

Air Education and Training Command

In Partial Fulfillment of the Requirements for the

Degree of Master of Science in Aeronautical Engineering

David H. Curtis

First Lieutenant, USAF

March 2009

AFIT/GAE/ENY/09-M05

# LASER DOT PROJECTION PHOTOGRAMMETRY AND FORCE MEASUREMENT FOR FLAPPING WING MICRO AIR VEHICLES

David H. Curtis
First Lieutenant, USAF

Approved:

| | |
|---|---|
| _____//SIGNED//_____ | 12 March 2009 |
| Reeder, Mark F., Civ AFIT/ENY (Chairman) | Date |
| _____//SIGNED//_____ | 12 March 2009 |
| Cobb, Richard G., Civ AFIT/ENY (Member) | Date |
| _____//SIGNED//_____ | 12 March 2009 |
| Palazotto, Anthony N., Civ AFIT/ENY (Member) | Date |

## Abstract

The purpose of this research was to develop testing methods capable of analyzing the performance of a miniature flapping wing mechanism that can later be adapted to a flapping wing micro air vehicle (MAV). A previously designed and built flapping only mechanism was used for testing, while a previously designed flapping and pitch mechanism was fabricated utilizing an Objet Eden 500V 3-dimensional printer and its operation demonstrated. The flapping mechanism was mounted on a six component force balance. Force and moment data were collected for a variety of wing sets at different flapping frequencies. The testing was conducted using wings composed of aluminum tubing and/or stainless steel wire for frame material, and thin latex as membrane material. The normal and axial force averages were taken with the force balance and compared. The axial force measurement was verified using an air bearing table and a load cell as a secondary means of measurement. Time accurate force data was also taken. A non-intrusive photogrammetry method using laser dot projection was developed allowing for the shape of the wing during flapping to be measured. The result was that approximately 98 data points representing wing shape and orientation were collected at 1000 Hz. Comparisons were made between laser dot projection photogrammetry and a more a traditional method using potentially intrusive marked targets for photogrammetry, with good correspondence. Differences in force data were then analyzed with the insight gained regarding wing shape. This research demonstrates

the capability to study the forces and moments involved in flapping flight as well as shape changing of wings during flapping flight.

## Acknowledgements

I would like to thank my advisor Dr. Mark Reeder for his guidance in every aspect of this research, as well as Maj Greg Parker at his team at Air Force Research Labs for their support. I would also like to thank Dr. Richard Cobb, Dr. Jonathan Black, and Dr. Roberto Albertani for their valuable insight. The lab technicians at the Air Force Institute of Technology provided invaluable assistance in this research, particularly John Hixenbaugh and Chris Zickefoose. Finally I would like to thank my wife Sara for her support.

## Table of Contents

## List of Figures

Page

Page

Page

## List of Tables

BIOMIMETIC MICRO AIR VEHICLE TESTING DEVELOPMENT

AND SMALL SCALE FLAPPING-WING ANALYSIS

# 1. Introduction

## 1.1 Motivation

Birds and insects are the original masters of flight; it has been only in the last century that man has successfully ventured into the air. Over the past century, man has pushed some of the boundaries of flight well past anything that natural flyers are capable of, yet there are certain areas within the flight envelope in which birds and insects still have the upper hand. In the past, size has been the major limitation, but as the size of sensors and electronics shrinks, and the capabilities in micro-manufacturing increase, the flight regime currently dominated by small natural flyers is within reach and therefore is of greater interest.

Micro Air Vehicles (MAV) is the term that has been given to air vehicles in this flight regime. According to DARPA, MAVs are smaller than 15 cm in their largest dimension and are "affordable, fully functional, militarily capable, small flight vehicles in a class of their own" (McMichael, 1997). Others have suggested that MAVs must have a maximum weight of 100 grams (Ho and others, 2003). The Air Force Institute of Technology (AFIT) is working with Air Force Research Labs (AFRL) to develop a fully functional MAV analysis and development center.

The uses of such vehicles are endless, particularly as the size of all types of sensors decreases. Releasing a flock of MAVs equipped with cameras could provide a valuable tool for providing real-time battlefield intelligence to both soldiers in the fight and to operational commanders. MAVs, equipped with listening and imaging devices, disguised as insects or birds could infiltrate enemy headquarters and send back valuable information (AFRL Air Vehicles Directorate, 2008).

The small scale and slow speed of flight requires an entirely new approach to vehicle design. With the exception of helicopters, flight over the past century has been accomplished primarily by separating the task of producing lift from the task of producing thrust. Jet or propeller engines produce thrust which pushes the aircraft through the air. The motion of the air over the wings produces lift. Natural flyers use flapping wings to produce both lift and thrust.

Hover is a requirement of many MAV missions. This requirement drives selection of either rotary wing MAVs or flapping wing MAVs. Rotary wing MAVs are known to have decreases in efficiency and ability to tolerate wind gusts as scale decreases (Svanberg, 2008). Flapping flight has been shown to be beneficial at the low Reynolds numbers ($10^4$-$10^5$) that correspond to small scale and low velocity (Ho and others, 2003). Further research into the dynamics of flapping flight in the unsteady region is crucial to the development of practical MAVs. These MAVs must be capable of forward flight, as well as hover. As hovering flight is both the most challenging to achieve, and the easiest to simulate, it is often the starting point of research into flapping flight.

Studies have shown that for both birds and insects, the shape of the wing often changes throughout the stroke. Birds do this through actuation of the internal skeleton in

the wing, while insects only actuate the wing at the wing root and often rely on the inherent flexibility of their wings to produce beneficial deformation (Ansari, Zbikowski, and Knowles, 2006b; Combes and Daniel, 2003:2999). Some studies have demonstrated a benefit for lift and thrust production in flapping wings due to flexibility (Ho and others, 2003). In order to design wings that will produce an optimal shape through deformation during flapping, there must be a method of measuring the shape of the wing during flapping.

One way to assess the overall effectiveness of a flapping mechanism, and its wings, is often quantified by the amount of average lift and thrust it can produce throughout its stroke per unit of input power. These values can be used to optimize mechanism design, wing design, and even stroke profile to meet the lift and thrust requirements for flight. Time-accurate force and moment data for the mechanism are required to better understand what is occurring within the wing stroke.

Flapping wing MAVs have endless potential. To unleash that potential, more research is needed to gain a better understanding of the dynamics of flapping flight. To facilitate this research, test methods must be developed that can be used to experiment with different aspects of the problem.

## 1.2 Research Focus and Goals

The purpose of this research was to assist AFRL in developing a bench test set-up which could be utilized to analyze and develop MAVs. A method was to be developed for taking measurements of the forces and moments associated with the flapping motion of a test mechanism utilizing a six component force balance. A high speed camera

system was used to capture images of a flapping wing throughout its stroke, and a non-intrusive technique was developed for measuring the shape and location of the wing throughout flapping.

The first step was to mount the flapping mechanism to a six component strain gauge based force balance. A LabView program had to be developed to read the voltage from each of the six channels of the force balance. Post processing scripts also needed to be developed to convert the voltage data into force and moment data. Force data was analyzed both as a time average for continuous flapping at a given frequency and temporally throughout a stroke. A linear air bearing table and load cell was to be used to validate the axial force average measured by the force balance.

The second component of this research was to develop laser dot projection photogrammetry. Placing a grid of target dots on a wing and recording high speed images during flapping gives a method of measuring the shape of the wing through photogrammetry. By using lasers dots as targets, the change in mass properties of the wing inherent with the use of traditional target marking methods is avoided.

# 2. Literature Review

## 2.1 Natural Flyers

Flying animals, such as birds, bats, and insects, represent examples of functional flapping wing flight. These animals have had to master flight for their own survival, and in doing so have given us a blueprint for how to achieve effective flight with flapping wing MAVs. Hovering flight of diptera, or two winged flies, is considered by S. A. Ansari, Zbikowski, and Knowles (Ansari, Zbikowski, and Knowles, 2006a). In hover, it is shown that flies flap their wings in a figure eight pattern, with the leading edge always constant, meaning that throughout the flapping stroke the wing pitches so that the same edge of the wing is always leading the wing through the air.

Figure 1 shows the path of the wing tip throughout a stroke. According to Ellington, the wing speed is not constant throughout the stroke; the wing quickly accelerates at the beginning of the halfstroke and decelerates at the end of the halfstroke with constant speed during the midstroke in between (Ellington, 1984).

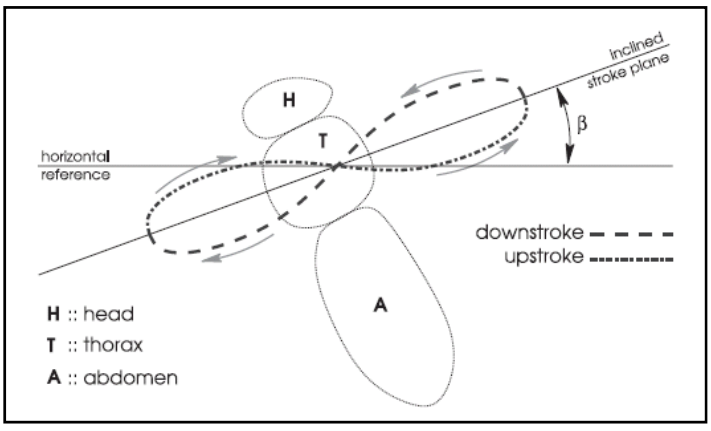


**Figure 1: Insect Wingtip Motion (Ansari, Zbikowski, and Knowles, 2006a)**

When looking at a large bird soaring through the air, one would notice that it rarely flaps its wings. This would suggest that there are certain regions of flight in which flapping is most efficient, and certain regions in which soaring, which is essentially fixed wing flight, is most efficient. Consequently, for natural flyers the wingspan cut-off between these two methods of flight is approximately 15 cm, the same dimension assigned as the maximum wingspan for MAVs (Ho and others, 2003). Traditional aerodynamics attempts to describe quasi-steady flow, while Ho and others prescribe that the nature of most flapping flight is inherently unsteady in nature. To help quantify the degree of unsteadiness in flapping flight, the authors used the advance ratio (J).

$$J = \frac{U}{2\Phi f b} \tag{1}$$

Where U is the forward velocity, Φ is the total flapping angle in radians, *f* is the flapping frequency, and *b* is the wing span. The cut-off region between flight in the unsteady region and flight in the quasi-steady region is determined to be approximately at an advance ratio of one. Values of J < 1 are in the unsteady flow region while values of J > 1 are in the quasi-steady flow region (Ho and others, 2003).

Ellington looks at insect flight, particularly those insects utilizing only one set of flapping wings. Insect flapping frequencies and wing area have been found to be tied to the insects mass in the following way (Dudley, 2000):

$$S \propto mass^{2/3} \tag{2}$$

$$f \propto mass^{-1/4} \tag{3}$$

Where S is the wing area and f is the wing beat frequency. Although not all insects follow this pattern directly, there is a trend that suggests these relationships would be a good starting point for flapping wing MAV design. As with other types of flight, an

important parameter is the Reynolds number. Ellington defined the Reynolds number for hovering flapping flight using the following equation:

$$Re = \frac{\bar{c}\bar{U}_T}{\nu} = \frac{4\Phi nR^2}{\nu AR} \quad (4)$$

where

$\bar{c}$ = 2R/AR = mean chord

$\overline{U_t}$ = 2ΦnR = mean wing tip velocity

R = b/2 = wing length

AR = Aspect Ratio

Φ = Wing beat amplitude in radians

n = flapping frequency

ν = viscosity

The primary axis in which the wings are flapped is called the stroke plane. The stroke plane is perpendicular to the primary aerodynamic force, which for hovering flight is lift, therefore during hovering flight the stroke plane is horizontal. The flight of a bumblebee was studied, and it was determined that while in hover, the wing rotates through approximately $120^o$ between half-strokes, causing the leading edge to remain constant. The flexibility of most insect wings causes twisting that gives the root of the wing an effective angle of attack of $10^o$ to $20^o$ greater than the tip. Insect maneuverability and control is achieved through a combination of adjusting the stroke plane, adjusting the center of gravity, and adjusting the frequency and amplitude of flapping each individual wing (Ellington, 1999). How an insect adjusts other parts of its body during flight was investigated by Chakravarthy and others, and will be discussed in more detail in section 2.6.

## 2.2 Flapping Mechanisms

There have been many attempts to mimic the flapping motion used by natural flyers. There are three primary degrees of freedom associated with flapping wings. In-plane motion is the motion in the stroke plane, and is perpendicular to the direction of flight. Out-of-plane motion is the motion perpendicular to the stroke plane and pitching motion is twisting of the wing along its primary axis. Banala and Agrawal at the University of Delaware created a mechanism that is capable of all three degrees-of-motion. It utilized a five bar mechanism for both the in-plane and out-of-plane motion, and a four bar mechanism for the twisting motion. This allows the mechanism to produce the figure-eight wing tip pattern that insects are known to exhibit in flight. A picture of the mechanism is shown in Figure 2 (Banala and Agrawal, 2005).

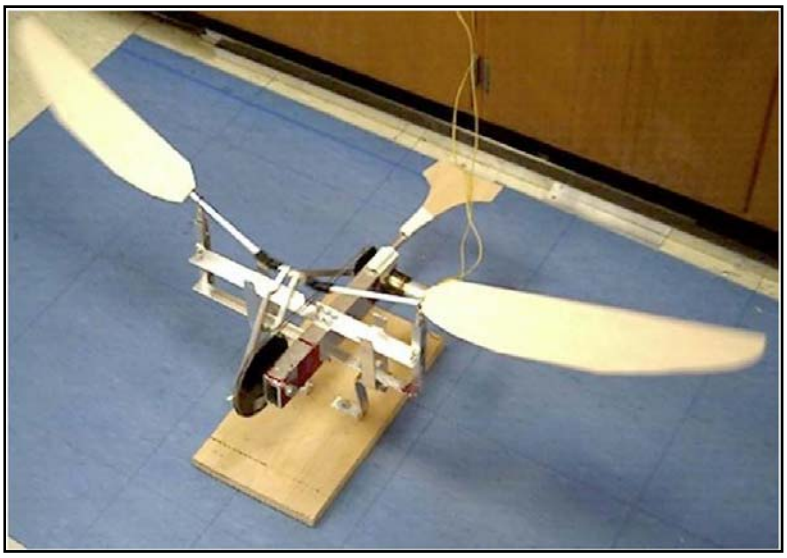

**Figure 2: University of Delaware Mechanism (Banala and Agrawal, 2005)**

Other researchers have achieved pitching motion through the use of servomotors located in-line with the wing. An encoder was linked to the servo such that the pitch

angle would be reversed at the end of each halfstroke. This forced the angle of attack to be such that thrust was produced during both the upstroke and the downstroke. A strain gauge force transducer was also mounted in-line with the servomotor and the wing. The force transducer measured the force normal to the surface of the wing at all time. This flapping mechanism was setup for flapping in a water tank. It was suggested that inertial and gravitational loading on the force transducer could be determined from numerical analysis or by conducting identical experimentation in air. A drawing of the mechanism is shown in Figure 3 (Isaac, Colozza, and Rowles, 2006).

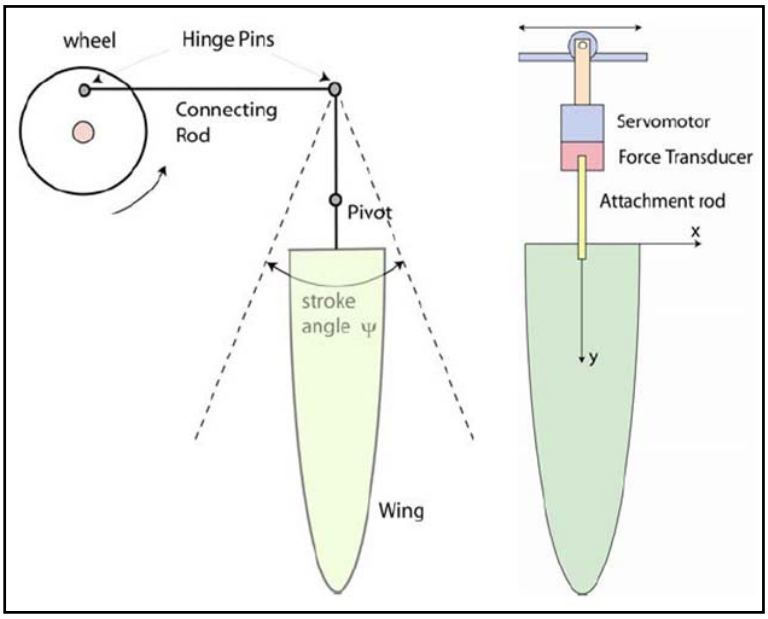


**Figure 3: University of Missouri Mechanism (Isaac, Colozza, and Rowles, 2006)**

Another mechanism was developed at Cranfield University. This mechanism was designed to provide figure-eight tip motion along with pitching, particularly rapid pitch reversal at the top and bottom of the stroke. This was accomplished with a mechanism that utilized three distinct parts, a four-bar mechanism for figure-eight generation, wing articulations to transfer motion to the wings, and a Geneva wheel for

rapid pitch reversal at the halfstrokes. A Geneva wheel is a mechanical device used to produce rotary motion of a particular angle from each rotation of constant rotary motion. This is precisely what is needed for rapid pitch reversal at the halfstrokes. The mechanism was capable of +/- 45$^{o}$ of sweeping motion, and successfully achieved rapid pitch reversal at the top and bottom of the stroke. A diagram of the workings of the mechanism is shown in Figure 4 (Zbikowski, Galinski, and Pedersen, 2005).

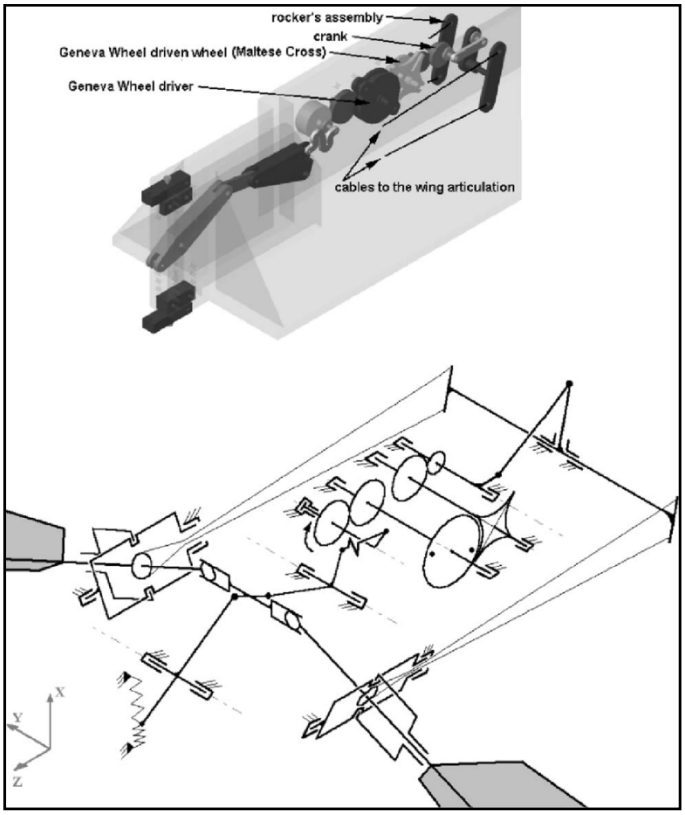


**Figure 4: Four Bar Linkage Mechanism (Zbikowski, Galinski, and Pedersen, 2005)**

## 2.3 Wing Design

Ellington suggests that wings should incorporate twist from the root to the tip, and this twist must be reversed during the half stroke. He suggests that preliminary flapping

wing vehicles should consist of "simple sail-like construction", with a stiff leading edge, a chordwise support member at the root of the wing, and a membrane connected to them (Ellington, 1999). Wilson and Wereley used these principles to construct the wings shown in Figure 5. They used the following equation from Ellington, along with design goals to determine the wing length, R, to be 10 cm.

$$m = 0.387 \frac{\Phi^2 n^2 R^4 C_L}{AR} \quad (5)$$

The variables in Equation 5 are the same as in Equation 4 with the added variable $C_L$ representing the lift coefficient. The span to chord ratio for each individual wing was taken to be 2.5:1 as is common for insects. Wing frames were constructed with carbon fiber rods, while tissue paper was used for the membrane and was attached to the frame using epoxy. Stiffness of the wing varied based on the thickness of the carbon fiber used as well as the frame design. His experimentation with these wings concluded that wings IV and V had the best aerodynamic performance (Wilson and Wereley, 2007).

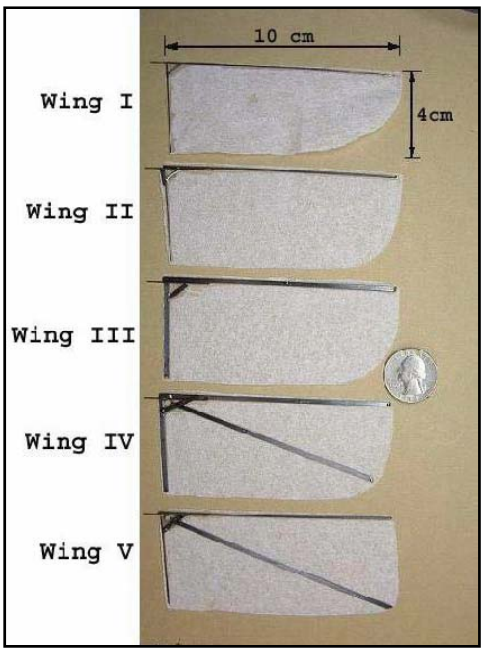


**Figure 5: Carbon Fiber frame Wings used by Wilson and Wereley (Wilson and Wereley, 2007)**

The effect of flexibility on thrust production for flapping wings was studied by Heathcote, Martin, and Gursul. Steel plates of varying thicknesses were attached to an airfoil and oscillated in a water tank. The results showed an increase in thrust production for the flexible plate. Images of the flapping showed that there was a phase lag between the leading edge and the trailing edge. This phase lag is essentially equivalent to a pitching motion, effectively causing a negative pitch during the downstroke, and a positive pitch during the upstroke, which allowed for thrust production throughout the stroke (Heathcote, Martin, and Gursul, 2004).

Ho and others studied the effect of leading edge flexibility on lift production. They found that for the *cicada* type wings tested, flexibility of the leading edge diminished lift production in the unsteady region at which flapping wings are beneficial. The results and the wings used are shown in Figure 6. This is likely due to the disruption

of the leading edge vortex caused by the constant deformation of the leading edge (Ho and others, 2003).

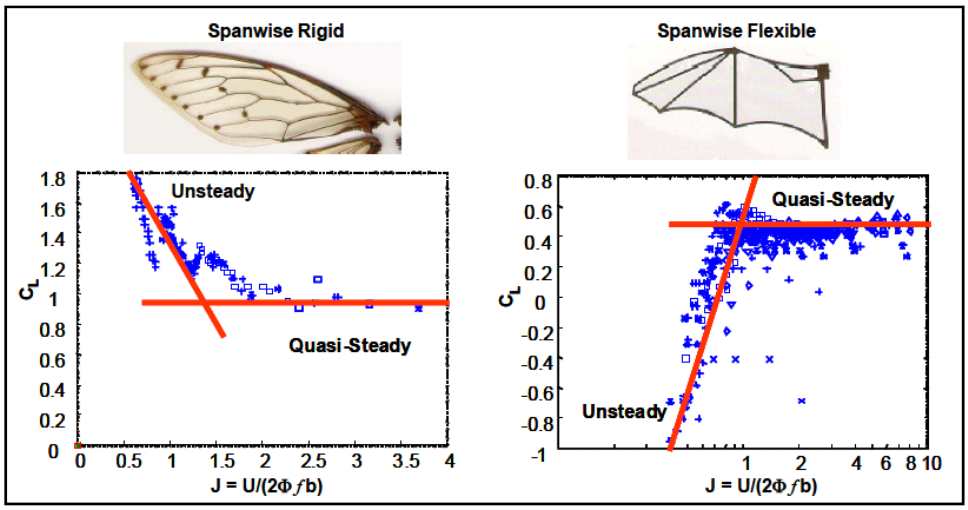


**Figure 6: Effect of Leading Edge Flexibility (Ho and others, 2003)**

They also studied the effect of flexibility on thrust production by comparing thrust production from wings with identical frames but with membranes of different flexibility. The mylar membrane wing was more flexible then the paper membrane wing, and produced a higher thrust coefficient, particularly as the advance ratio decreased toward hovering flight. Overall results demonstrate the advantages flexibility in flapping wings can provide when applied properly (Ho and others, 2003).

The effect of spanwise camber in flapping wings was investigated by Hong and Altman. Digital Particle Image Velocimetry was done on the flow field around a flapping flat plate wing, as well as a flapping wing with spanwise camber. The forces and the velocity of the air above and below the wing were measured throughout the stroke. It was determined that for the cambered wing more lift was produced during the downstroke, than negative lift was produced during the upstroke, resulting in a net lifting

force greater than for a flat plate. The greatest difference in lift between the uncambered wing and the cambered wing was during the downstroke. It was found that the cambered wing produces more force during the first half of the downstroke, while the uncambered produces more force on the second half of the downstroke (Hong and Altman, 2006).

Hu and others used a force-moment sensor cell mounted underneath the flapping mechanism to study the effects of wing flexibility in flapping and gliding flight. The force-moment sensor cell is capable of measuring forces in all three orthogonal directions as well as the torques, or moments, about these directions. They sampled data for 60 seconds at 1,000 Hz for each experiment run. Lift and thrust time averaged values were determined from the measurements. Data was taken for a wooden membrane wing (rigid), a nylon membrane wing (flexible), and a latex membrane wing (most flexible). The schematic of the three different wings tested is shown in Figure 7. All three wings have identical rigid graphite frames. Results showed comparable forces for all three wings at low speed and low angle of attack ($<10^{o}$). Higher orientation angles resulted in higher lift and drag coefficients for the flexible wings, but a nearly constant lift to drag ratio. At higher freestream velocities, approximately 8 m/s, the overall aerodynamic performance was higher for the flexible wing then for the rigid wing. During flapping flight the flexible wings produced more thrust than the rigid wings. At higher flight speeds, flapping did not produce enough thrust to counteract drag, resulting in overall net drag, particularly at high flapping frequencies. Results again show that the benefit of flapping flight is predominantly in the unsteady regime. Flexibility was shown to be beneficial to lift and thrust production for advance ratios of less than approximately 0.5 (Hu, Kumar, Abate, and Albertani, 2009).

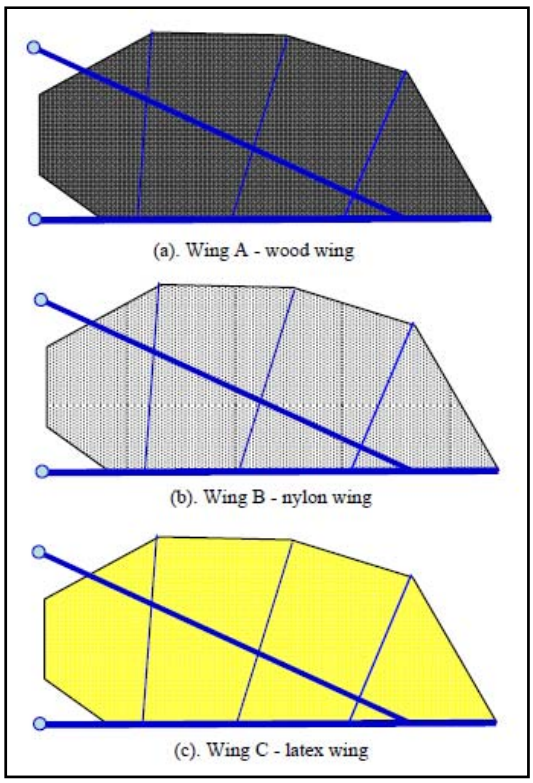


**Figure 7: Effects of Membrane Flexibility (Hu, Kumar, Abate, and Albertani, 2009)**

## 2.4 Force Measurement

Force measurement for flapping wing vehicles has traditionally been done with force cells that utilize a strain gauge. A strain gauge typically utilizes an electrical circuit called a Wheatstone bridge. A Wheatstone bridge allows precise measurement of the resistance of one of its legs. Changing the cross-sectional area of a wire changes the electrical resistance of the wire. When a force is applied to the wire, strain, or a stretching of the wire, occurs. In general, within the elastic region, the stress applied can be determined by multiplying the strain by the modulus of elasticity of the wire. The geometry of the resistor can then be used to determine the forces that caused the strain, or elongation. The elongation produces a change in cross-sectional area, and therefore a

change in resistance. This resistance can then be measured as a voltage through use of the Wheatstone bridge.

Wilson and Wereley used load cells that utilized strain gauges in their experiments to measure flapping wing lift. They directly applied the load cell to the root of the wing in such a way as to measure the lifting force produced by the wing as shown in Figure 8. Since the wing was mounted vertically, the lifting force in these experiments is perpendicular to the stroke plane. Force data was taken over the entire cycle and averaged to give the overall lift at a given frequency (Wilson and Wereley, 2007).

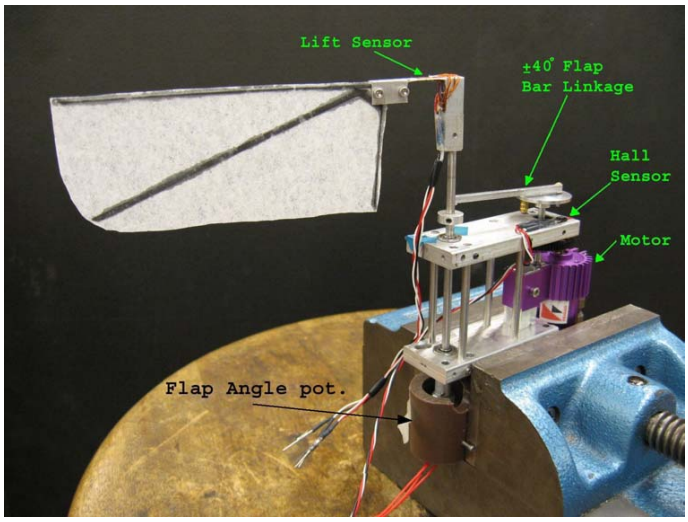


**Figure 8: Force Measurement Set-Up with Strain Gauge at Wing Root (Wilson and Wereley, 2007)**

Singh and Chopra utilized a similar technique to measure the aerodynamic and inertial loads with strain gauges. They set up the strain gauges along the root of the wing so that the two orthogonal bending moments could be sensed. With this method they were able to determine the forces that were acting on the wing in the directions normal and tangential to the wing chord throughout the stroke. In order to translate this data into a more useful coordinate frame, or in terms of lift and thrust, they used Hall effect

sensors and tapered magnets. The Hall sensors have an output that depends on magnetic field strength. The tapered magnets passing through the sensor allowed the angle of rotation of the pitch axis as well as the flapping motion of the mechanism to be measured. The data from the Hall effect sensors yielded time accurate position data on the wing, which could then be differentiated to determine wing velocity. Meaningful relationships between the measured forces and velocity of the wing could then be examined (Singh and Chopra, 2006).

Jadhav and Massey, at the Georgia Institute of Technology, used a different approach to force measurement. They used a test setup in which forces were calculated through the measurement of motion. A simple flapping mechanism utilizing in-plane flapping and passive pitch motion was devised and mounted to a vertical aluminum rod with two linear bearings, allowing the device to slide up and down the rod freely. The mechanism was then suspended in place with springs. This entire setup was mounted on a linear air bearing that would allow free motion in the x-direction, again the system was constrained in the x-direction using springs. Position transducers were used to sense movement in the vertical and horizontal direction. The forces that the mechanism produced during flapping were then calculated by applying the spring constants to the displacement data. The set-up is shown in Figure 9. Flexible wings with a carbon-fiber frame and a thin membrane made of two sheets of fiberglass, each 0.0025 in thick, were created to mimic bat wings. Inertial effects were determined and subtracted out of the results by gathering flapping data using aluminum rod wings with the same mass properties, but with no membrane. A high speed camera system was synchronized to the data acquisition system so that position data could be accurately compared to the

resulting force data. The flexibility of the wing was evident in the results. The tip of the wing was shown to lag the root by over 60$^{o}$ at the center of the upstroke. As anticipated, the design of the mechanism allowed for passive pitching motion throughout the stroke (Jadhav and Massey, 2006).

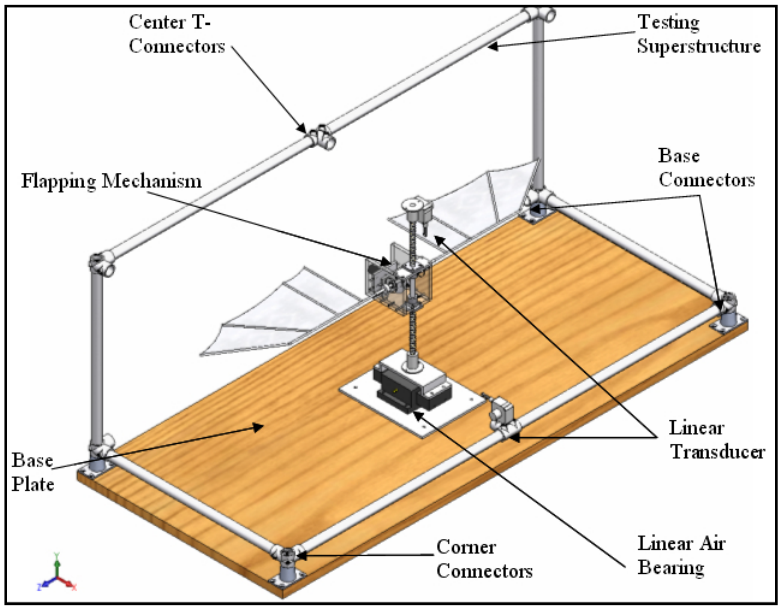


**Figure 9: Set-up for Force Measurement through Position Sensing (Jadhav and Massey, 2006)**

A six component strain gauge based force balance was used by Shkarayev and Silin to measure the forces associated with a flapping wing MAV in a wind tunnel. Force measurements at different advance ratios, and dihedral angles were taken. The normal force was defined as the force parallel to the stroke plane and thrust was defined as perpendicular to the stroke plane. These forces were determined by averaging the force balance measurements over time. The dihedral angle is the angle between the horizontal and the center of the flapping stroke. It was found that a dihedral angle was required for the production of normal force, and that an overall increase in dihedral provided benefit

to both normal force and thrust. The stroke plane angle, essentially the angle of attack, was also varied. Although lifting force does trail off when stroke plane angle approaching $90^{o}$, the flapping wing mechanism did not exhibit a point of abrupt stall as is the case with fixed wing flight (Shkarayev and Silin, 2009).

## 2.5 Force Separation

Wing deformation during flapping flight occurs in both natural flyers as well as man-made flapping mechanisms. Often this wing deformation is significant enough to drastically affect the aerodynamics of the wing. Therefore, in order to create an accurate model of the wing throughout the flapping stroke, the deformation of the wing must be analyzed. To properly model the deformation of the wing, the reason for the deformation must be determined. There are two primary forces acting on the wing that could cause its deformation, aerodynamic forces, caused by the air, and inertial forces, caused by the acceleration of the wing's mass. If the aerodynamics of the wing are the primary forces causing deformation, then any model must calculate the aerodynamic forces and the deformation continuously through the simulation time steps. If the inertial forces are primary, then the deformation of the wing throughout the stroke can be determined separately from the aerodynamics and simply applied to the model (Combes and Daniel, 2003).

Combes and Daniel conducted an experiment at the University of Washington to try to determine which of these two forces dominate. They created a chamber in which they could replace the air with helium, thereby reducing the density inside the chamber. A hawkmoth wing was flapped, and forces were measured both in air and in the helium

filled chamber. Deformation measurements from the atmospheric tests and the helium filled chamber testes were comparable which suggests that the contribution to wing deformation by inertial loading is significantly greater then contributions from aerodynamic loading (Combes and Daniel, 2003).

Wilson and Wereley also did some interesting work to separate the inertial from the aerodynamic force for flapping wings. Their work utilized a 16' diameter cylindrical acrylic vacuum chamber which they pulled down to 27 in Hg, or about a 90% vacuum. Figure 10 shows their test setup (Wilson and Wereley, 2007).

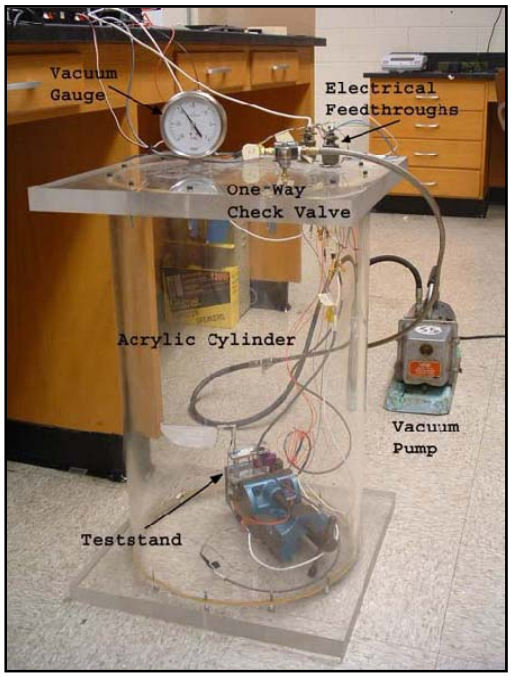


**Figure 10: Vacuum Chamber for Separating Inertial and Aerodynamic Forces (Wilson and Wereley, 2007)**

Singh and Chopra utilized the same vacuum chamber to determine the inertial loads on flapping wing experiments. Their mechanism utilized a sensorless speed controller to adjust the power given to the motor, and therefore to adjust the flapping

frequency of the mechanism. Less power is needed for flapping in the vacuum so the voltage had to be adjusted from the level used in the free atmosphere tests in order to obtain the same flapping frequency. The measured forces from the vacuum chamber experiment were then subtracted from the measured forces in the atmospheric tests in order to determine the aerodynamic loading on the wings. Results showed that the mean thrust inside the vacuum chamber was approximately 17% of the mean thrust in atmospheric tests, suggesting that approximately 83% of the mean thrust measurement can be attributed to aerodynamic forces (Singh and Chopra, 2008).

Other methods for isolating and subtracting inertial forces have been used. Hong and Altman used high speed cameras to estimate inertial forces. With the high speed cameras they were able to determine the angular velocity and angular acceleration of the wing at different points throughout the stroke. With this information, as well as the mass properties of the wing, they were able to use simple physics to determine the inertial forces acting on the wing. The inertial forces at certain locations in the stroke were found in this method, and then polynomial function was fit to the data. The inertial forces could then be subtracted from measured values (Hong and Altman, 2006).

## 2.6 Photogrammetry

The process of using multiple synchronized cameras to capture three dimensional data about wings in flapping motion is not a new one. Carruthers and others used high speed video cameras to capture the landing of an eagle. The landing maneuver was used because of its predictability. The eagle always landed on the handlers arm, and always landed into the wind. Two cameras were used to capture the landing of the eagle. A

MatLab code was utilized that matches pixels for points on the wing that are visible to both cameras. Points used included the outline of the wing as well as some points within the bottom surface. Points that could be considered connected where grouped together into 'veins'. The wing was split into 55 strips, which were each split into 100 sections for analysis. The angle of attack of each section and strip was determined. A time sequence with minimal feather deflection was used to validate the MatLab code. It was determined that the algorithm used successfully computed the basic shape of the eagles wing (Carruthers, Taylor, Walker, and Thomas, 2007).

Stewart and Albertani have done work in which a Visual Image Correlation (VIC) system was used to determine the deformation of flexible flapping wings. The VIC system uses images from two high speed cameras, set up as shown in Figure 11, as well as stereo triangulation to measure in-plane and out-of-plane displacements. A random speckle pattern is used in this system and was applied to flexible wings, as well as to a rigid plate that was fixed to the inboard section of the wing. The rigid plate gave a method of measuring the rigid motion of the wing due to the flapping. Using the speckle pattern on the rigid plate, the software is able to determine the wing kinematics, or the rigid body flapping motion of the wing. The 3D data that represents the wing kinematics can be used to create a transformation matrix. This transformation matrix gives a method of separating the kinematics of the wing from the deformation of the wing. It is applied to the 3D data acquired from the speckle pattern on the flexible portion of the wing to determine the deformation of the wing (Stewart and Albertani, 2007).

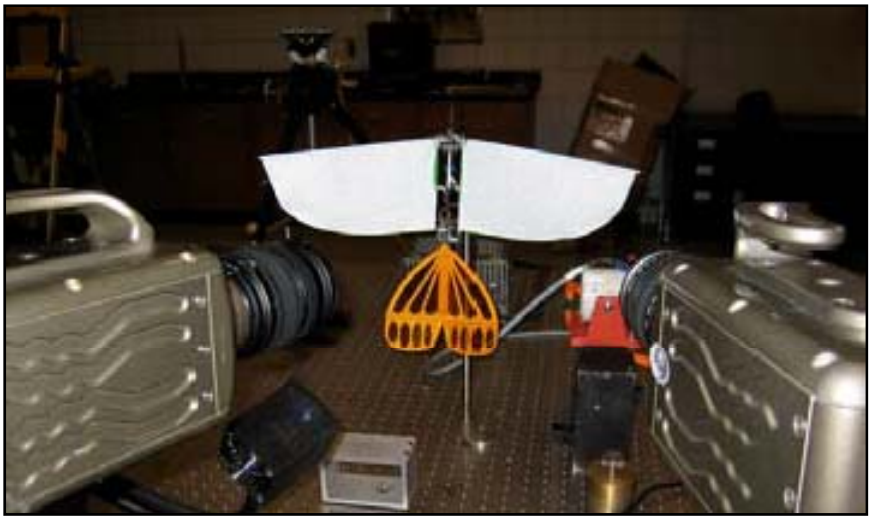

**Figure 11: Visual Image Correlation Validation Set-Up (Stewart and Albertani, 2007)**

The effect of wing flexibility was studied through the use of videogrammetry by Lunsford and Jacob. They used wings with a clear 2 mil polyethylene membrane that was marked with a 9 x 4 grid of fiducial markers. Because the membrane was clear, the marks could be used when viewing the membrane from either side. A LabView trigger was used to sync the force measurement from two load cells to the image capture from two high speed cameras. PhotoModeler was used to perform photogrammetry on the wings during flapping. Due to the flexibility, some of the corner points were not present in images from both cameras at some points in time. Analysis of the results shows that the wing does not deflect uniformly. An example of the clear wings used and example results from PhotoModeler are shown in Figure 12 (Lunsford and Jacob, 2009).

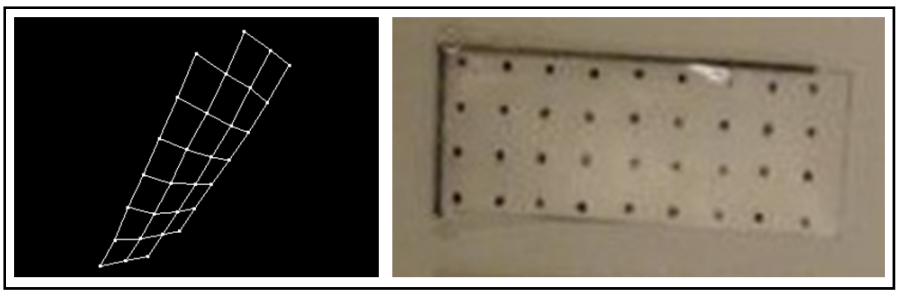

**Figure 12: Example Clear Wing with Grid (left) and PhotoModeler Results (right) (Lunsford and Jacob, 2009)**

Chakravarthy, Albertani, Gans, and Evers used two high speed cameras to research the flight of butterflies in their natural habitat. They set-up the cameras in a butterfly vivarium and captured images of multiple butterflies performing multiple flight maneuvers. Images were captured at 100-200 Hz. Using software, certain body parts of the butterfly, including the abdomen, wings, head and antenna, were tracked during certain categories of flight including takeoff, landing, flapping flight, gliding flight, hovering and wing morphing. Results showed that during take-off and steady flight the abdomen and the wing tips move out of phase with one another. As the wing tips move downward, the abdomen moves upward. As demonstrated in the research, this type of information can be used to design control systems for flapping wing MAVs (Chakravarthy, Albertani, Gans, and Evers, 2009).

Photogrammetry requires a consistently recognizable location on the wing so that the same location can be identified in images taken from different angles. Each of these studies have met this requirement either by using distinguishable features of bird or insect wings, or by applying some type of marking to man-made wings.

## 2.7 Dot Projection Photogrammetry

One limitation of traditional photogrammetry practices is that dots, or targets, on the wing are required in order to consistently mark the same points in each photo. For traditional rigid wings used in fixed wing flight this is not a problem since placing targets does not make a significant change to the dynamics of the wing. With small flapping wing vehicles, the wings themselves can be less than one gram. Placing adhesive targets on a wing that is so light can significantly change its mass properties, and therefore change the dynamic motion of the wing. For this reason it would be desirable to project dots on the wing with a laser.

Jones and Pappa used a white light slide projector to put light targets on an F-18 E/F wing for tracking. The wing was placed on a traverse to provide measured movement, and two cameras were used to capture images. Both projected dots and retro-reflective targets were used, with results showing that the projected dots and the retro-reflective targets both gave similar results. A laser was also used to project a dot pattern on a MAV. Accuracy of this method was limited by the speckle pattern that is produced by lasers reflecting off of a rough surface. The speckle pattern limited the consistancy of the centroid marking technique. The variation in marking laser targets was higher than the variation in marking retro-reflective targets (Jones and Pappa, 2002).

Dot-projection photogrammetry and videogrammetry was also studied for use on space structures by Pappa, Black, Blandino, Jones, Danehy, and Dorrington. One of the experiments done was to project dots on a plate that was swinging at a known frequency. Video of the plate, with the projected dots was taken and analyzed. The configuration is shown in Figure 13. The results of the dot projection videogrammetry were in-line with

the results using retro-reflective targets as well as the anticipated results from the known motion of the plate. Another experiment demonstrated the ability of dot projection videogrammetry to pick up on vibrations. A two-meter matte solar-sail was excited with an electrodynamic shaker. A laser vibrometer was used to measure the frequency response function yielding a mode of 3.34 Hz. Next a LCD projector was used to project 50 targets, and two video cameras recorded data at 15 frames per second. Analysis of the video yielded a mode at 3.47 Hz. These experiments demonstrated the versatility and capabilities of a dot projection system for use in photogrammetry (Pappa and others, 2003).

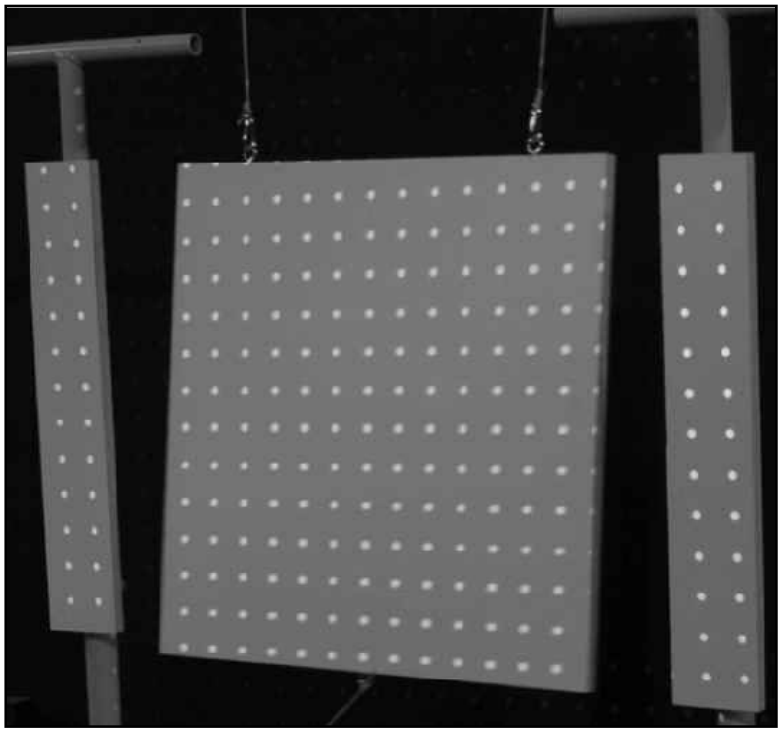

**Figure 13: Swinging Plate Configuration for Testing Dot Projection Targeting Method (Pappa and others, 2003)**

# 3. Methodology

## 3.1 Experimental Apparatus and Setup

### *3.1.1 Flapping Mechanism.*

Two flapping mechanisms were designed in SolidWorks and built. Prior work from Svanberg describes in detail the design and fabrication methods of a flapping only mechanism (Svanberg, 2008). Only minor modifications and repairs were done to the flapping mechanism developed by Svanberg. The main modification was the replacement of the pivot arm. The original pivot arm shown in Figure 14 has a hole in which an extension of the leading edge of the wing is inserted. A small set screw was used to hold in the wing and prevent it from twisting in the hole. The condition of the set screw deteriorated as repeated use caused stripping of the plastic into which it was fastened.

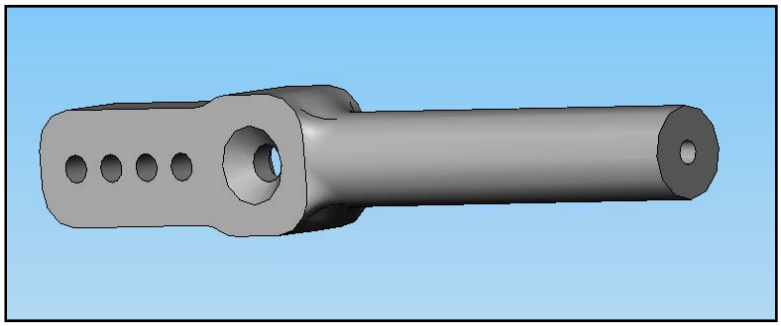

**Figure 14: Original Pivot Piece**

The initial solution to this problem was development of the pivot piece shown in Figure 15. A metal insert which housed a set screw was secured to the top of the pivot

piece. This prevented the wing root from twisting within the hole and secured the wing to the mechanism during flapping.

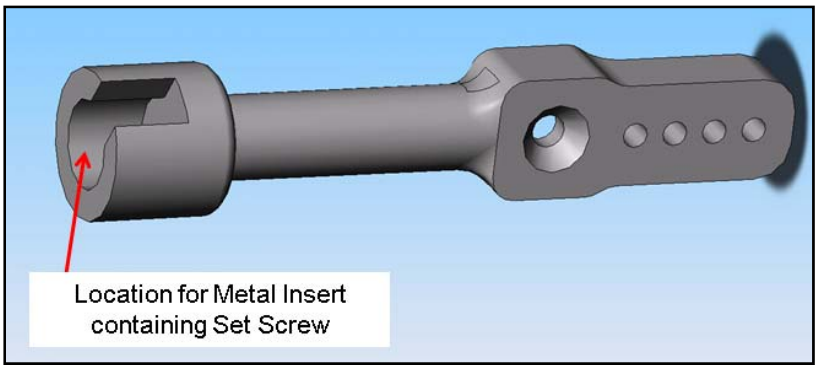


**Figure 15: Pivot Piece with Set Screw**

The pivot piece shown in Figure 15 solved the initial problem, although a second problem was encountered when using the aluminum tubing framed wings, discussed in more detail in the section 3.1.2. During flapping, all of the forces from the wing are concentrated at the attachment point. In this case the only attachment point was the extension of the leading edge. The forces generated during flapping caused inelastic bending of the aluminum tubing at the connection point to the pivot arm. Again, the pivot piece was re-designed to solve this problem.

The solution was to attach the wing to the pivot piece at both the leading edge as well as the root chord. The final pivot piece used in testing is shown in Figure 16. This method of attachment not only split the forces between two connection points, it also prevented the wing from twisting.

**Figure 16: Final Pivot Piece Used**

The two degree-of-freedom flapping with pitch mechanism described by Svanberg was also fabricated (Svanberg, 2008). The operation of the mechanism was demonstrated in SolidWorks before construction and is shown in Figure 17.

**Figure 17: SolidWorks Demonstration of Flapping with Pitch Mechanism**

As designed, the mechanism is capable of +/-35$^{o}$ in pitch during the stroke. Figure 18 shows how the pitching angle changes throughout the stroke as calculated using SolidWorks. An Objet Eden 500V 3-dimensional printer was used to print the parts designed in SolidWorks. The Du-Bro ball links used in the flapping only mechanism, shown in Figure 19, were used in the flapping with pitch mechanism for both the flapping push rods and the pitching push rods.

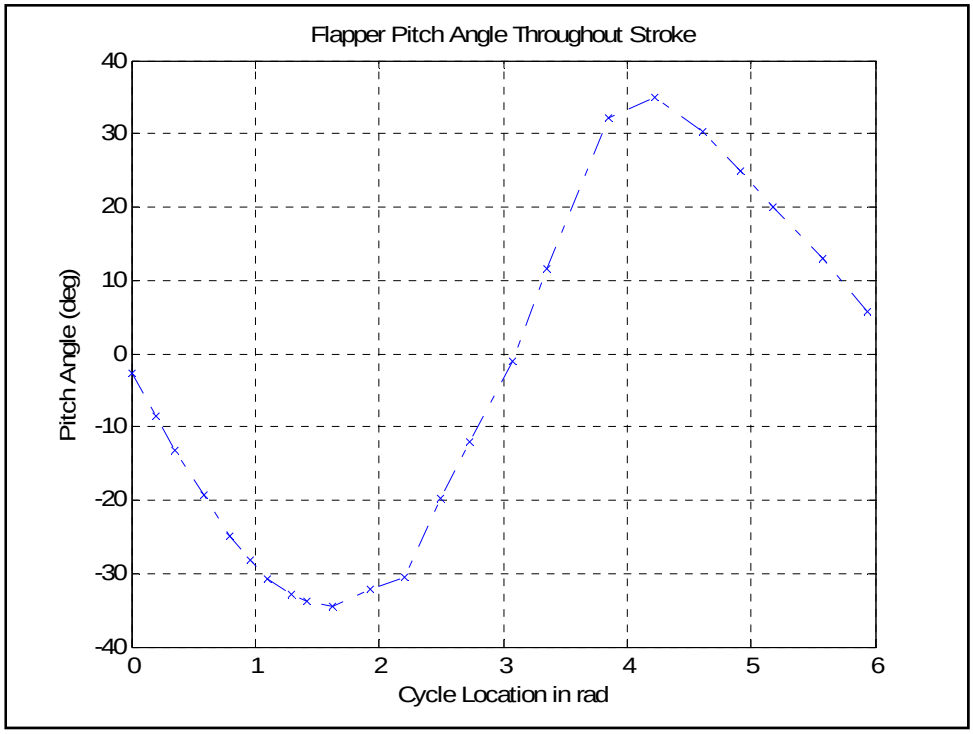


**Figure 18: SolidWorks Calculation of Pitch Angle throughout Stroke for Flapping and Pitch Mechanism**

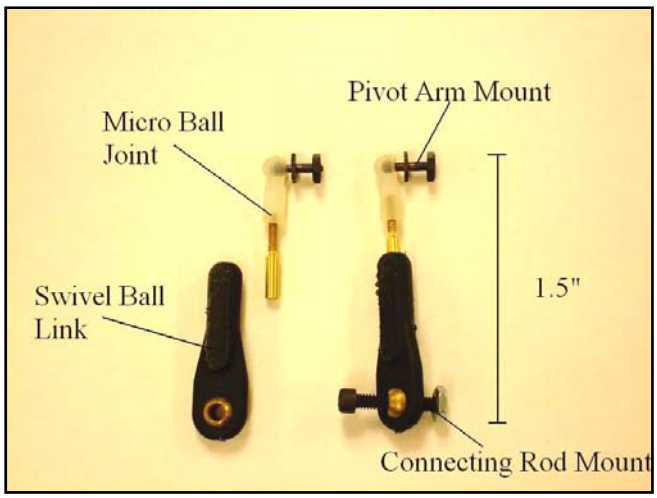


**Figure 19: Connecting Rods used in Flapping Only and Flapping with Pitch Mechanism (Svanberg, 2008)**

Some adjustments to the original design were made. Bearings were added to the inside of the pitch housing to ensure smooth rotation of the pitching shaft. The pitching shaft was also modified to allow for attachment of the pitching pushrod, and to ensure proper clearance while flapping. Operation of the mechanism from different camera angles is shown in Figure 21. The pitching motion of the wing through the stroke is demonstrated best in the images from camera 2. Both mechanisms used are shown in Figure 20.

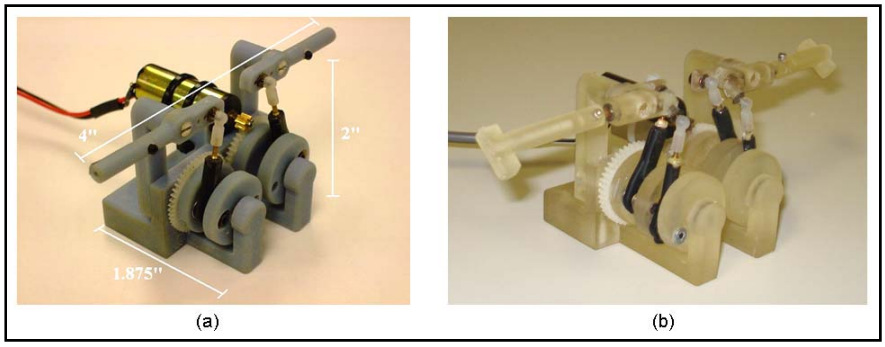


**Figure 20: Flapping Mechanisms: (a) Flapping Only Mechanism (Svanberg, 2008) (b) Flapping with Pitch Mechanism**

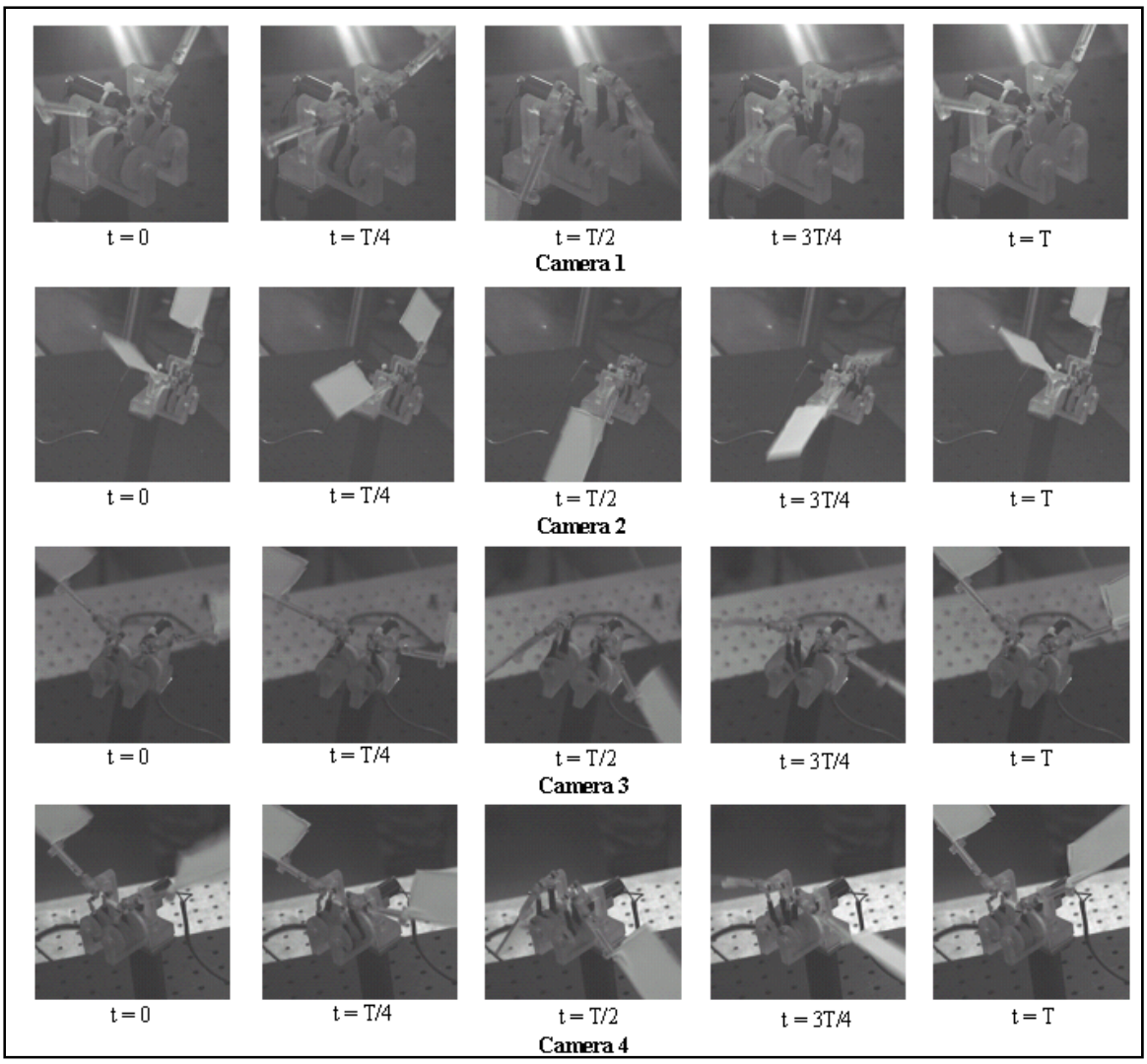


**Figure 21: Flapping with Pitch Mechanism in Operation**

### *3.1.2 Wing Construction.*

Initial work was done using the carbon fiber frame and mylar membrane wings developed by Svanberg (Svanberg, 2008). These wings produced thrust, but had limitations with regard to this research. The trailing edge and wing tip only contained the membrane edge with no structural support from frame material. For purposes related to repeatability, it was desired to have more structure to the wing to facilitate the

development of the laser dot projection method. The clear mylar membrane material also presented a problem. It did not provide adequate reflection of the laser grid. The possibility of utilizing the laser dot projection on the clear mylar membrane wings was investigated and is presented in section 4.2.

For this reason, it was desired to develop a set of wings that would provide both interesting force results, as well as provide an interesting platform for photogrammetry. To meet these criteria, a set of wings were developed so that the effects of spanwise camber could be investigated. These wings have the same dimensions as wing number 3 used in Svanberg's experiments (Svanberg, 2008). They have a leading edge length of 3 inches and a chord length of 1.5 inches, producing approximately a 10 inches total wingspan for the entire mechanism. The wings developed are shown in Figure 22.

Natural rubber latex provided a membrane material that was opaque, so that the laser dots could be easily seen when projected on it. The latex material used was approximately 0.006 inches thick, had a tensile strength of approximately 400 psi, and an ultimate elongation of 750%. A rectangular frame design was selected which provided support around the entire planform of the wing. It was desired to test both stiff and flexible wings that were both straight and had spanwise camber. Aluminum tubing (0.625" OD, 0.587" ID) was used for the tube frame wings, and six strands of (0.01" diameter) stainless steel wire twisted together were used for the wire frame wings. Spanwise camber was applied to wing sets of each frame material such that the ratio of the distance from root to tip along the curve of the wing to the straight line distance from root to tip was approximately 0.95. This is in reference to work by Pennycuick which determined that the span of a cormorant during flight, when normalized by the maximum

span, varied from 0.7 to 1 during the stroke, demonstrating that birds apply spanwise camber adjustments in flight (Pennycuick, 1989).

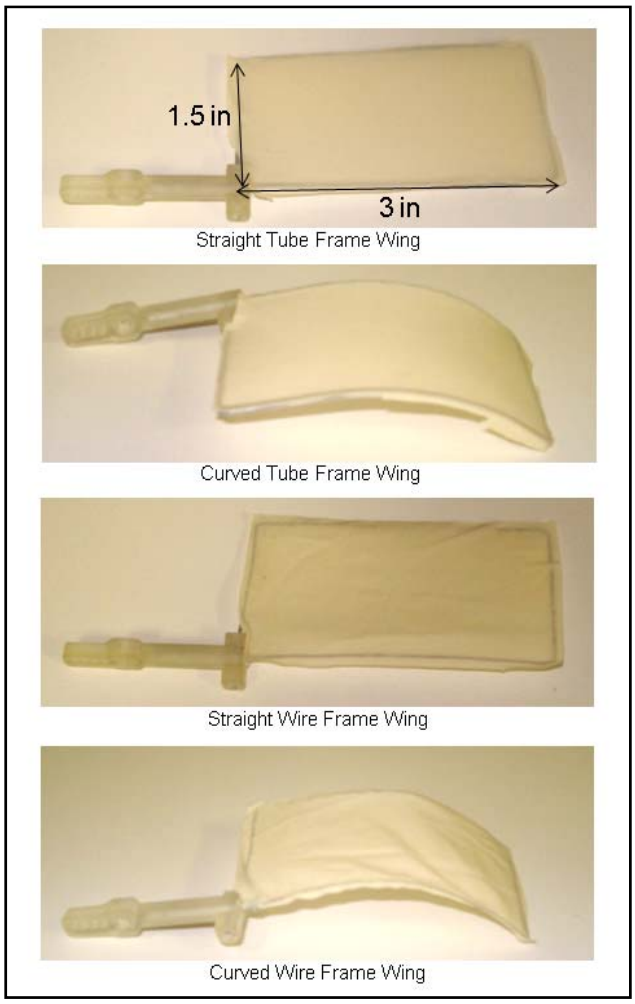


**Figure 22: Wings Used in Testing**

The aluminum tube frame wings were relatively stiff. The wire frame wings were flexible to the point that flexure was visible throughout the stroke. The latex membrane was attached by spreading out and pinning latex to a board as shown in Figure 23. The frame was sprayed with Elmer`s Multi-Purpose Spray Adhesive and then pressed onto the latex. The glue was allowed to dry for approximately 1 hour, at which point the latex

was trimmed around the frame. As validation of measurement methods was of primary concern, this construction method was adequate for our purposes, although is limited in repeatability. Experimentation more concerned with detailed analysis of wing performance may require a different, more precise construction method.

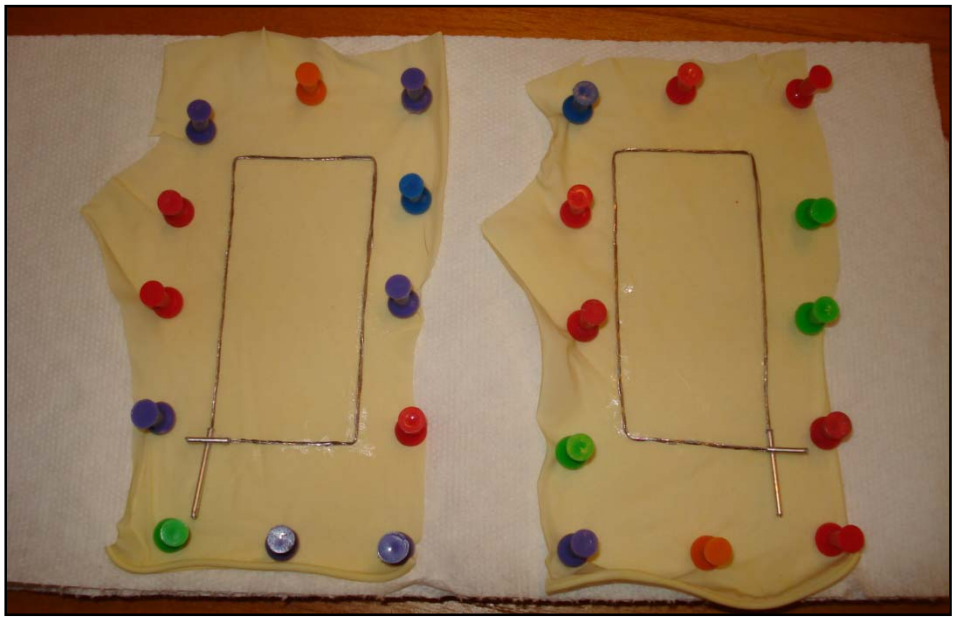

**Figure 23: Attachment of Latex Membrane to Wing Frames**

Review of test results from these wing sets lead to the development of a wing set that was a hybrid of the two different frames. Aluminum tubing was used for all portions of the wing except the trailing edge and half of the tip chord, for which a single strand of stainless steel wire was used. Figure 24 shows the wing frame design. Latex was used for the membrane and was attached as before. This wing design allowed for some flexibility of the wing while keeping the overall planform of the wing relatively constant.

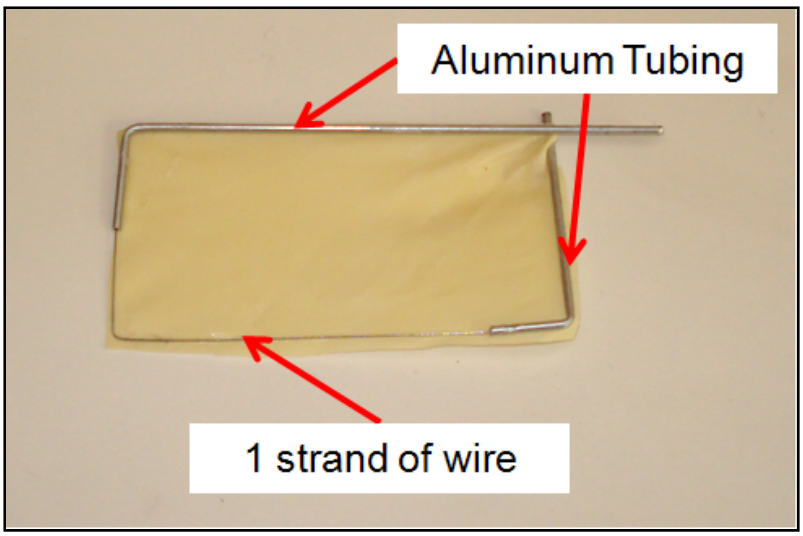


**Figure 24: Hybrid Frame Wing**

### *3.1.3 Testing Equipment.*

The equipment used can be broken down into two categories. Equipment used for force measurement, and equipment used for high speed video and photogrammetry.

Force data was collected primarily using a six component force balance built by Modern Machine and Tool Co. The force balance is strain gauged based and capable of measuring normal force, axial force, side force, pitch moment, roll moment, and yaw moment in the ranges specified in Table 1.

The force balance was mounted inside a stainless steel sting, and the sting was mounted to a stand which was attached to the table. The setup is shown in Figure 25. The mechanism was mounted to the force balance using a piece designed in SolidWorks and printed using the Objet Eden 500V 3-D printer. The force balance mount was designed to put the center of gravity of the mechanism above the center of gravity of the balance. This extends the range of the pitch moment measurement by ensuring that the pitch moment is near zero when the mechanism is at rest.

**Table 1: Force Balance Load Ranges**

| Component | Measurement range |
|---|---|
| Normal Force | +/- 4 lbs (+/- 1814 g) |
| Axial Force | +/- 2 lbs (+/- 907 g) |
| Yaw Force | +/- 2 lbs (+/- 907 g) |
| Pitch Moment | +/- 2 in-lbs (+/- 23,043 g-mm) |
| Roll Moment | +/- 4 in-lbs (+/- 46,043 g-mm) |
| Yaw Moment | +/- 2 in-lbs (+/- 23,043 g-mm) |

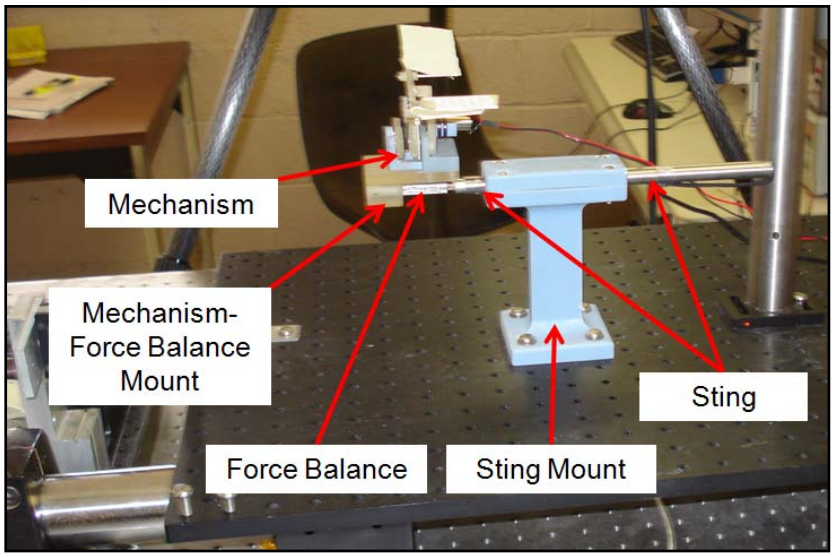


**Figure 25: Force Balance Set-Up**

A National Instruments data acquisition system and LabView 8.5 were used to collect the data. The six channels of the balance were connected to six of the eight available channels on a SCXI-1314 terminal block in accordance with the force balance manual. A connection diagram for channel 1, the normal force, is shown in Figure 26.

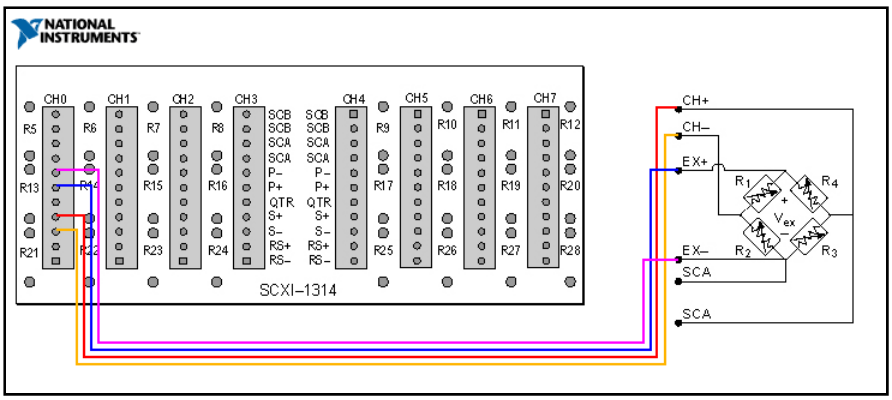


**Figure 26: Normal Force Example of Force Balance Wiring to SCXI-1314 Module**

The terminal block was then connected to a SCXI-1520 universal strain gauge input module. This system is specifically designed for use with Wheatstone bridge based strain gauges. An excitation voltage of five volts was used. Initial analog signal conditioning was accomplished within the SCXI-1520 hardware for each channel individually. The signal is amplified in accordance with the anticipated voltage range specified by the user. The anticipated voltage range was specified in the calibration book by the balance manufacturer, and is shown in Table 2 along with the corresponding amplification values determine by the National Instruments system. After the signal is amplified, an adjustable anti-aliasing low-pass analog filter is applied to the signal to help to decrease higher frequency noise on the measurement signal.

A task within LabView was setup to sample the voltage from the strain gauge. A 'voltage with excitation' task was used instead of the traditional 'strain' task. This was done because all of the calibration and sensitivity information given for the balance is based on voltage, not strain. The task reads data from all six channels at the same time. The data is then separated into individual channels so that the amplification values selected by the system for each channel could be viewed. Potentiometers are electrical

devices that are have variable resistance and can be used to control voltage in low power circuits. Fine and coarse potentiometers are used within the data acquisition hardware to control the voltage output of each channel. They were adjusted for so that the unloaded zeroes for each channel of the balance were as close as possible to the values specified in the force balance calibration book that was provided by the balance manufacturer. The potentiometer values are also specified in Table 2.

**Table 2: Parameters of Force Balance Channels**

| Channel | Voltage Range +/- (mV) | Amplification | Unloaded Zero (mV) | Coarse Potentiometer | Fine Potentiometer |
|---|---|---|---|---|---|
| Normal Force | 10.244 | 870 | -0.518 | 62 | 2127 |
| Axial Force | 5.16 | 1000 | 0.82 | 62 | 2131 |
| Pitch Moment | 5.688 | 1000 | 0.146 | 62 | 2151 |
| Roll Moment | 6.688 | 1000 | -0.282 | 62 | 2060 |
| Yaw Moment | 5.639 | 1000 | 0.859 | 62 | 2087 |
| Side Force | 5.085 | 1000 | 0.388 | 62 | 2071 |

Analog filtering was available at values of 10Hz, 100Hz, 1kHz, and 10kHz. Analog filters are used to solve the aliasing problem in spectral analysis. The anti-aliasing filter frequency should be selected such that it is half the sample rate or lower. High frequency content was not required for our purposes, so an analog filter of 100Hz was chosen. With a sample rate of 200 Hz (0.005 sec), this filter substantially reduced noise.

A screen shot of the LabView Virtual Instrument (VI) developed is shown in Figure 27, and the block diagram is shown in Figure 28. The signal is broken into six channels, and each channel is output to a plot on the screen. This allowed the data being measured by the balance to be viewed in real time. A button was put on the screen to

turn on and off the data collection function. Data was written to the specified file after every 10 points were acquired, which corresponds to every 0.05 seconds. No digital signal processing was accomplished within LabView. The raw voltage data for all six channels was saved as the output file. This ensured that no data was lost and digital signal processing parameters could be adjusted after the data was taken. MatLab was used for post processing.

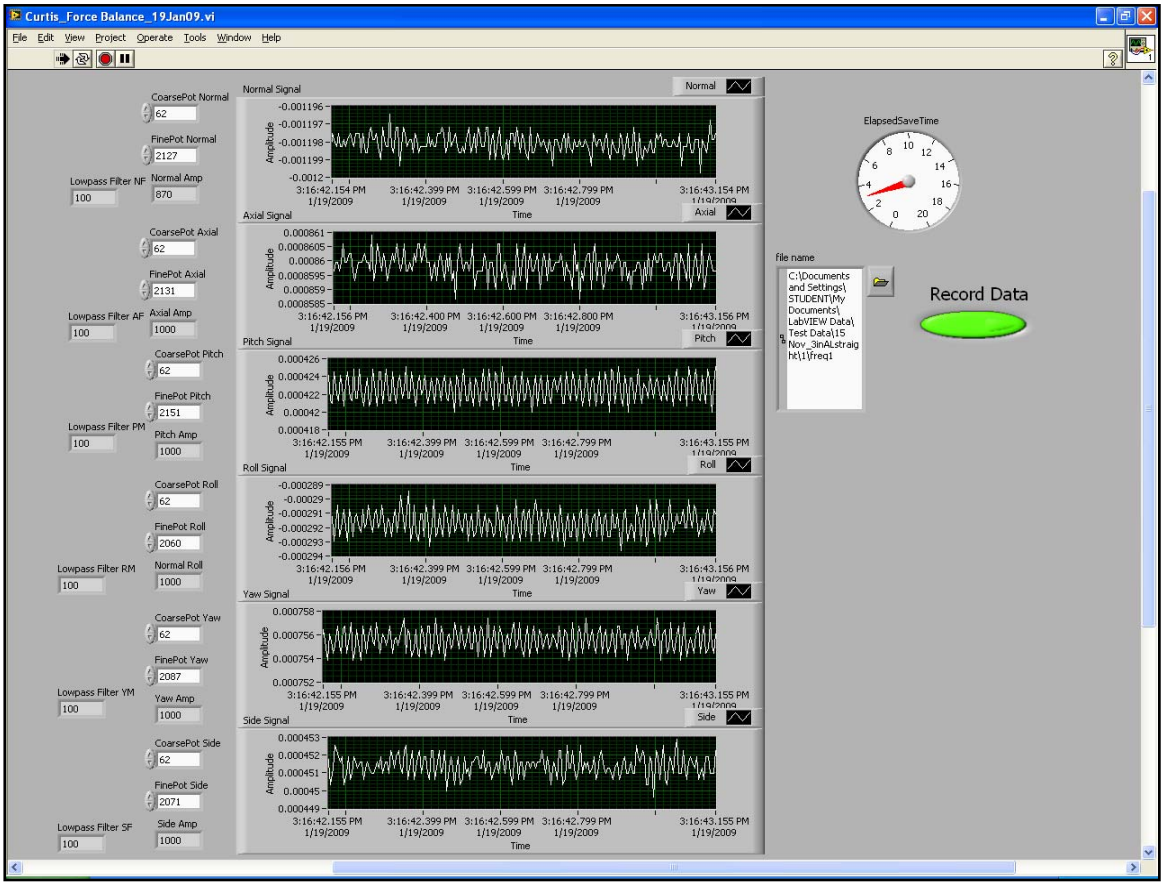


**Figure 27: LabView VI Used for Data Acquisition**

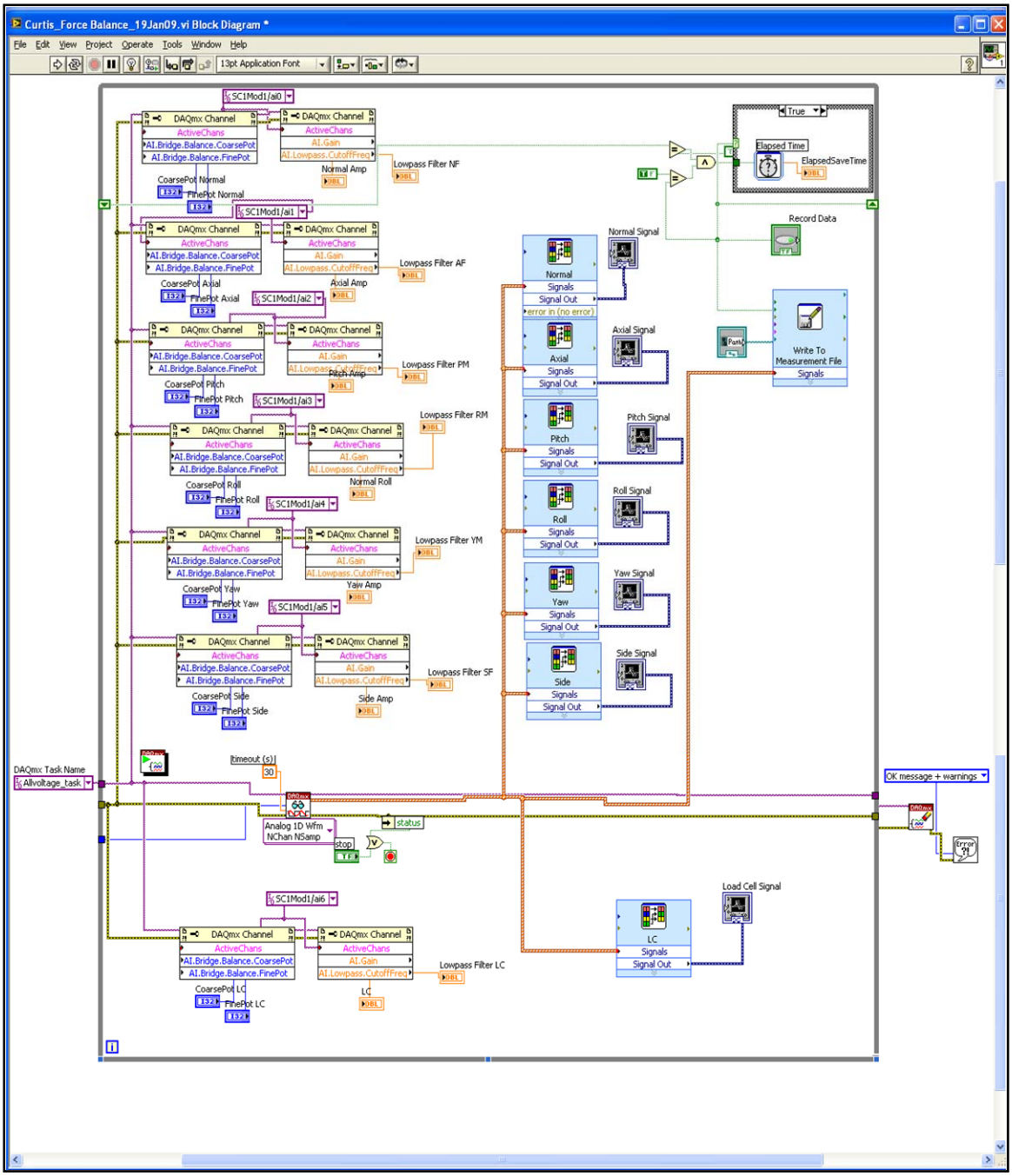


**Figure 28: Block Diagram of LabView VI**

A secondary method, developed by Svanberg, was used to measure the average axial force, and to validate the force balance measurements (Svanberg, 2008). This method involved the use of a load cell and an air bearing table. The linear air bearing

table, shown in Figure 29, uses four linear air bearings that slide on two stainless steel rails. A 24" x 18" aluminum plate is mounted on the air bearings. When the bearings are supplied with compressed air it provides for near frictionless motion of the table along the rails. Mounting the mechanism to the top of the air bearing allows the aerodynamic force that the mechanism creates during flapping to be directly transferred to the air bearing table, which in turn can be measured by a load cell (Svanberg, 2008). Validation was required to ensure the balance and data acquisition system were functioning properly.

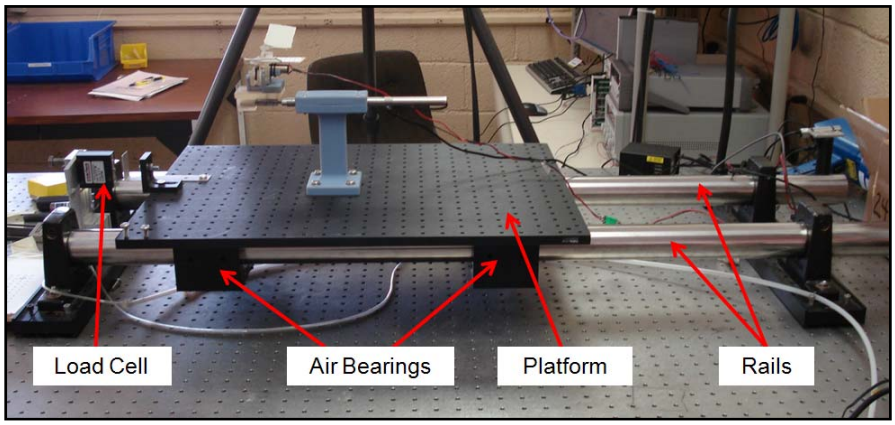


**Figure 29: Linear Air Bearing Table Set-up**

A strain gauge transducer load cell made by Interface was mounted to the rigid frame of the air bearing table such that the force from the frictionless platform could be measured, shown in Figure 30. The air bearing table was angled slightly so that the load cell was under constant loading. Initially the load cell was connected to a separate digital display, and the reading was manually recorded for each case. This method proved in-effective for small measurements that changed constantly with flapping. To remedy this situation the load cell was connected to the data acquisition system used for the force

balance. The load cell is also strain gauge based, and there were available channels on the data acquisition system so the strain gauge was simply 'plugged in' to an available port on the terminal block. The load cell channel was added to the LabView VI used for the force balance so that the load cell voltage could be recorded along with the voltages from the force balance. The excitation voltage for the load cell was set to 10 V and a calibration was accomplished. The slope of the calibration curve was applied to the voltage readings in post processing to get the measured force in grams. Once the force balance measurement technique was shown to give comparable results to the load cell measurement technique, the load cell was no longer used.

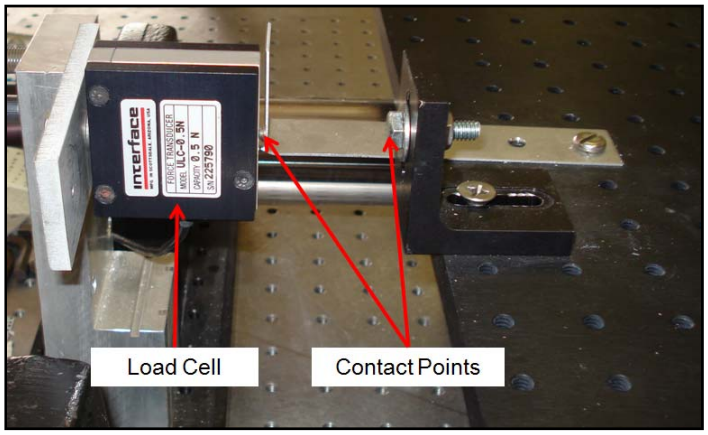


**Figure 30: Load Cell Mounting**

Control of the flapping mechanism speed was accomplished by controlling the power supplied to the DC motor. This was accomplished using an Instek laboratory DC power supply shown in Figure 31. The wires from the mechanism motor were attached to the power supply in front. The coarse adjustment current knob was turned on and left constant. The fine adjustment voltage knob was used to control the motor speed, and therefore the flapping frequency.

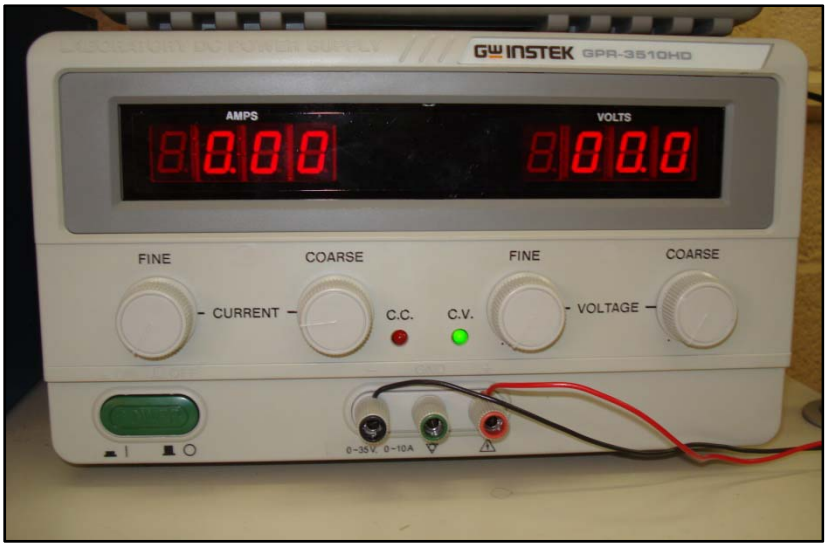


**Figure 31: Power Supply Used to Control Mechanism Flapping Frequency**

An 115V Monarch Phaser Strobe was used to estimate the flapping frequency of the mechanism. An optical sensor was mounted in front of the mechanism looking back on the crankshaft. A piece of reflective tape was placed on the crankshaft. The optical sensor records each time the reflective tape passes through its beam, and the frequency of the flapping is displayed on the strobe light screen. This gave an estimate of flapping frequency, while actual flapping frequency was determined from the Power Spectral Density (PSD) of the force measurements as discussed in section 3.2.1.

A vacuum chamber was designed and built to separate the inertial loads from the aerodynamic loads. The chamber was designed in SolidWorks, a rendering is shown in Figure 32. The total dimensions were approximately 24" x 24" x 24". The bottom plate is made of an aluminum plate 0.75" thick. Holes were machined in the bottom plate so that plates containing sealed pass-through ports for data, electrical power, and a pressure sensor could be attached. The connection to the vacuum pump was through the smaller hole in the aluminum plate. The other five sides were made of Acrylic plates 0.944"

thick. Circular o-rings are used around the top and the bottom while linear o-rings are used on the vertical edges. Threaded rods with wing-nuts were used along the corners to connect the sides.

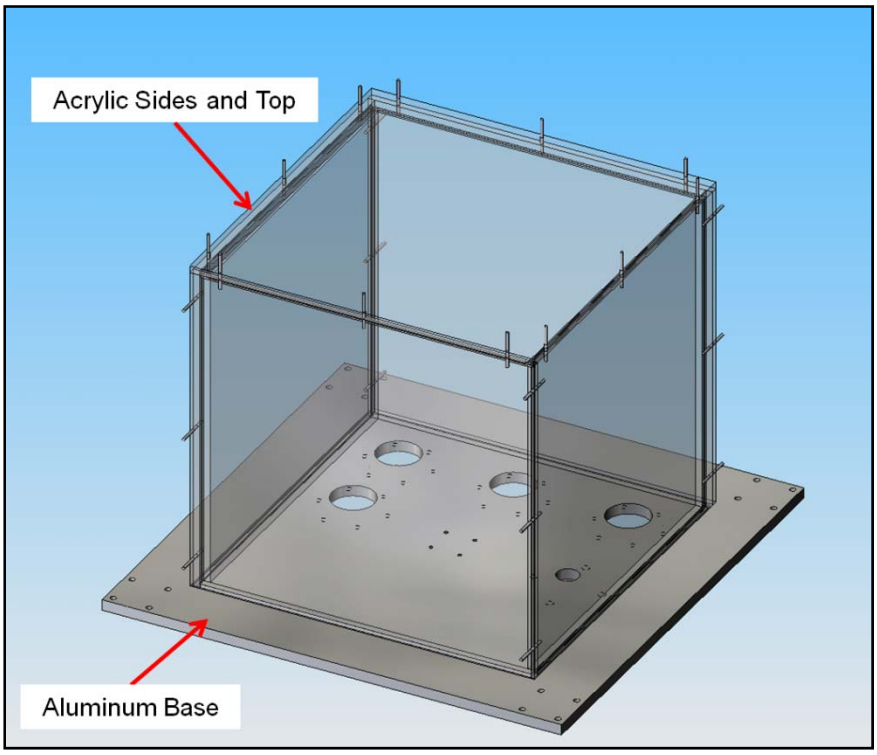


**Figure 32: Vacuum Chamber Design**

Once assembled, suction was applied using a Welch model 2585B-01 vacuum pump. The corners and vertical edges did not seal properly, and only about a half vacuum was achieved. The vertical edges were then bonded using Weld-On #16 solvent cement, and the bottom of the chamber was sealed to the aluminum using caulking. Once an adequate vacuum was finally achieved, the deflection of the side plates put enough force on the threaded rods to crack the acrylic side pieces in two places. As a safety precaution this part of the project was placed on hold and the chamber will need to be redesigned. No vacuum testing was accomplished as part of this effort.

The high speed video images used for photogrammetry were captured using a four camera system supplied by AFRL. The cameras used were Photron MC2 High Speed Digital cameras. These cameras are capable capturing images at 2000 Hz at resolution of 512 x 512. The camera head and lens, shown in Figure 33a, are separate from the camera body, shown in Figure 33b. The camera heads were mounted on tri-pods on either side of the flapping mechanism. Tamron A031 AF 28-200mm F/3.8-5.6 XR Di Aspherical (IF) Macro Zoom Lenses were used for testing. The overall set-up is shown in Figure 34. Photron FASTCAM Viewer 3 was used for image acquisition and PhotoModeler 6 from Eos Systems Inc. was used for photogrammetry. While all data presented was acquired with the AFRL camera system, preliminary work was done utilizing AFIT's three camera system.

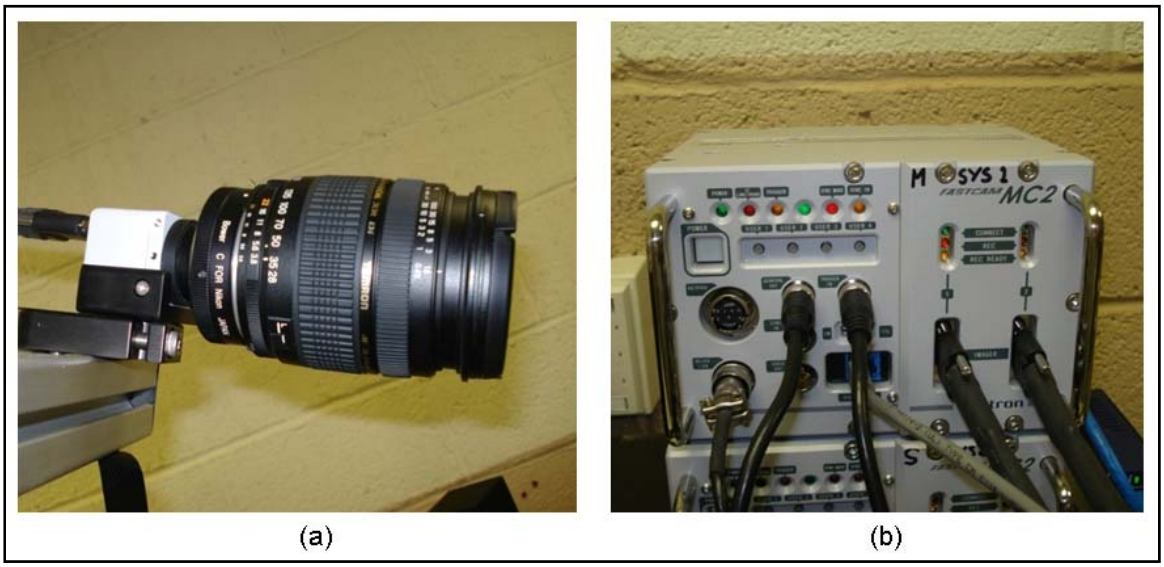


**Figure 33: High Speed Cameras (a) Camera Head (b) Camera Body**

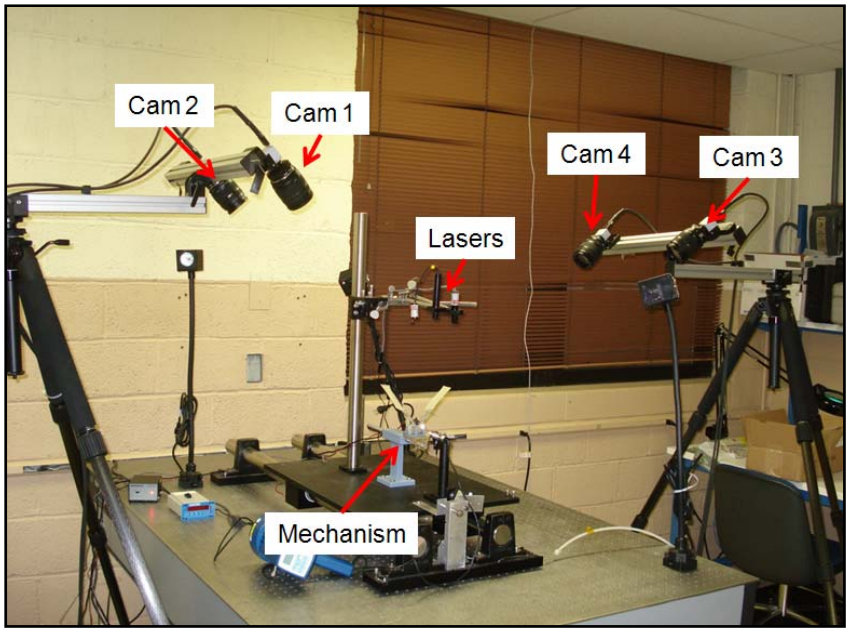


**Figure 34: Overall Set-up for High Speed Video Acquisition**

Two Lasiris Lasers Diodes made by StockerYale and purchased through Edmund Optics were used for dot projection. One of the lasers used is shown in Figure 35. These lasers are fairly small and inexpensive; they are operated at 7 mW and 101mA. Projection heads are available for these lasers that split the light into many different patterns. A projection head was selected which created a seven by seven square structured light dot array for each laser, giving 98 total points for the combination of two lasers. When the projection head is attached, these lasers are considered Class II and do not require eye protection.

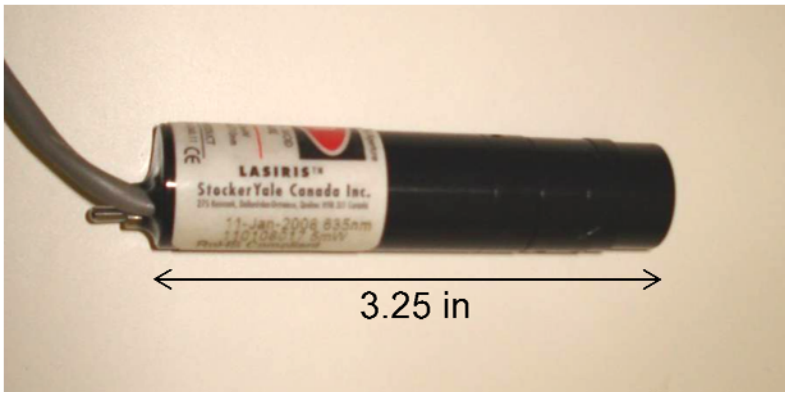


**Figure 35: Laser Diode**

The two lasers were mounted above the wing such that the best coverage throughout the stroke was achieved, as shown in Figure 36. This was difficult because of the fact that the size of the projected dot array on the wing varies with the distance of the wing from the laser. The laser array overall size increases as the surface moves away from the laser. While good coverage was achieved in the middle of the stroke, coverage became sparse at the bottom of the stroke and the wing was not fully covered at the top of the stroke. Because the lasers are relatively inexpensive, additional lasers could be purchased and focused at other locations in the stroke to alleviate this problem. Improvement in this area could also have been achieved by straightening, or collimating, the laser array with a lens so that the beams are parallel and the grid size remains constant with distance.

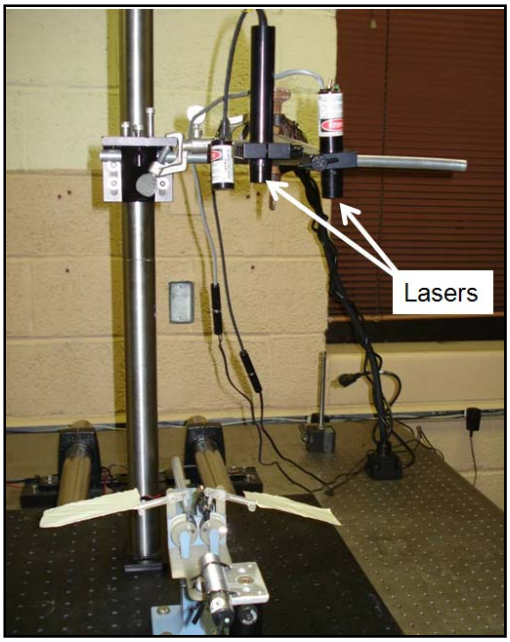


**Figure 36: Laser Dot Projection Set-Up**

## 3.2 Experimental Procedure

### *3.2.1 Force Measurement.*

Force measurements were taken for the wings discussed in section 3.1.2. The method for force measurement was as follows. First, wing sets were attached to the mechanism, giving an overall wingspan of approximately 10 inches (0.254 m). Next the mechanism was secured to the force balance. The LabView VI described in section 3.1.3 was run. Before turning on the mechanism, a data set is taken which serves as a tare file. All data sets were taken by recording data at 200 Hz for at least 16 seconds. Next the voltage to the flapper motor was turned up until the flapper started moving. A data set was taken, the approximate frequency was recorded from the phaser strobe, and the voltage and current draw from the motor was recorded. The voltage was increased, and a new data set, frequency, voltage, and current were taken. This was repeated at

approximately seven different frequency points within the frequency range. The lowest frequency at which the mechanism can continuously operate is approximately 2.5-3 Hz. This limit is due to the need to overcome the static friction in the mechanism. The highest frequency is limited by the power of the motor and is based on the weight of the wing. It was approximately 7.5-8 Hz for the wings examined in these tests. Once data is captured at seven frequency points the mechanism was turned off. The mechanism was looked over to ensure that it was still in good working order and that the wings were intact. Another tare file was taken and the process was repeated. This was done for each wing set approximately 10-15 times.

Data was also taken for the axial component using the load cell and air bearing table system. The process was the same, but with one added step. Before the tare file was taken, compressed air was supplied to the table. Once the air bearing table was pressurized, the table was allowed free contact with the load cell. To do this, a bolt that was in place to protect the load cell was loosened to allow free contact. The power wire to the mechanism and the data lines from the balance were taped so that they applied as little force as possible to the air bearing table. Since the load cell was wired into the same acquisition system, no additional steps were required; the load cell voltages were recorded in the same data file for post processing.

Post processing of the force balance voltage data taken from LabView was done in MatLab. Data files for each run were saved in separate folders, allowing automation of post processing. Once the data was read into MatLab, the interaction matrix was applied. When multiple strain gauges are used together to measure different components of force, as is the case in a six component balance, it is impossible to fully separate the

forces. For instance, forces applied purely in the axial direction will cause some change in voltage on the normal channel. Values for the interactions between the six components were provided by the manufacturer in the 27 x 6 interaction matrix which is shown in Appendix A. These interactions between the voltages on each channel must be taken into account in order to determine the actual force that was applied. The interaction matrix provided was determined by the manufacturer by performing a static calibration. From conversations with Dr. Albertani, it was noted that improvement might be achieved by performing some type of dynamic calibration to ensure the accuracy of dynamic measurements (Albertani, 2008). The method below was used to apply the interaction matrix in post processing; a summary of the process is shown in figure__.

1. Using equation 5, convert the measured voltage from each channel to lbs (or in-lbs) by applying constants determined from the unloaded zeros, voltage ranges, and measurement ranges for each channel that are given by the balance manufacturer

   $$Measured\ load\ (lbs\ or\ in-lbs) = \frac{Max\ Load}{(V_{max} - V_{unloaded})} * V_{measured} \quad (5)$$

2. Determine the initial values of the 27 interaction parameters on the left hand side of the interaction matrix (Appendix A) where abbreviates are as follows: NF=Normal Force, AF=Axial Force, PM=Pitch Moment, RM=Roll Moment, YM=Yaw Moment, and SF=Side Force.
3. For each of the six components determine the resolved force/moment by multiplying each of the interaction parameters by the corresponding value, in the corresponding column of the interaction matrix and then subtracting this

result from the measured value. The equation for the normal force is shown in equation 6.

$$NF_{resolved} = NF_{measured} - [AF * AF_{IM} + PM * PM_{IM} + RM * RM_{IM} + YM * YM_{IM} + SF * SF_{IM} + NF^2 * NF^2{}_{IM} + (NF * AF) * (NF * AF)_{IM} + (NF * PM) * (NF * PM)_{IM} + (NF * RM) * (NF * RM)_{IM} + (NF * YM) * (NF * YM)_{IM} + (NF * SF) * (NF * SF)_{IM} + AF^2 * AF^2{}_{IM} + (AF * PM) * (AF * PM)_{IM} + (AF * RM) * (AF * RM)_{IM} + (AF * YM) * (AF * YM)_{IM} + (AF * SF) * (AF * SF)_{IM} + PM^2 * PM^2{}_{IM} + (PM * RM) * (PM * RM)_{IM} + (PM * YM) * (PM * YM)_{IM} + (PM * SF) * (PM * SF)_{IM} + RM^2 * RM^2{}_{IM} + (RM * YM) * (RM * YM)_{IM} + (RM * SF) * (RM * SF)_{IM} + YM^2 * YM^2{}_{IM} + (YM * SF) * (YM * SF)_{IM} + SF^2 * SF^2{}_{IM}] \quad (6)$$

In equation 6 the subscript IM represents the corresponding value in the NF column of the interaction matrix. This needs to be done for each force and moment. Luckily by utilizing matrix mathematics this can be done simply with matrix multiplication using equation 7.

$$F_{resolved} = F_{measured} - C * IM \quad (7)$$

Where $F_{resolved}$ is a matrix 1x6 in dimension representing the six resolved forces/moments, $F_{measured}$ is a matrix 1 x 6 in dimension representing the six measured forces/moments, C is a matrix 1 x 27 in dimension representing the 27 interaction parameters (NF, AF, PM, etc…), and IM is the interaction matrix which is 27 x 6 in dimension.

4. Subtract the resolved values from the measured values. If the maximum difference for each component is low enough, in this case less than 1e-14,

then the resolved values are the final values with the interaction matrix applied. If the difference is not low enough additional iteration is required. Repeat steps two and three but use the values calculated in the first iteration to determine the 27 interaction parameters. Repeat iteration until the maximum difference between consecutive iterations is sufficiently low.

5. Convert back into voltage for additional processing.

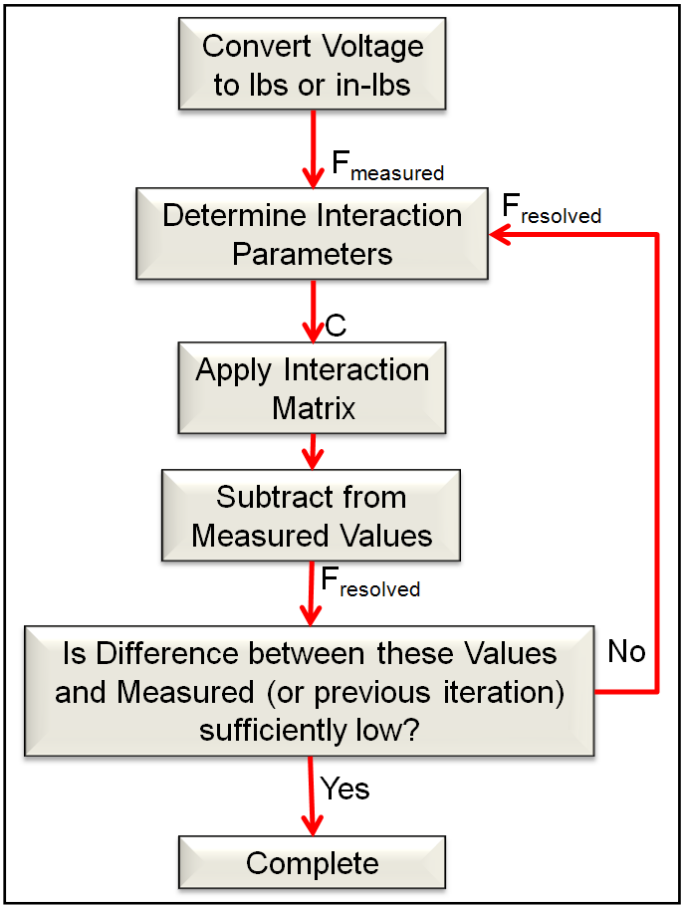


**Figure 37: Summary of Interaction Matrix Application Process**

The interaction matrix was applied to the data at each time step. The next step in post processing was subtracting the tare file. The interaction matrix was applied to the average voltages from the tare file. These values were then subtracted from data taken at

each time step. Next the data was converted to grams or gram-mms. The resulting data set represents the inertial and aerodynamic forces and moments produced by the mechanism during the time period recorded.

The frequency of the given data set was determined from spectral analysis. Since the fast Fourier transform was used in the processing, the number of data points per block needs to be a power of two. A block size of 1024 was used, and a hanning window applied. This block size will produce 512 frequency data points over the Nyquist range of 0-100 Hz. Since data was sampled for at least 16 seconds, there was a minimum of three unique blocks of data. A 50% overlap was chosen, and the PSD values from each block averaged. An estimate of the frequency of flapping, taken from the phaser strobe, was used to determine a range in which to look for the peak on the PSD. The frequency location of the highest peak of the averaged PSD within the range was taken as the frequency of flapping for that data set. This method gives the average flapping frequency for the data set to within approximately +/- 0.1 Hz. An example of the PSD for a flapping frequency of 6.25 Hz is shown in Figure 38b along with a time series of voltage readings from the Normal Force channel shown in Figure 38a. As shown, the highest peak is at the flapping frequency, and additional peaks are seen at each harmonic of the flapping frequency.

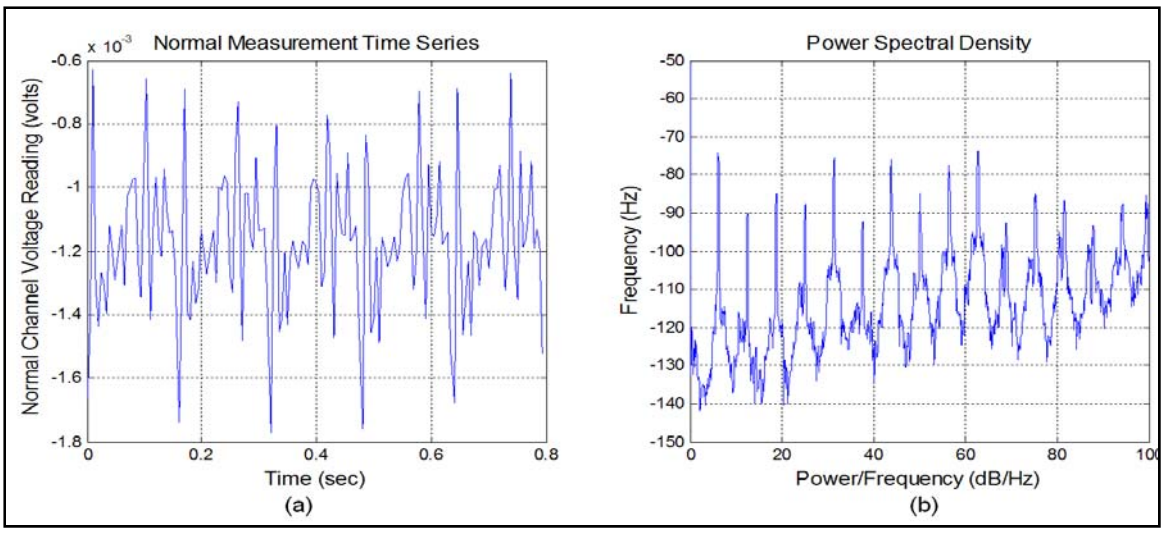


**Figure 38: (a) Example Time Series at 6.25 Hz flapping frequency (b) Example Power Spectral Density at 6.25 Hz flapping frequency**

Post processing of load cell data was also done in MatLab. The process was much simpler. The load cell data from the tare file was averaged and subtracted from the file. The calibration slope was applied to the voltage reading to give the measurement in grams.

The average normal and axial forces were compared for the four wing sets. The data acquisition process did not require a constant set of flapping frequencies for each run. This made the determination of overall averages and error bars for the combination of all runs more challenging. The solution was to break the frequency range into sections, each 0.4 Hz wide. Each data point, which represents the average value of normal or axial force from a given data set, was separated into a section based on its frequency value. Once sorted, sections with at least four data points were used. The force values were averaged, and the standard deviation was determined. The error bars were determined by applying a 95% confidence interval to the standard deviation as

specified in the Barlow, Rae and Pope textbook (Barlow, 1999). The frequency value for the data point was taken as the average of the frequency values within the section. Since the frequencies are averaged, the calculated standard deviation will be larger than the actual standard deviation supported by the data.

### *3.2.2 High Speed Images/Photogrammetry.*

The experimental procedure for gathering the high speed images used for photogrammetry began by attaching the proper wing set to the mechanism, and mounting the mechanism to the force balance. For consistency, the mechanism was mounted to the force balance for photogrammetry experiments as well as force measurement experiments. A piece of balsa wood was marked with dots spaced at 0.25" and was attached to the mechanism. This served as a set of stationary reference points used in the photogrammetry process.

The lasers were positioned above the wing and were adjusted to provide the best coverage of the wing at the midstroke while also providing the best possible coverage throughout the rest of the stroke. An image of the laser grid positioned on a wing is shown in Figure 39; the arrows labeled ‘x’ and ‘y’ represent the coordinate frame used, the z direction is defined perpendicular to the x-y plane and positive upward. Although the color of the lasers is different, the cameras produce black and white images so the laser grids look identical.

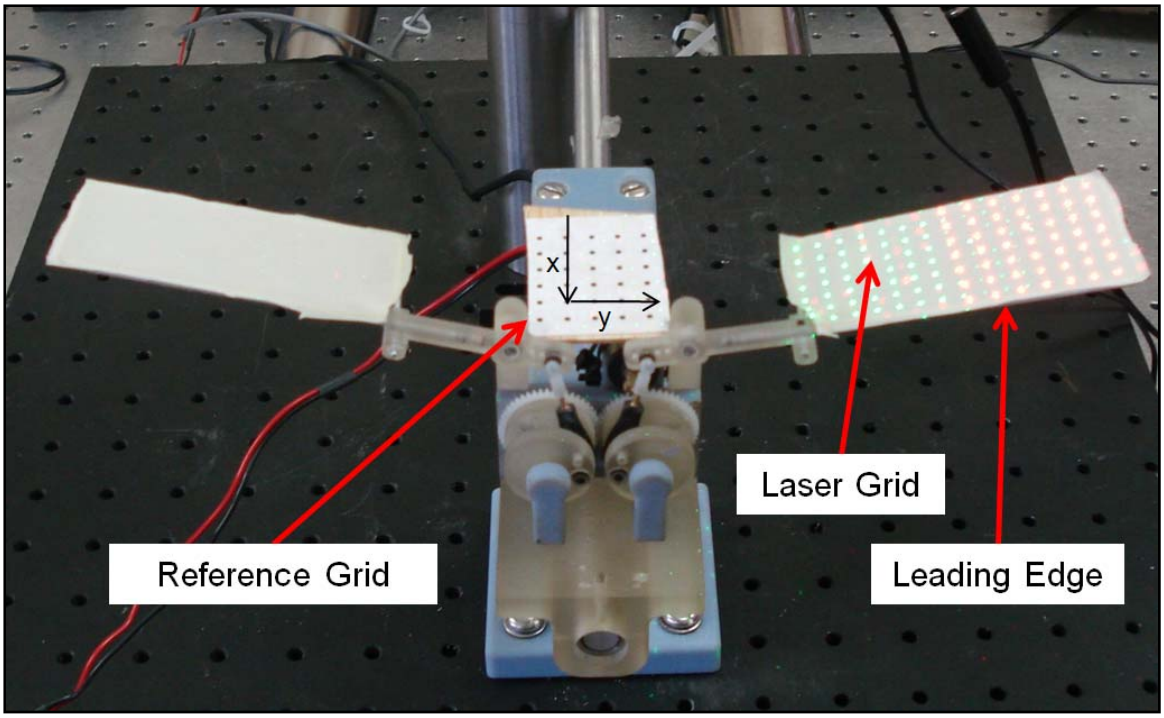


**Figure 39: Flapping Mechanism with Laser Dot Grid**

Once the lasers were positioned, the cameras were positioned. The cameras were located in sets of two on either side of the table holding the mechanism. All four cameras were focused on the port wing. Two cameras were pointed and focused on the upper portion of the stroke, and two cameras were pointed and focused on the lower portion of the stroke. Cameras were positioned and focused such that the entire flapping stoke was captured, and such that the reference points were captured. The overall set-up is shown in Figure 34.

Images were captured at 1000 fps with a shutter speed set to 1/1000 seconds. The apertures on the lenses were completely opened, to an F-stop of 3.8, so as to allow in as much light as possible. Although the laser grid showed up in the images at this setting with no additional lights, in order to see the reference points clearly, and to see the

motion of the wing, additional lighting was needed. Additional lights were turned on and adjusted until the reference points were visible. The additional lights were too bright to point directly at the mechanism. For best results the lights were turned on, but pointed away from the mechanism.

The image acquisition system used has many different options for triggering the acquisition of images; the 'end' trigger mode was selected. This method continuously records until the trigger is activated at which point it stops recording and saves the last 8,188 images recorded. Once all lasers and cameras were positioned and focused, the data acquisition system began recording. The mechanism was then turned on. After a few seconds of flapping, the triggering device was pushed to stop the image acquisition; then the mechanism was turned off. Images from each camera were saved for two consecutive cycles. The flapping frequency was determined from the number of images for a cycle.

Validation of the laser dot projection technique was done by comparing photogrammetry results using marked targets to photogrammetry results using laser projected targets for a stationary wing. The curved tube frame wing was used in the validation. The wing surface was marked with a marker, placing dots at approximately the same spacing as the laser grid. The marked wing was attached to the mechanism, and the mechanism mounted. The wings were positioned at the midstroke, and the mechanism taped so that the wings could not move. The lasers were positioned so that the grid covered approximately the same area as the marker dots, and the cameras were focused on the wing and reference dots as before. The lasers were turned off, and a few images were taken of the stationary wing at a shutter speed of 1/125 seconds. This

allowed sufficient light to clearly see the marker targets. The lasers were then turned on, taking care not to touch the mechanism or the cameras. The shutter speed was adjusted to 1/1000 seconds which was fast enough to allow the laser dots to over-power the marker dots, but slow enough to allow the reference dots to be clear. A few images were taken of the stationary wing with the laser grid. This procedure gave images of an identical wing using two different methods.

Calibration allows PhotoModeler to take things like lens distortion, focus distance, and zoom into account when determining the 3D location of points. Calibration of the cameras was done after every test session, or any time the cameras were adjusted. Each camera was calibrated independently, according to instructions from the PhotoModeler software. The calibration grid used is shown in Figure 40. The data acquisition system has the ability to record a single image each time the trigger is pushed. This method was used to take 12 images of the calibration grid for each camera.

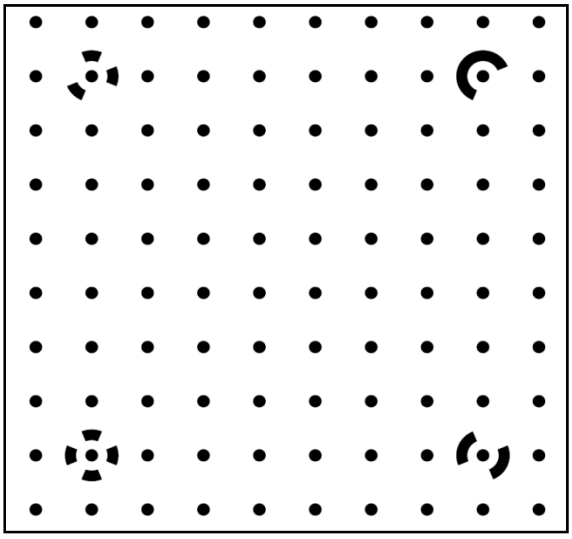

**Figure 40: PhotoModeler Calibration Grid**

By mounting the calibration grid to a flat plate, images could be taken at multiple angles by simply rotating and tilting the grid. PhotoModeler requires 12 images taken of the grid; three different tilt angles from each of the four directions. Multiple grid sizes were made available, and the one that covered the most area in the field of view while in focus was selected. An example calibration images is shown in Figure 41.

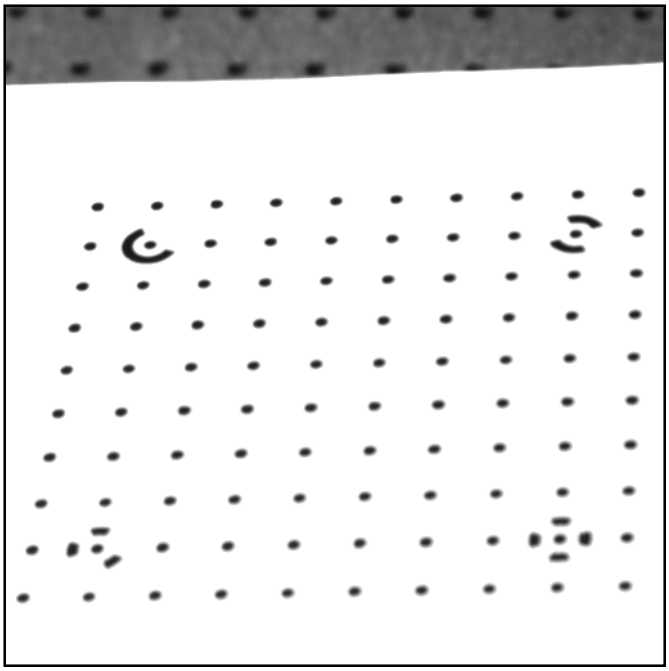

**Figure 41: Example Calibration Image**

After all of the images, and calibration images were taken, photogrammetry could be accomplished. The first step was to perform calibration within PhotoModeler for each camera. A camera calibration project was selected, and the calibration images from one camera imported. Camera calibration was run. The camera calibration project was saved. This was done for each of the four cameras.

Once all of the cameras were successfully calibrated, a PhotoModeler Video (PMV) project was started. The images to be analyzed were imported and matched to the

camera calibration file corresponding to the camera used to record the images. The PMV project is set up in multiple epochs; each epoch contains four images, one from each camera, that correspond to the same point in time.

The process was begun by marking points in the first epoch to be analyzed. The laser dots and the reference frame dots were marked using sub-pixel marking. This is a precise method for consistently marking the center of a light or dark multi-pixel target. Many of the dots were marked automatically, but some were done manually.

Once all of the dots on all the images were sub-pixel marked, they were referenced together. Referencing is a method of signifying which points in different images correspond to the same point in space. When enough points are manually referenced, PhotoModeler was able to orient the photos, meaning that 3D position information is calculated for each point. After the photos were oriented, automatic referencing was done for the rest of the points. The reference dots were then used to identify the origin, the scale, and the x and y axis directions. By processing the project, the 3D locations of the points are adjusted to the assigned coordinate system.

Each point is assigned a residual when the epoch is processed. A table of residual values is a valuable tool for determining if there are points with large marking residuals. Marking residuals are discrepancies between where a mark is on a given photo and where the program interprets the mark's location on the photos taken from different camera angles. Errors in marking and referencing were corrected until all of the residuals were less than one pixel for each camera view. The value and direction of the residuals could also be viewed using vectors at each point in each photo. This tool was used to ensure

that the residuals were in random directions. Residuals that point in the same direction or in a circular pattern could be a sign of a bad calibration.

One of the potential drawbacks of laser dot projection versus printed dot photogrammetry is that when the targets are projected onto the surface they move along the contour of the surface. Meaning that for each image in time, a given laser dot is in a different place on the surface of the wing. This allows for an overall view of changes in the wing's contour, but does not provide deflection data of each point on the wing. When viewing the three dimensional position of the points after processing, boundaries cannot be determined using only laser dot projection. To help with this visualization, four additional points were added; one at each corner of the wing. Since there was no target on the corners of the wing these points were not sub-pixel marked; they were placed manually by placing a mark on the image where the corner appeared. Inconsistency in this marking method increases the inaccuracy of the corner points, although the accuracy of the corner points is not as critical as they only serve as a reference frame to help visualize the outline of the wing.

Once an epoch was processed successfully, a tracking tool was used to move to the next epoch. PhotoModeler has two options for tracking points, 2D tracking and 3D tracking. The 3D tracking option was used. In this method the initial point for search in the photos in the new epoch is found by projecting the 3D position of each point from the previous epoch onto the photos in the new epoch. For the most part, the automated tracking method accurately tracks and references the points, but it is not perfect. To keep the accuracy of referencing, and marking in each epoch, the tracking was done one frame

at a time. Referencing and marking was adjusted as required to ensure accuracy before moving to the next epoch.

A screen shot of PhotoModeler is shown in Figure 42. The four photos are in the center, each with marked points, shown as crosses, corresponding to the centroid of the laser dots. The 3D viewer to the right was a useful tool to ensure that the overall shape of the wing was as expected. A 'points quality' table, located below the 3D viewer, was used to view the residuals of all of the points, and to help find points that were poorly marked or referenced.

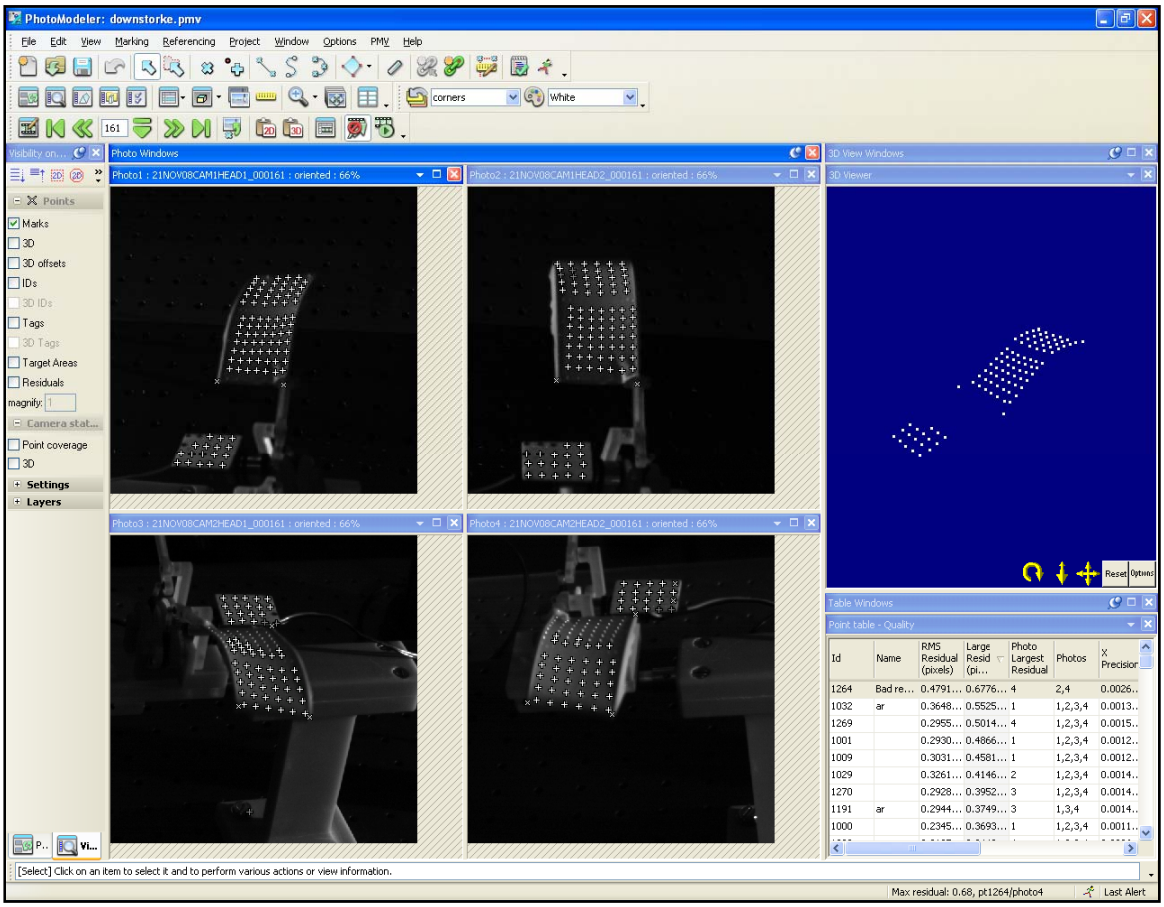


**Figure 42: PhotoModeler Screen Shot**

The same process was used for the stationary validation. The marker dots were sub-pixel marked and referenced in one project, and laser dots in another. As with all PhotoModeler analysis, the 3D position data was exported to a text file, and further analyzed in MatLab.

Due to the time consuming nature of the photogrammetry process, only portions of the stroke were analyzed. Additional lasers and additional camera angles may be needed if analysis of the entire stroke, particularly for a highly flexible wing, was desired. The midstroke had the best coverage from the laser grid, so 26 image sets from the downstroke and 26 image sets from the upstroke were analyzed for the tube frame straight wing and the tube frame curved wing. Initially these wings were chosen because they had little flexure during the stroke which provided a simple case for preliminary trial of the laser dot projection method. The portions of the stroke analyzed are shown in Figure 43 and Figure 44. A combination of a preference to use the frames with the best dot coverage, and a preference to look at the same location in the stroke for each case drove the selection of these locations.

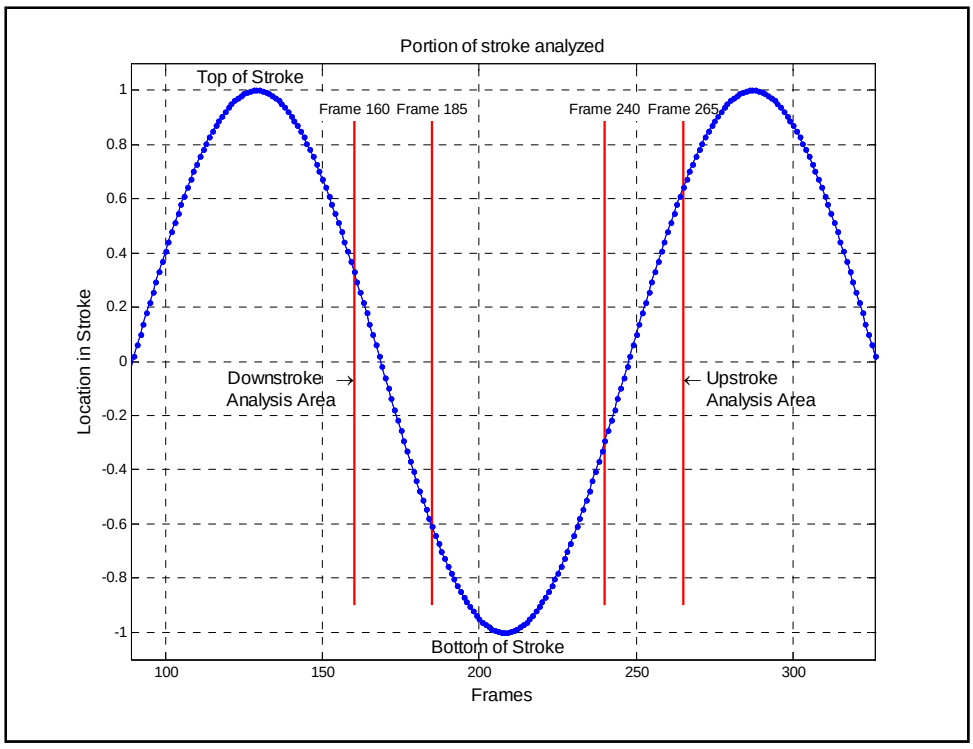


**Figure 43: Photogrammetry Analysis Area for Curved Tube Frame Wings**

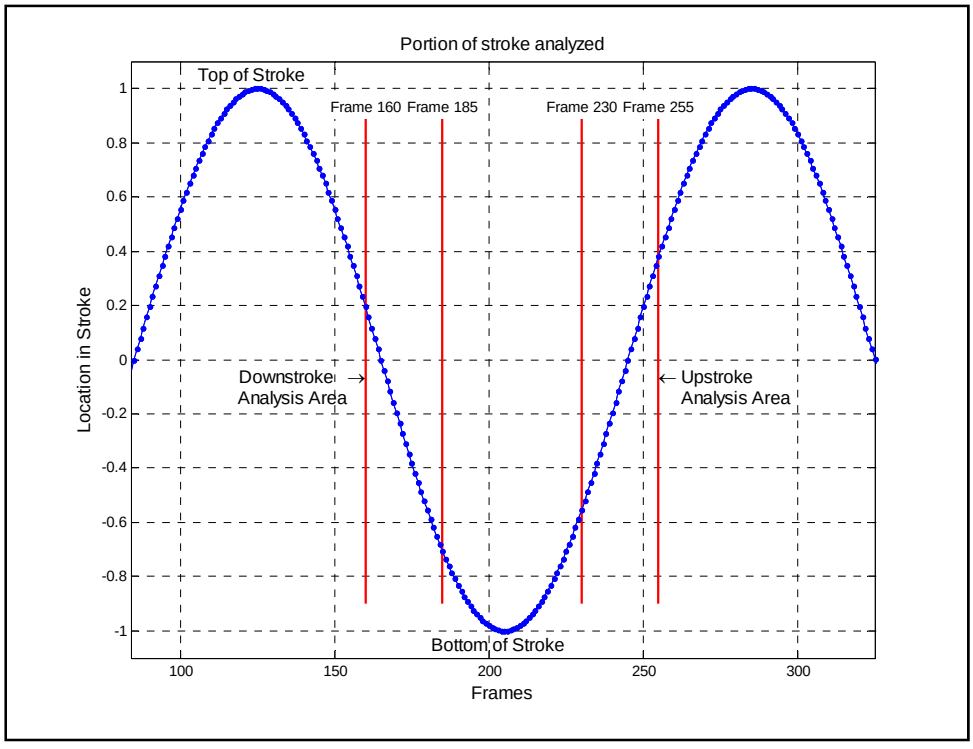


**Figure 44: Photogrammetry Analysis Area for Straight Tube Frame Wings**

Since the tube frame wings showed promising results, a wing with some flexibility was desired for analysis. For this reason the hybrid frame wing was developed and portions of its stroke analyzed. Thirty frames from the upstroke and downstroke were analyzed. The analysis area is shown in Figure 45.

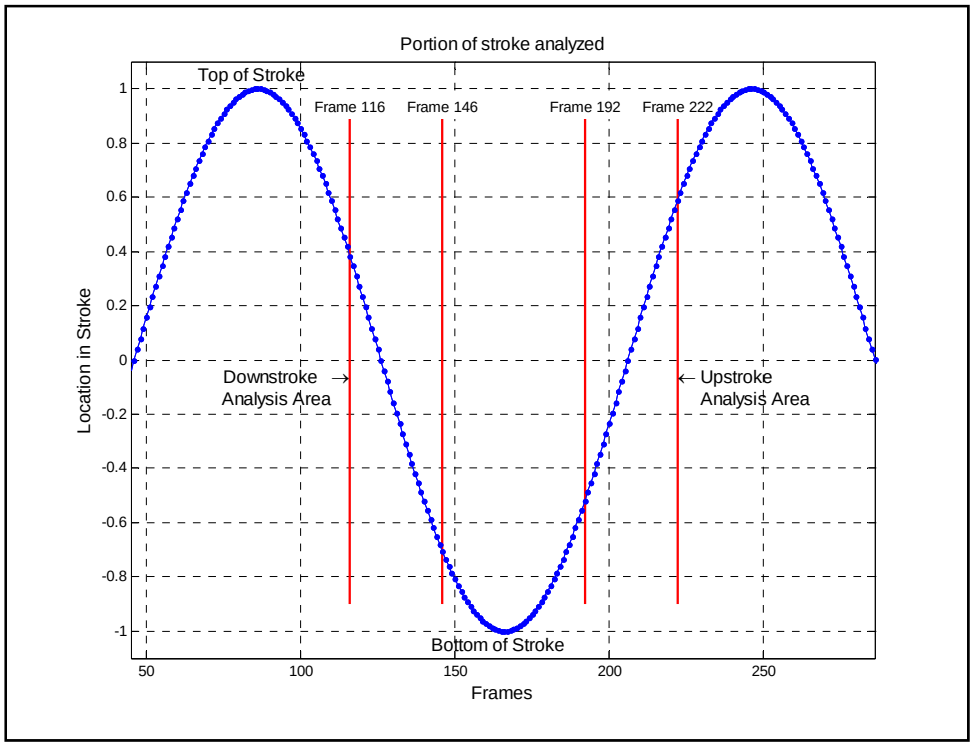


**Figure 45: Photogrammetry Analysis Area for Hybrid Frame Wings**

For the validation of the laser dot projection method, comparison to traditionally marked targets was required. The images used for comparison are shown in Figure 46. Marker dots were placed on the wing so that there would be approximately the same number and same spacing as the laser grid. However, the marker dots and laser dots are not located at exactly the same position on the wing. Because they aren't located at the same place on the wing, comparing the photogrammetry results using the two methods was not trivial.

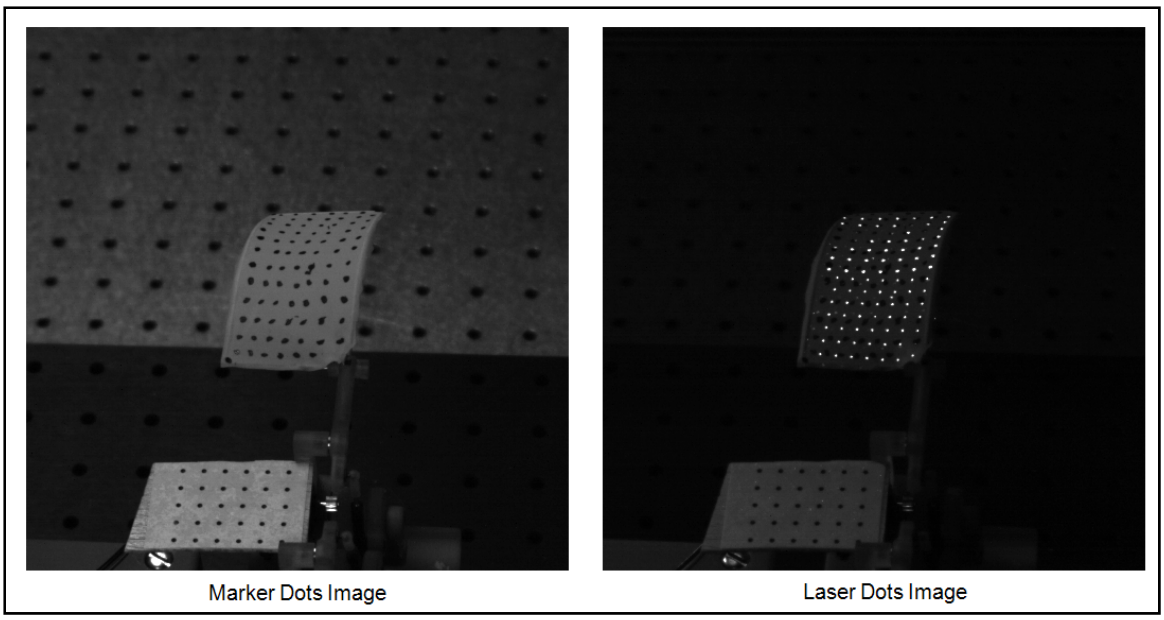


**Figure 46: Images Used for Comparison of Marker Dots to Laser Dots**

In order to compare the results, there needed to be some method of modeling the shape of the wing surface for each case. A type of interpolation was used to accomplish this task. Bicubic splines are traditionally used to estimate a function for a dependent variable over a grid of two, evenly spaced, independent variable. Because neither the marker dots nor the laser dots are exactly evenly spaced, a traditional bicubic spline routine could not be used on the data points. Instead, a radial basis function method was used. MatLab codes, developed by Travis Wiens and available from the MathWorks website, were used to apply this radial basis function method (Wiens, 2008). The codes are available in Appendix B.

The radial basis function method considers that every known point affects every other known point according to some function, the radial basis function, of the radial distance between the two points (Press and others, 2007). The radial distance between two points is taken as the square root of the sum of the squares of the difference in each

independent variable. In this case the x and y values of the points are treated as the independent variables. The below equation from *Numerical Recipes* is the basis for the radial basis function method.

$$z_j = \sum_{i=1}^{N_k} w_i \phi(r_{j,i}) \tag{8}$$

In Equation 8, $z_j$ is an element in a vector of the dependent values, in this case the z-value of the known points; $N_k$ is the number of known data points gathered from the photogrammetry process; $\varphi(r)$ is the radial basis function described later; and $w$ is a vector of $N_k$ length which represents the weight of each of the radial basis function values. The radial basis function is a function of the radial distance, $r_{j,i}$, between the $j^{th}$ known or unknown point, and the $i^{th}$ known point. The radial distance is found from the difference in the x-value of the two points, $\Delta x_{j,i}$, and the difference in the y-value of the two points, $\Delta y_{j,i}$, as shown in Equation 9.

$$r_{j,i} = \sqrt{{\Delta y_{j,i}}^2 + {\Delta x_{j,i}}^2} \tag{9}$$

$$\Delta x_{j,i} = x_j - x_i \tag{10}$$

$$\Delta y_{j,i} = y_j - y_i \tag{11}$$

In Equations 9-11, $x$ and $y$ are vectors of the x-values of the known points and the y-values of the known points respectively, each of these vectors is of length $N_k$. The radial distance, $r$, of each point from each other point, is determined from the magnitude of the vector between the two points in the x-y plane, as shown in Equations 9-11. These radial distances are inputs to the radial basis function from Equation 8. Essentially this method assumes that the z-value of each known grid point is based on a linear combination of the weighted radial basis function, $\varphi(r)$, evaluated at each value of $r$.

The left hand side of Equation 8 is the z-value of the $j^{th}$ known grid point. This leaves the values of *w*, the weights, as the only unknowns. The *w* vector is of size 1 x $N_k$. Evaluating Equation 8 for a single known grid point results in one equation with $N_k$ unknown values in the vector *w*. By evaluating this equation for each of the $N_k$ known grid points the system of equations is expanded to $N_k$ equations for $N_k$ unknown which can be solved linearly for the values of the vector *w*.

Once the values of *w* are found, Equation 8 can be used to find the z-value at any value of x and y within the region covered by the known grid. To do this, the radial distance between the desired point and every known data point is found with Equations 9-11, and the radial basis function evaluated for these radial distances. The weights are applied to the radial basis function values, and the results summed in accordance with Equation 8 to give the z-value for the input x and y values. This method gives a way of determining an estimate for the z-value at any value of x and y.

There are many different types of radial basis functions, *φ(r)*, presented in *Numerical Recipes*. Different functions were experimented with, and the thin-plate spline found to give satisfactory results. Equation 12 is the thin-plate spline radial basis function.

$$\phi(r) = r^2 \log\left(\frac{r}{r_0}\right)$$

$$\phi(0) = 0 \qquad (12)$$

The variable $r_0$ represents a scale factor which can be used to fine tune the results. In this case $r_0$ was set equal to one (Press, 2007).

The steps followed to utilize this method are as follows:

1) Create a $N_k$ x $N_k$ matrix containing all of the values of $r_{j,i}$ representing the radial distances between each known data point and each other known data point. Each row of the matrix would be the distance between the $j^{th}$ point and each other point. For instance, $r_{1,2}$ would be the radial distance between point 1 and point 2. It would be determined by Equations 9-11
2) Solve the radial basis function, Equation 12, for each value of $r$, giving a $N_k$ x $N_k$ matrix called $\Phi$.
3) Equation 8 can be expressed in matrix form using Equation 13. In Equation 13, the vector $z$, and the matrix $\Phi$ are known. Solving for the unknown, $w$, yields Equation 14. Evaluating Equation 14 gives the weights, $w$.

$$z = w * \Phi \tag{13}$$

$$w = z * inv(\Phi) \tag{14}$$

4) The weights, $w$, can then be used to find the value of the dependent variable, z, at any desired combination of independent variables, x and y. Define $x_d$ and $y_d$ as the combination of independent variables for which a z-value is desired. The radial distance, $r$, between each of the desired points and each of the known points is determined from Equations 9-11 by setting $x_j$ and $y_j$ equal to $x_d$ and $y_d$ respectively. This yields a matrix r of size $N_d$ x $N_k$, where $N_d$ is the number of desired points, and $N_k$ is the number of known gird points. Equation 12 is then solved for each point in the matrix $r$ to give $\Phi$.
5) Finally Equation 13 can be solved to give the z-value of all of the desired points.

The radial basis function method described above was done for the results from the marker dots and from the laser dots. Results were then compared by sampling at known x and y positions, and comparing the z position data. The same method was also used to model a surface for the hybrid frame wing and the curved wire frame wing.

# 4. Results

## 4.1 Force Measurements

Note that in all results shown, a negative axial force corresponds to positive thrust, while positive normal force corresponds to positive lifting force. Also note that all forces are expressed in grams instead of newtons; conversion to newtons would be required for calculation of any thrust of lift coefficients.

The wire frame wings were used to validate the force balance measurements by comparing the axial force measurements taken using the air bearing table to measurements taken using the force balance. Figure 47 shows axial force data acquired with the load cell and axial force data acquired with the force balance taken at the same time. The load cell validates the capability of the balance; small differences could be attributed to friction in the air bearing table, or disruption of airflow from the wings by the balance stand.

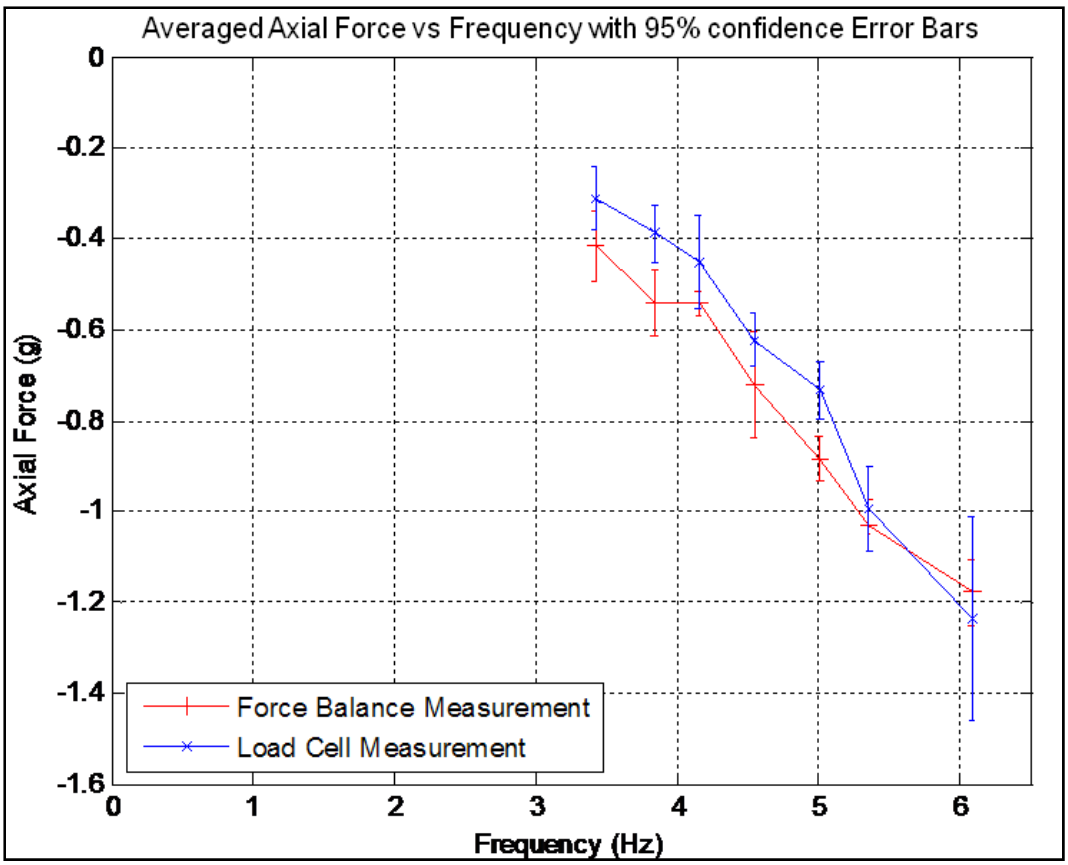


**Figure 47: Axial Force Comparison of Load Cell and Force Balance Measurement Techniques**

From Figure 48 and Figure 49 it can be seen that the spanwise camber of the wing does have an effect on the production of a normal force (z-direction). For both the tube frame wings and the wire frame flexible wing, the cambered wing produces higher normal forces than an identical wing without spanwise camber. This is consistent with the findings of Hong and Altman, who found that for a wing with spanwise camber, more positive force is produced on the downstroke than negative force produced on the upstroke (Hong and Altman, 2006). The spanwise camber does not apparently produce the same axial force for this particular wing geometry. For the wire frame flexible wings, the straight wings produced more axial force than the curved wing, while for the rigid

tube frame wings there was no increased axial force with increased frequency for either wing set. Notice, from Figure 48, that there is a spike, at approximately 4.1 Hz, in the measured normal and axial forces taken from the curved tube frame wing set. Investigation into data sets near this spike revealed that a flapping frequency of approximately 4.1 Hz for this wing set yields a lower ratio of standard deviation to mean than data sets taken at higher and lower flapping frequencies. Resonance could be playing a role, but work is needed in this area to clarify the cause. Further investigation would be required to draw concrete conclusions regarding the reasons for the spikes in normal and axial force.

Comparison of the straight wings, including the hybrid wing, is shown in Figure 50. The axial force for the wire frame wing is significantly higher than for the tube frame wing. This could be due to the fact that the wire frame wing is significantly more flexible then the tube frame wing. Ho and others observed that flexible wings in flapping produced thrust, while stiff wings did not (Ho and others, 2003). Since the attachment point of the wings is at the leading edge, the flexibility will cause the trailing edge to lag behind the leading edge, as demonstrated by Heathcote, Martin, and Gursul and as is evident from Figure 59, at least for a significant portion of the upstroke and downstroke. This lag essentially causes a positive pitch angle on the upstroke and a negative pitch angle on the downstroke, or essentially a positive angle of attack with regard to the motion through the air throughout the stroke. This allows axial force to be produced in the forward direction throughout the stroke (Heathcote, Martin, and Gursul, 2004). Minimal normal force was produced by any of the straight wings, although the hybrid wing did produce some increase in normal force with increased flapping frequency.

A comparison of the wings with spanwise curvature is shown in Figure 51. Notice that the rigid tube frame wing produced more normal force then the flexible wire frame wing. Because of the curvature of the wing, when the airflow is impinging on the top of the wing, as in the upstroke, the surface is more aerodynamic than when the airflow impinges on the bottom of the wing, as in the downstroke. This could attribute to the increased normal force for the curved wings. The rigidity of the tube frame wing ensures that overall shape of the wing is upheld throughout the stroke, while the flexibility of the wire frame wing could also be contributing to the normal force production as will be discussed later.

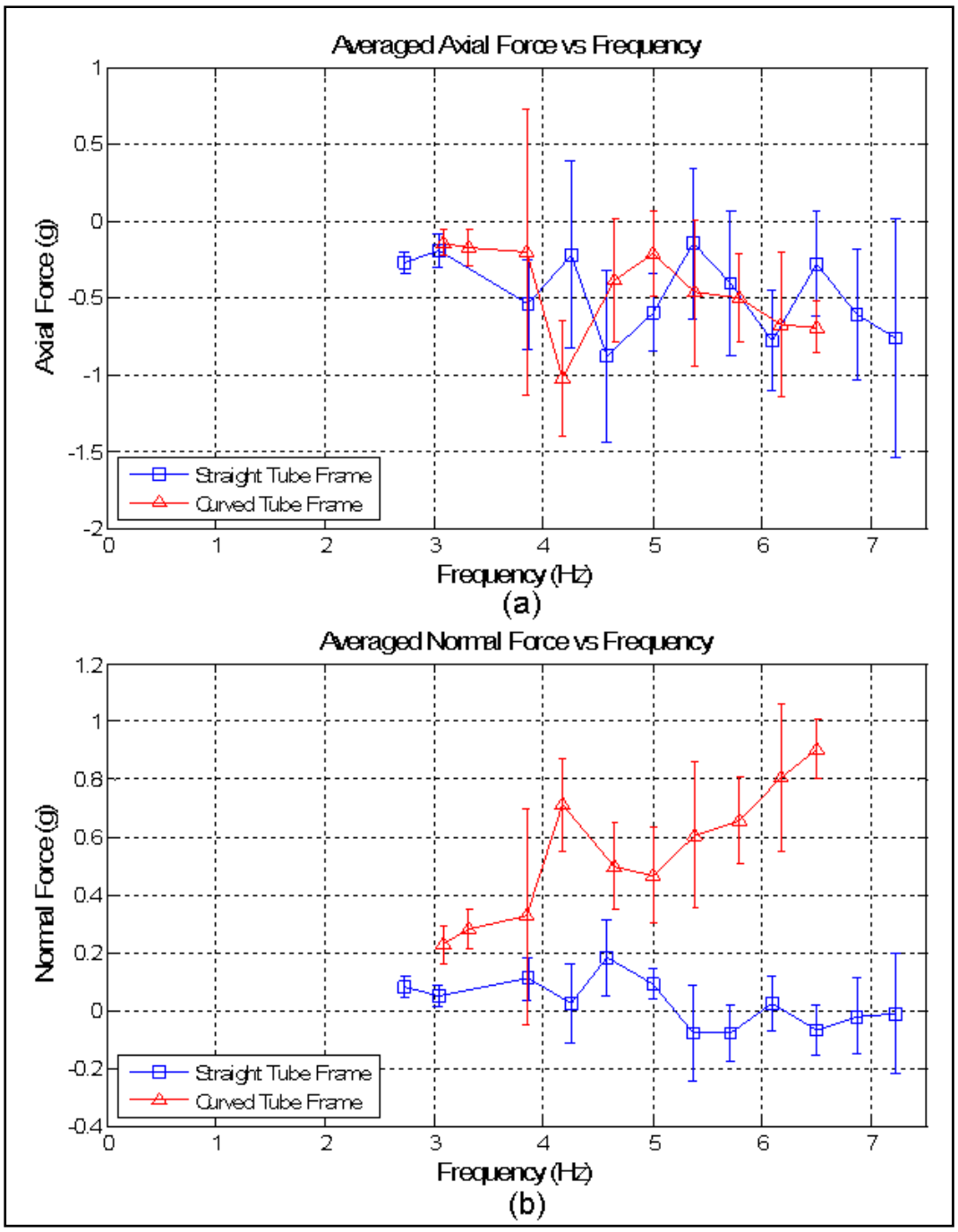


**Figure 48: Force Comparison for Straight and Curved Tube Frame Wings with 95% Confidence Error Bars (a) Axial Force (b) Normal Force**

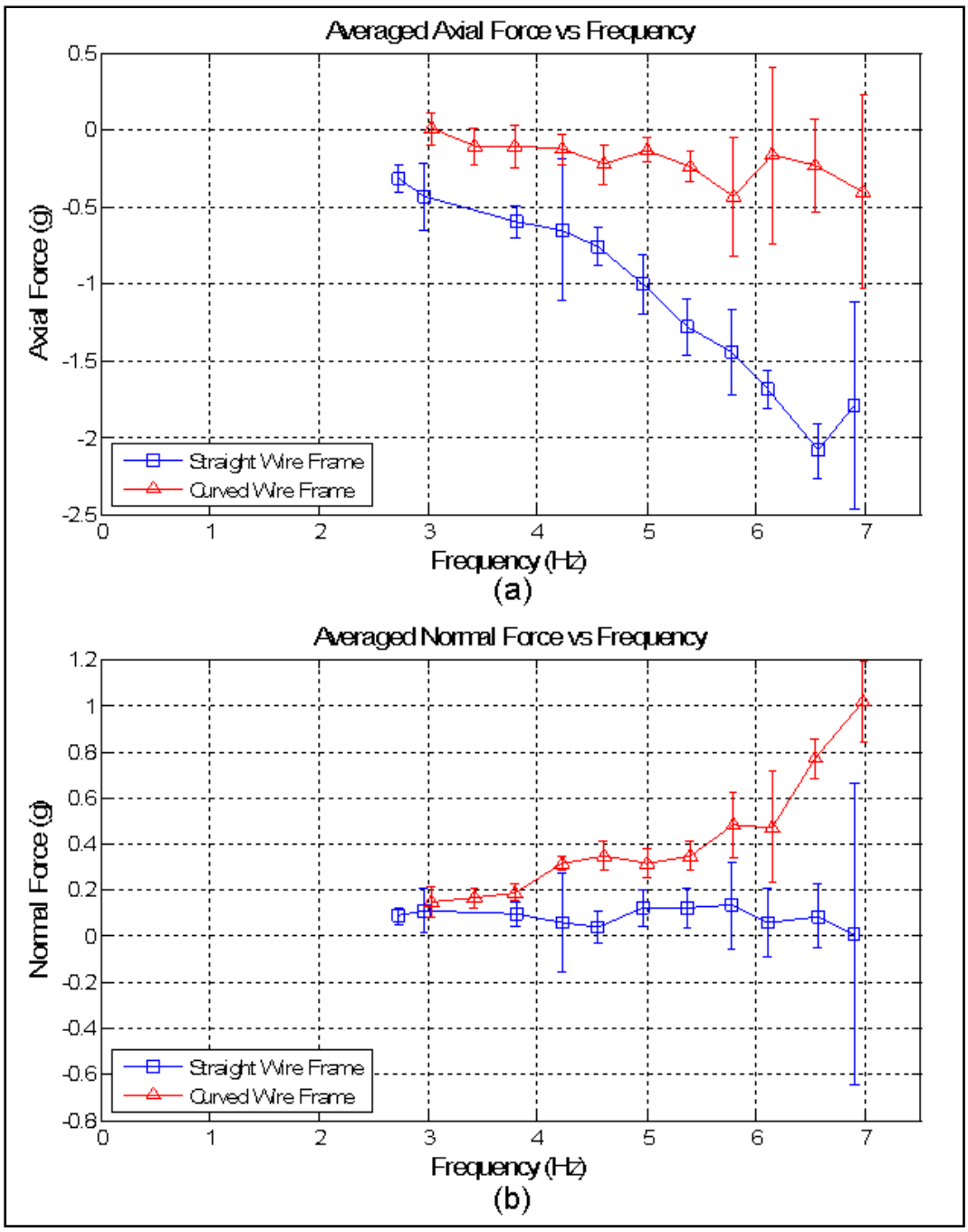


**Figure 49: Force Comparison for Straight and Curved Wire Frame Wings with 95% Confidence Error Bars (a) Axial Force (b) Normal Force**

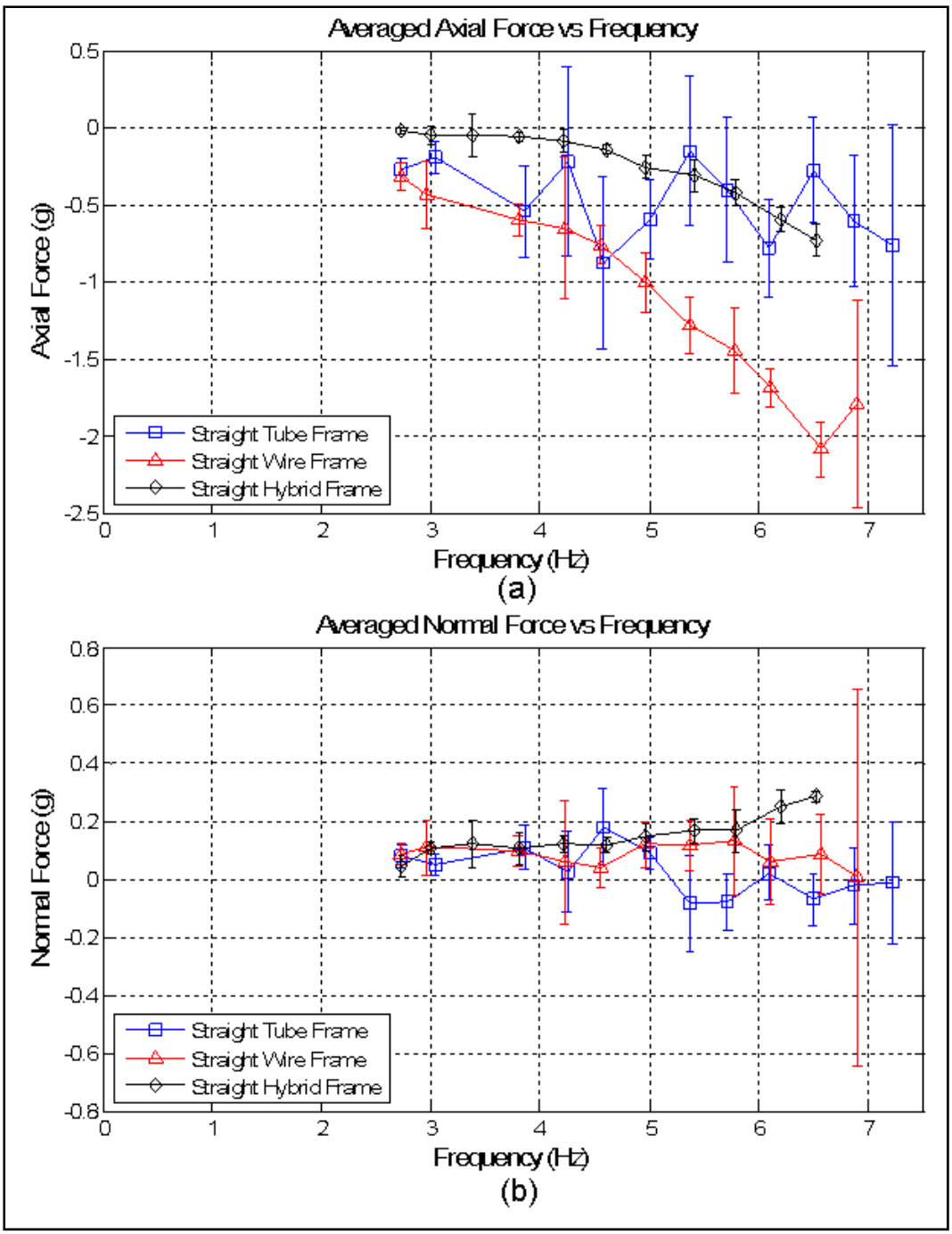


**Figure 50: Force Comparison for Different Frame Straight Wings with 95% Confidence Error Bars (a) Axial Force (b) Normal Force**

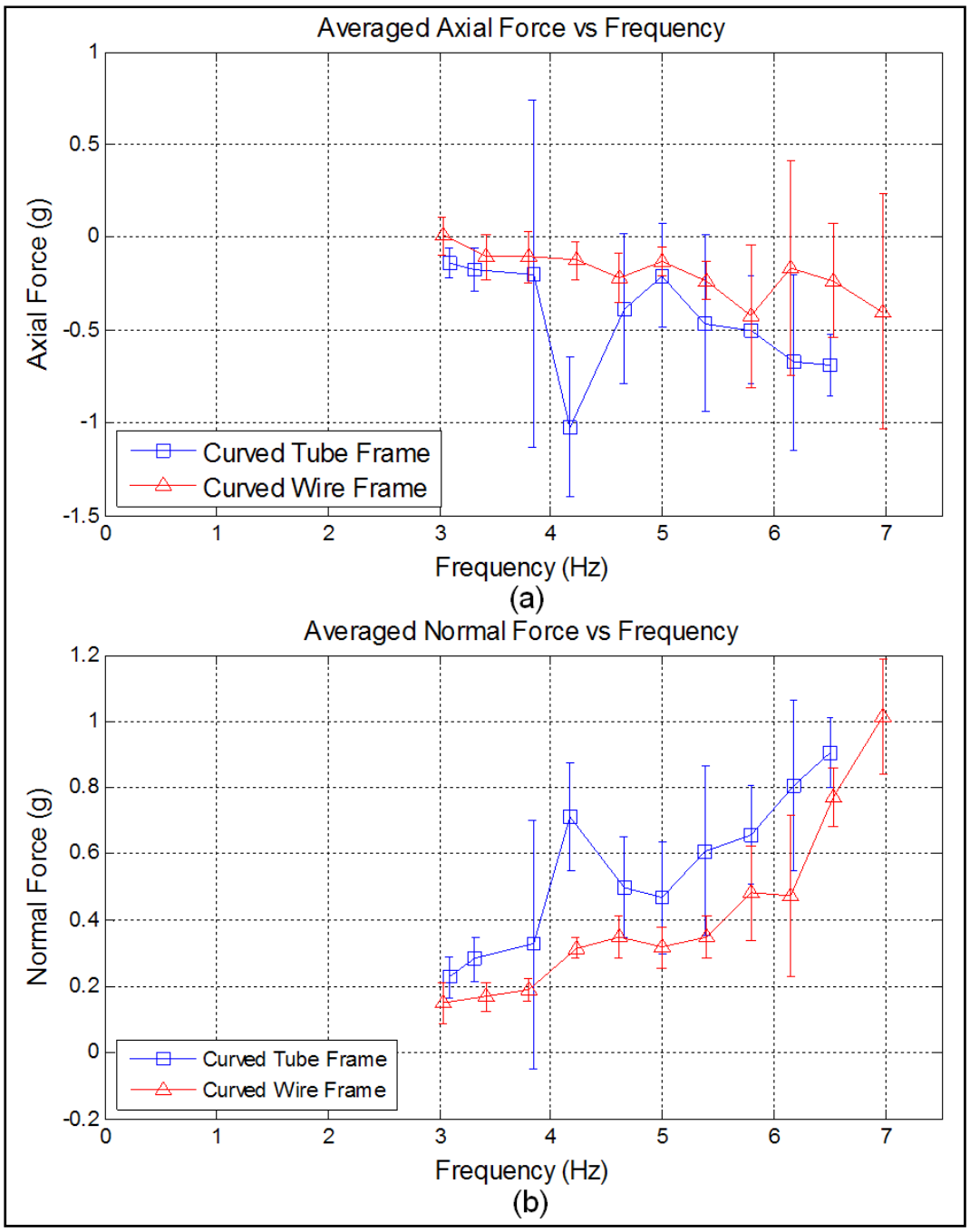


**Figure 51: Force Comparison for Different Frame Curved Wings with 95% Confidence Error Bars (a) Axial Force (b) Normal Force**

Most testing was done with the one degree-of-freedom flapping mechanism, but some force data was taken from the two degree-of-freedom flapping with pitch

mechanism. The rigid tube frame straight wings were used with the two degree-of-freedom mechanism. The results are compared to the results from the one degree-of-freedom mechanism using the same wings; they are shown in Figure 52. Notice that by pitching the wing to provide for a positive angle of attack throughout the stroke, axial force is produced. The results are in-line with the finding of many other researchers (Isaac, Colozza, and Rolwes, 2006; Birch and Dickinson, 2003; Jadhav and Massey, 2007; Wilson and Wereley, 2007).

Measurements were also taken with the two degree-of-freedom mechanism operating in the reverse direction. The motor leads were switched so that the wing always had a negative angle of attack, in other words the wing pitch was positive on the downstroke and negative on the upstroke. The results are shown in Figure 53. As expected, the wing produces positive axial force when the rotation was reversed, although more net force was produced when the mechanism was used as designed. Since the connection point is at the leading edge, any additional passive pitching of the wing due to aerodynamic or inertial forces is such that it will add to the active pitching when the mechanism is operated in the proper direction. When operated in reverse, the additional passive pitching of the wing will subtract from the active pitching. The increased normal force when operated in reverse is curious. Further analysis would be required to draw conclusions regarding the cause.

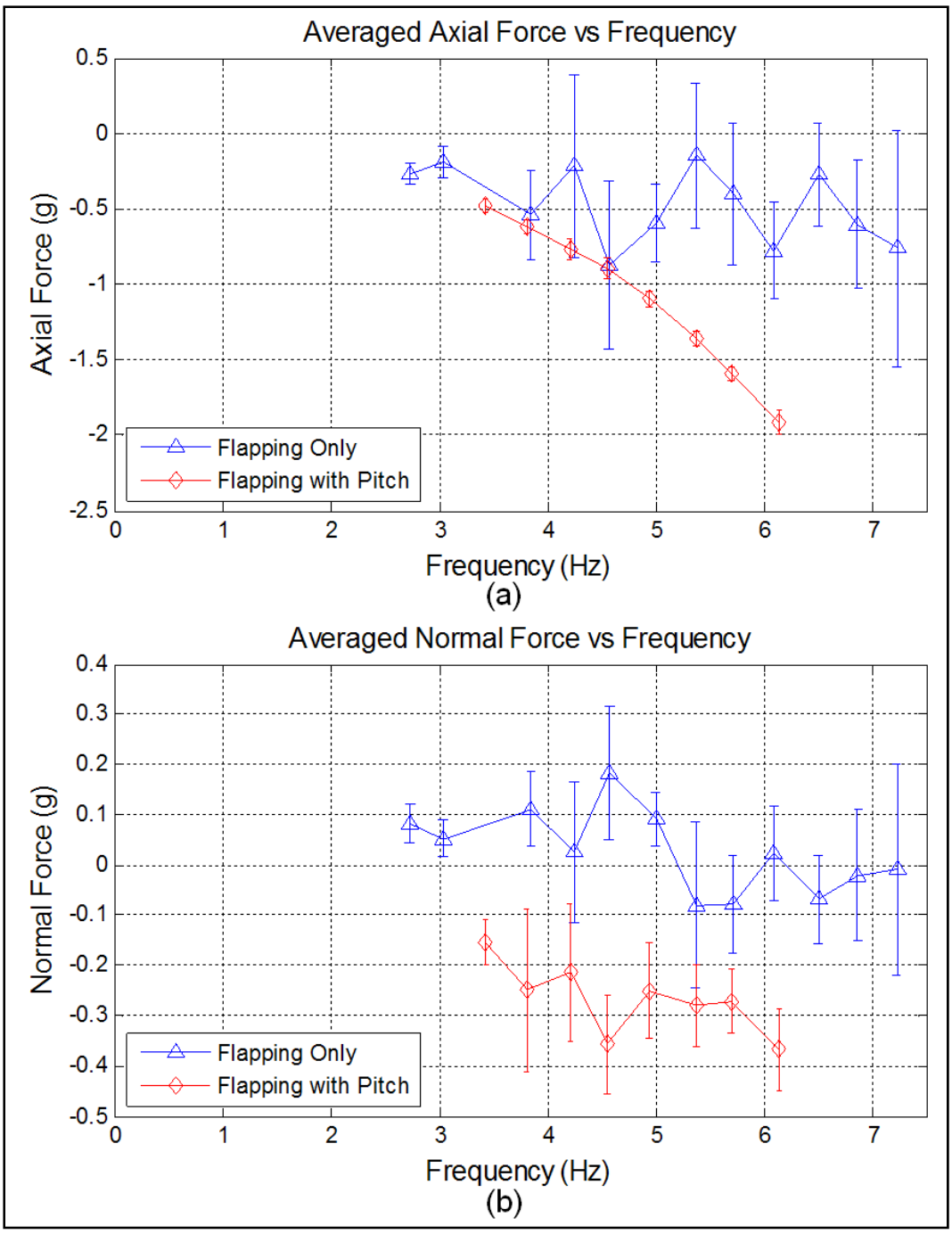


**Figure 52: Force Comparison for Straight Tube Frame Wings in Different Mechanisms with 95% Confidence Errorbars (a) Axial Force (b) Normal Force**

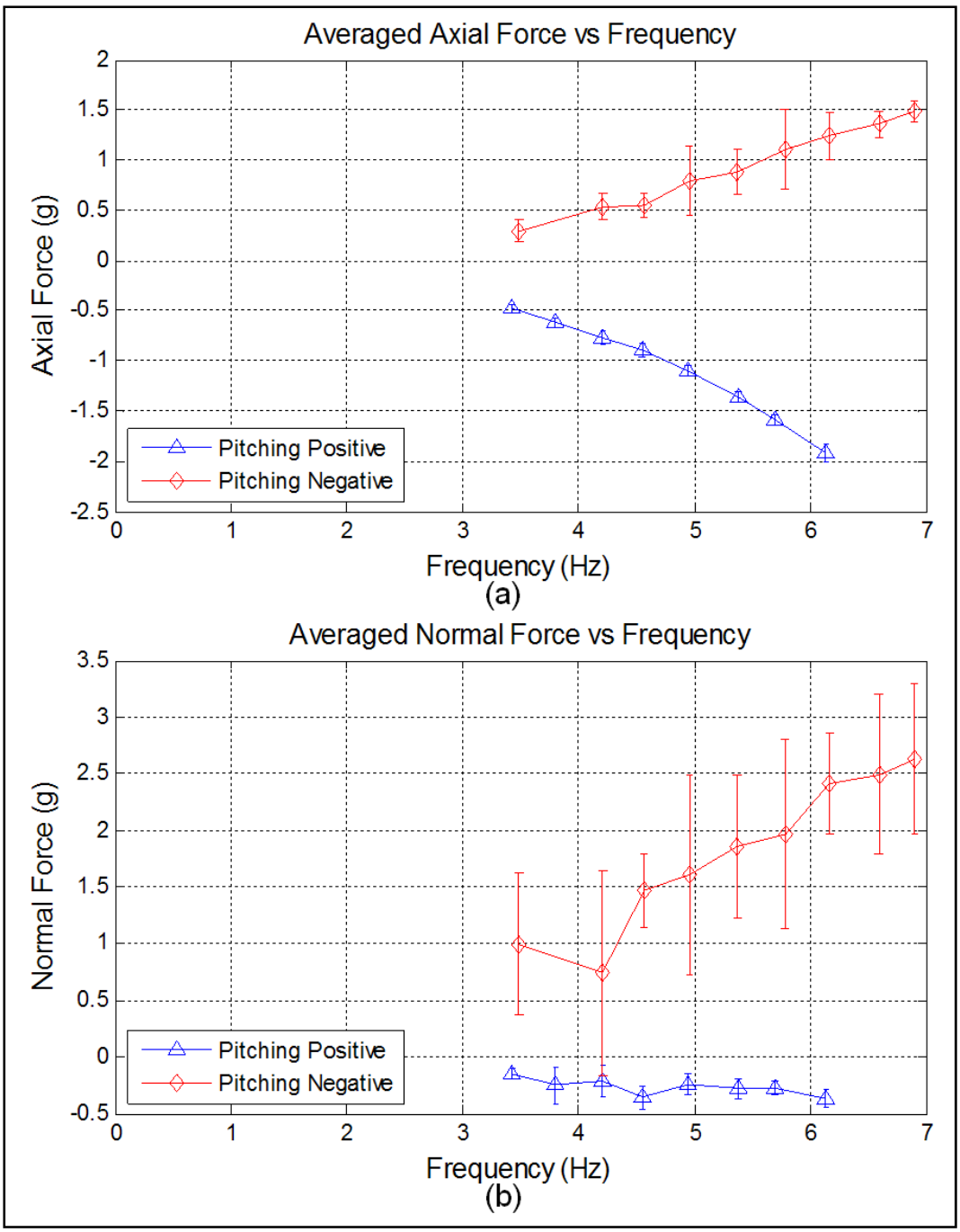


**Figure 53: Force Comparison for Operation of Flapping with Pitch Mechanism with 95% Confidence Errorbars (a) Axial Force (b) Normal Force**

Although the time averaged force data was used for most analysis, the time-accurate force data was also taken. Data sets from the tube frame and the wire frame

wing sets with a flapping frequency of 6.25 Hz are presented. The averaged axial force at this frequency was higher for the flexible wire frame wing then it was for the rigid tube frame wing. The temporal axial and normal forces over four cycles are shown in Figure 54. The third set of data in the plot represents the magnitude of the forces when the mechanism is flapped with no wings attached. The cross-correlation of the data sets was used to determine the time shift that would best match the signals.

Notice that a higher peak magnitude of force is produced by the more rigid tube framed wing. The rigid nature of the wing forces it to completely change direction more rapidly at the beginning and end of each stroke. More force is transferred to the mechanism in order to quickly stop the inertia of the wing. The fact that the forces from the tube frame wings had a wider range throughout the stroke can be quantified by looking at the standard deviation. Over the time period plotted in Figure 54, the standard deviations for the tube frame wings were 117 grams and 50 grams for the normal and axial forces respectively. While for the wire frame wings the standard deviations were 60 grams and 35 grams for the normal and axial forces respectively. The standard deviations for the mechanism flapping with no wings were 11 grams and 6 grams for the normal and axial forces respectively. Measuring the mechanism with no wings can serve as a method of quantifying the noise in the signal generated only from the operation of the mechanism.

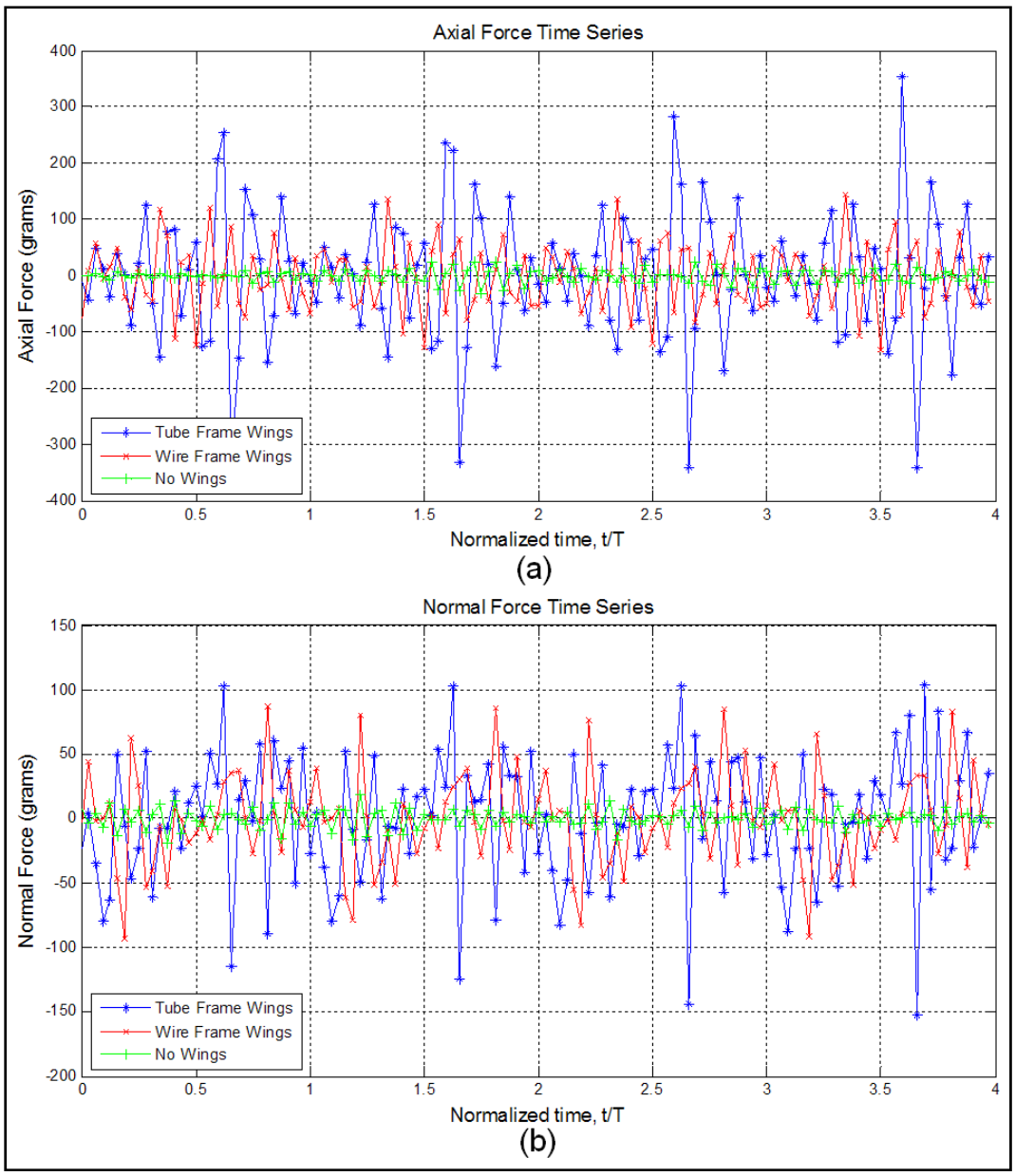


**Figure 54: Temporal Axial and Normal Force Data for Straight Tube and Wire Frame Wings Flapping at 6.25 Hz (a) Axial Force (b) Normal Force**

Data taken when flapping only the frame can give a means of estimating the inertial forces involved in the cycle. This was done for the straight tube frame wing. The membrane was removed, the frame was attached to the mechanism, and it was flapped at approximately 6.2 Hz. The temporal results are shown in Figure 55. As can be seen,

flapping the frame produces a smaller range of forces than does flapping the wing. This shows that the forces generated from flapping the wings are a combination of the inertial and aerodynamic forces. Further experimentation, possibly through operation in a vacuum chamber, would be required to more accurately determine and subtract the inertial forces from the aerodynamic forces.

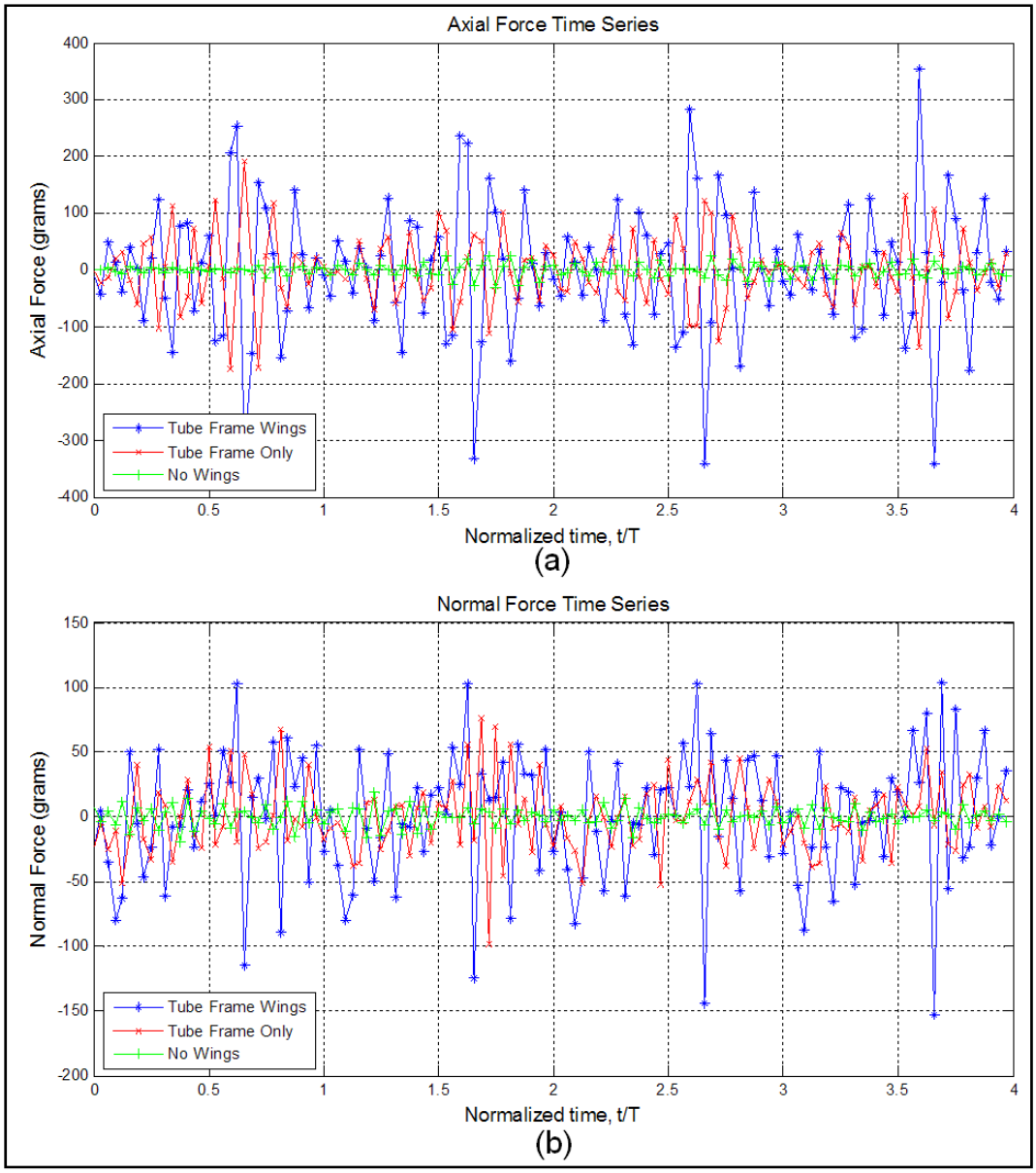


**Figure 55: Temporal Axial and Normal Force Data for Straight Tube Frame Wings and Frame Only flapping at 6.25 Hz (a) Axial Force (b) Normal Force**

Auto-correlation is a mathematical method of determining the consistency of a repeating pattern within a signal. An auto-correlation was done on the axial force data from the straight tube and wire frame wings. Comparison of the two auto-correlations is presented in Figure 56. Each auto-correlation was normalized by the square of the root mean square value for the data. This essentially sets the magnitude to one for zero lag.

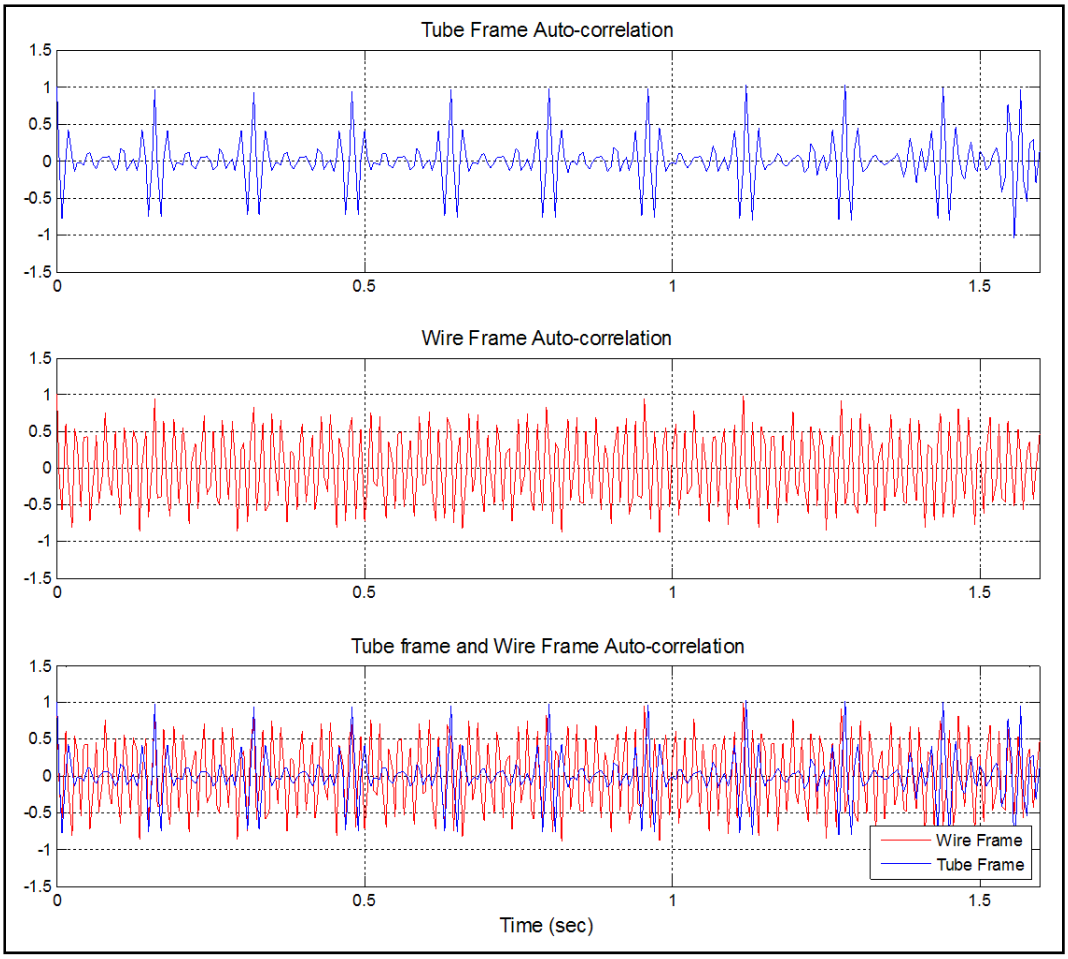


**Figure 56: Auto-correlation of Axial Force Time Series Data for Straight Tube and Wire Frame Wings (flapping frequency = 6.25Hz)**

The tube frame wing has slightly higher peaks at the multiples of each period. This suggests that the cycles are more consistent for the more rigid wing. The wire frame

wing has many peaks in between the multiples of the periods. This suggests that there are frequencies in the data other then the primary flapping frequency.

## 4.2 High Speed Images and Photogrammetry

Note that for all photogrammetry results, the axis is set so that the positive x direction is toward forward, or parallel to the axis of the balance. The positive y direction is positive out along the length of the wing, and the positive z direction is upward, and in the direction of the flapping motion.

Results of photogrammetry using marker dots on a still wing were compared to photogrammetry results using laser dots on the same still wing. The wing used was the curved aluminum frame wing. Figure 57 shows the 3D location of the dots from the two different methods.

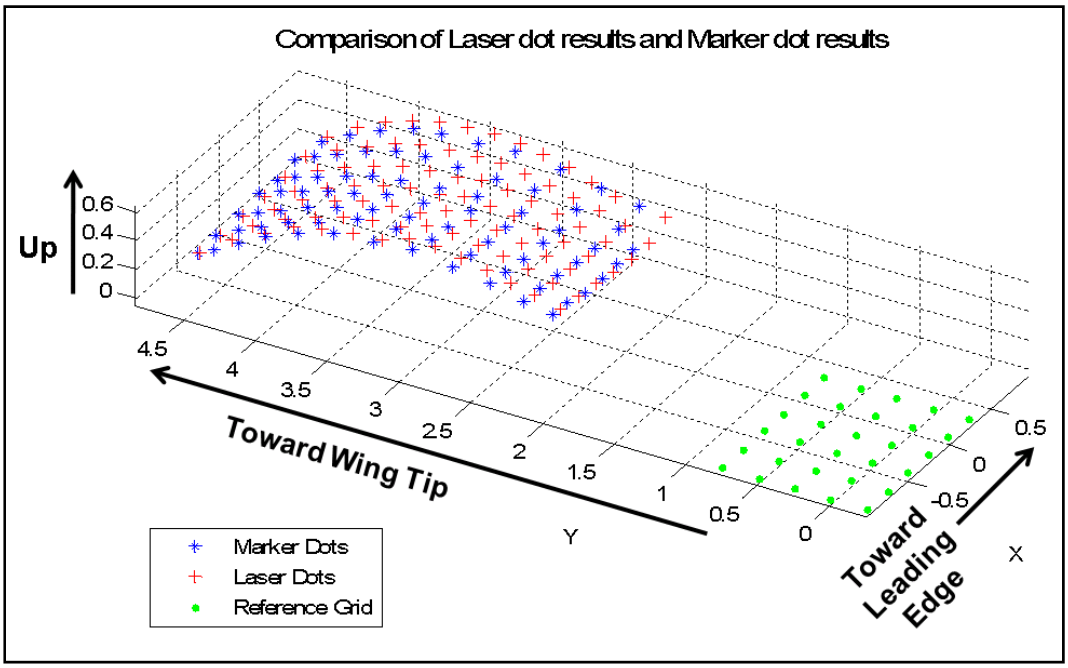


**Figure 57: Marker Dot and Laser Dot Photogrammetry Results**

The procedure outlined in section 3.2.2 was used to form a surface that could be used to estimate the location in the z direction. An evenly spaced grid of 20 x 40 points representing a 1" x 2" section in the center of the wing was used to compare the results. For each of the grid points, the locations in the z axis for the laser dot surface and for the marker dot surface were determined using the RBF method. The average of the absolute value of the difference between the z values of each of the grid points was 0.0109" with a standard deviation of 0.0079". This represents an average difference of approximately 0.4% of the wing's span. Figure 58 shows the surfaces created using the two different sets of data, evaluated over the evenly spaced grid. Notice that for approximately half of the wing, the marker dot surface is higher, while for the other half, the laser surface is higher. In fact, when the difference in the z values of the grid are averaged without taking the absolute values, the result is -0.00022". These results show very close correlation between the two methods, validating the laser dot projection method as an accurate method of determining the overall shape of a surface.

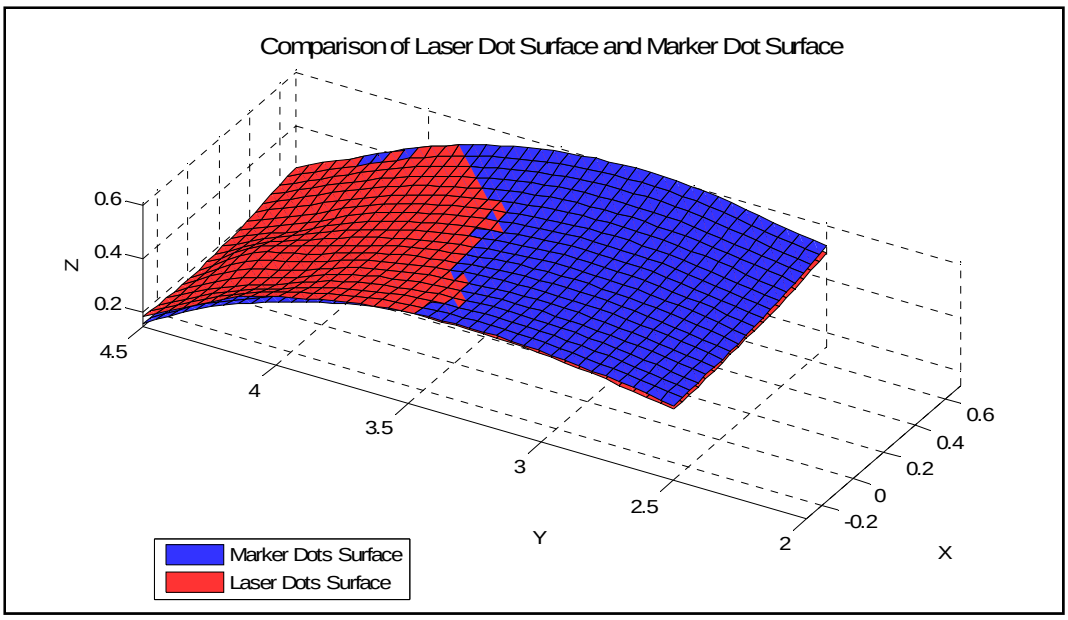


**Figure 58: Surface Comparison of Photogrammetry Results from Two Different Marking Techniques**

The next step was to utilize this method on the wing sets during flapping. All wing sets where photographed at 1000 fps while flapping at approximately 6.2 Hz. Figure 59 shows the wire frame curved wing and the wire frame straight wing at nine locations throughout the stroke. Labels show the position in the stroke, where T represents the flapping period and is equal to approximately 0.16 seconds. As can be seen, significant flexibility occurs during the stroke. The curved wing appears to be straightening on the downstroke and curving on the upstroke, which has been shown to be a characteristic of the flapping stroke of some birds (Pennycuick, 1989). This could contribute to the increased lifting force when compared to the straight wing. As anticipated, flexibility is also shown during flapping of the straight wire frame wing.

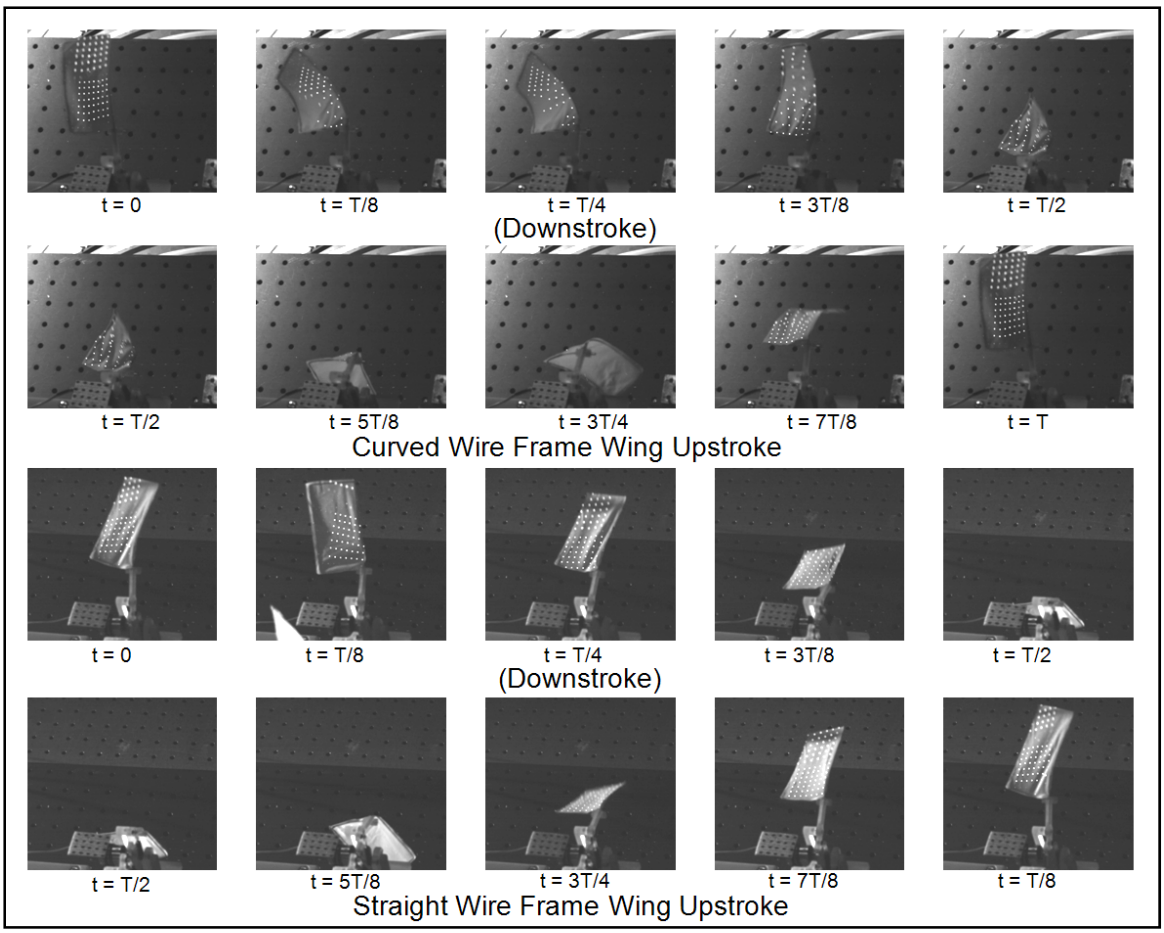


**Figure 59: Images Taken of Wire Frame Wings Flapping at 6.2 Hz, T is the Flapping Period**

A limitation of the laser dot projection method is demonstrated by taking a closer look at a few of the images from the curved wire frame wings during flapping. Figure 60 and Figure 61 shows all four camera views for two of the frames shown in Figure 59. Notice that in the first set of images, the laser dots provide relatively equal coverage over the entire wing, where as in the second set of images, there are hardly any laser dots visible on the wing. Since the laser dots are not attached to the wing, maintaining coverage throughout the stroke can be difficult, particularly for highly flexible wings. The use of additional laser grids could help to solve this problem. Another method may

be to first take high speed images of the wing during flapping and determine the general position of the wing at the portion of the stroke that is of interest. Then, focus the laser grids so that the wing is fully covered at that portion of the stroke.

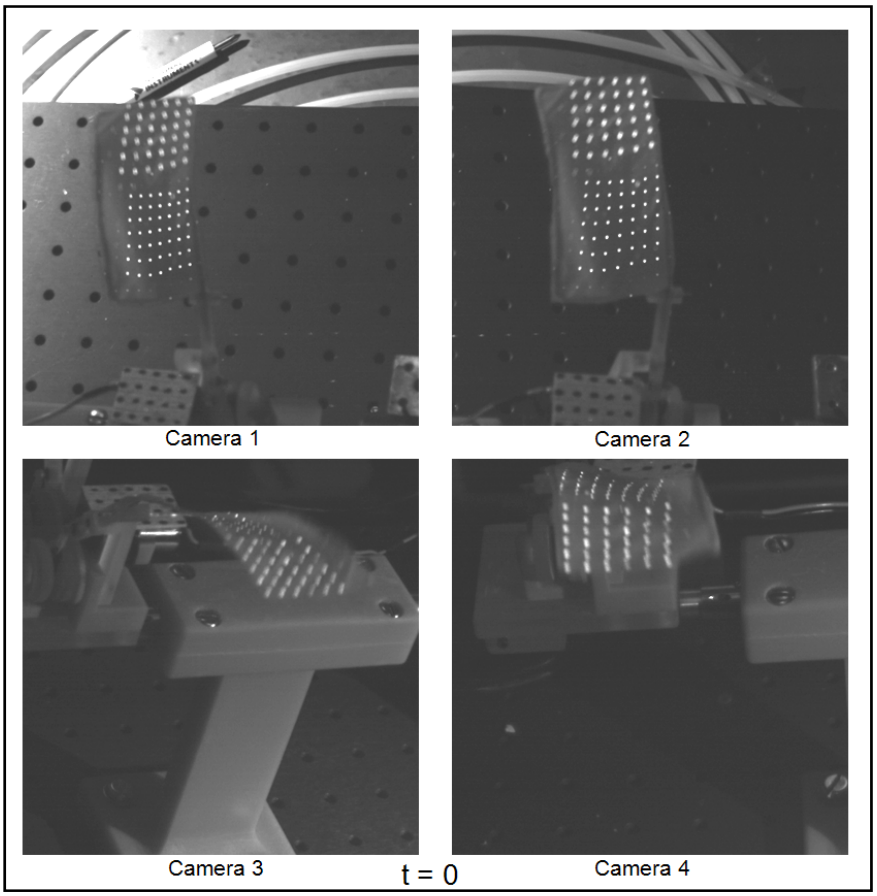


**Figure 60: Curved Wire Frame Wings during flapping from four camera angles with good laser grid coverage**

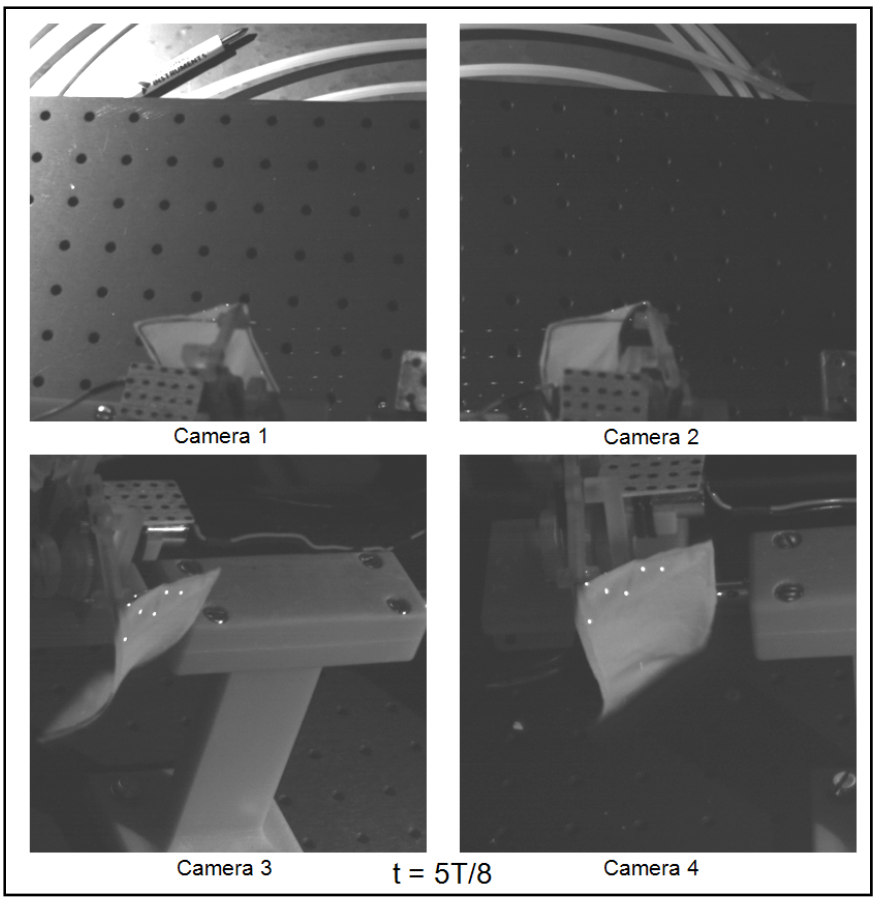


**Figure 61: Curved Wire Frame Wing during flapping from four camera angles with bad laser grid coverage**

Because of the highly flexible nature of the wire frame wings, and the challenges presented above, photogrammetry analysis was only performed on a two image sets from the curved wire frame wing, which will be discussed later. Images of the rigid tube frame wings are presented from all four camera angles in Figure 62 and Figure 63. As can be seen, there is no visible flexure of these wings throughout the stroke. This provides a simpler platform for initial testing of the laser dot projection technique.

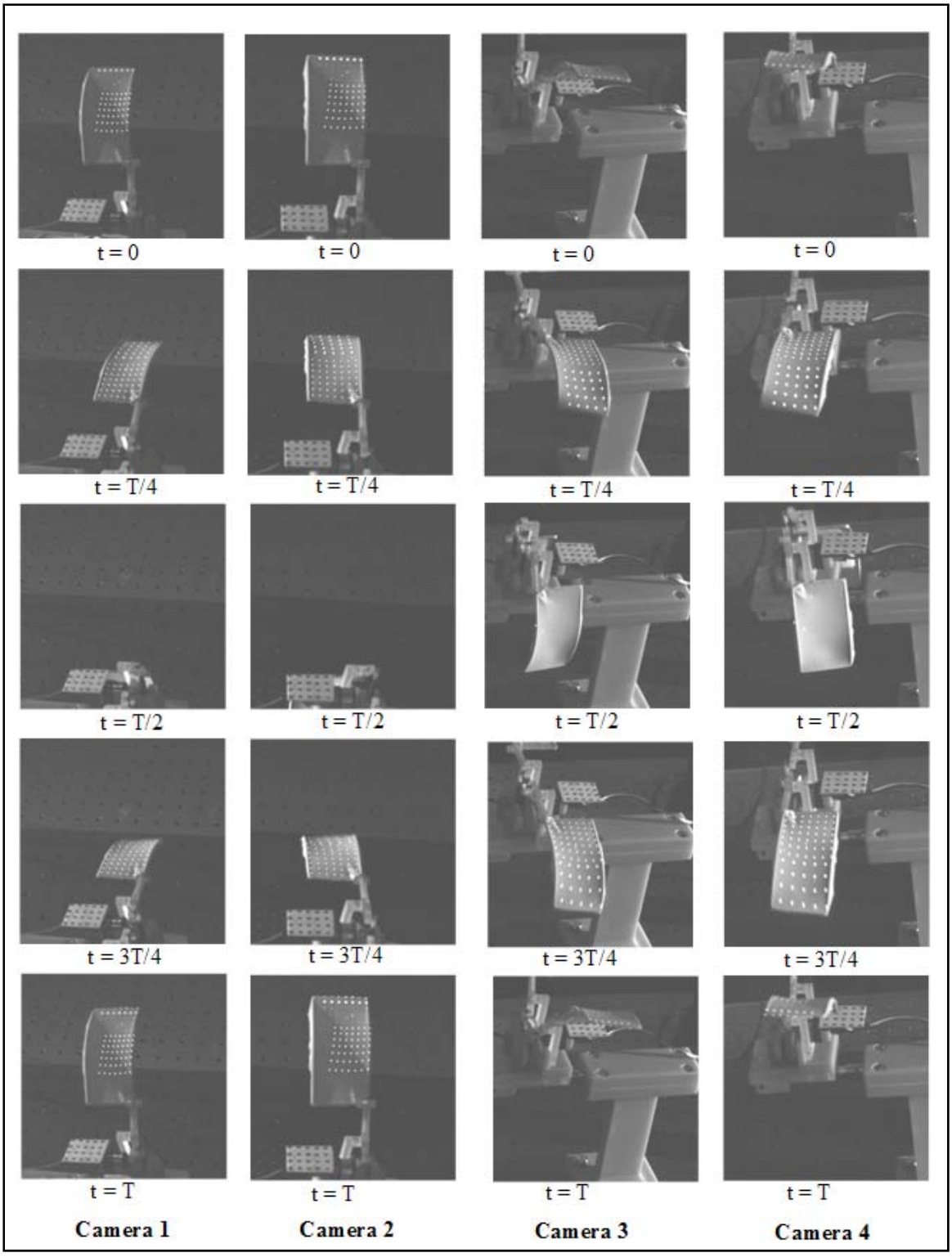


**Figure 62: Images of Curved Tube Frame Wing flapping at 6.2 Hz**

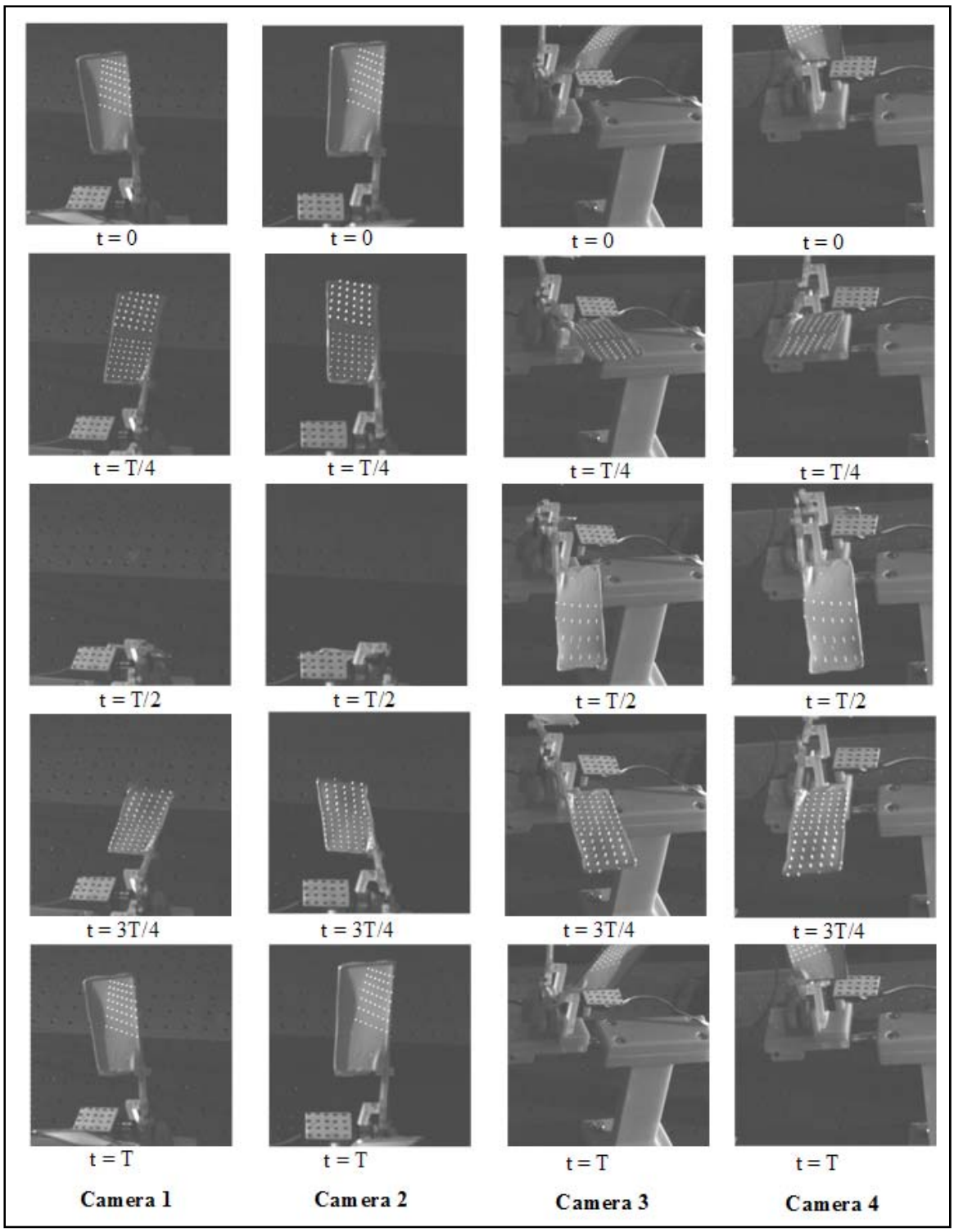


**Figure 63: Images of Straight Tube Frame Wing flapping at 6.2 Hz**

The PhotoModeler 6 software was used to produce 3D position data for each of the laser dots and reference dots in the images analyzed, as discussed in section 3.2.2. Figure 64 shows one particular image along with a 3D plot of the corresponding laser dots and reference grid. The blue dots represent the corners, the green dots represent the reference grid, and the blue x marks represent the laser dots.

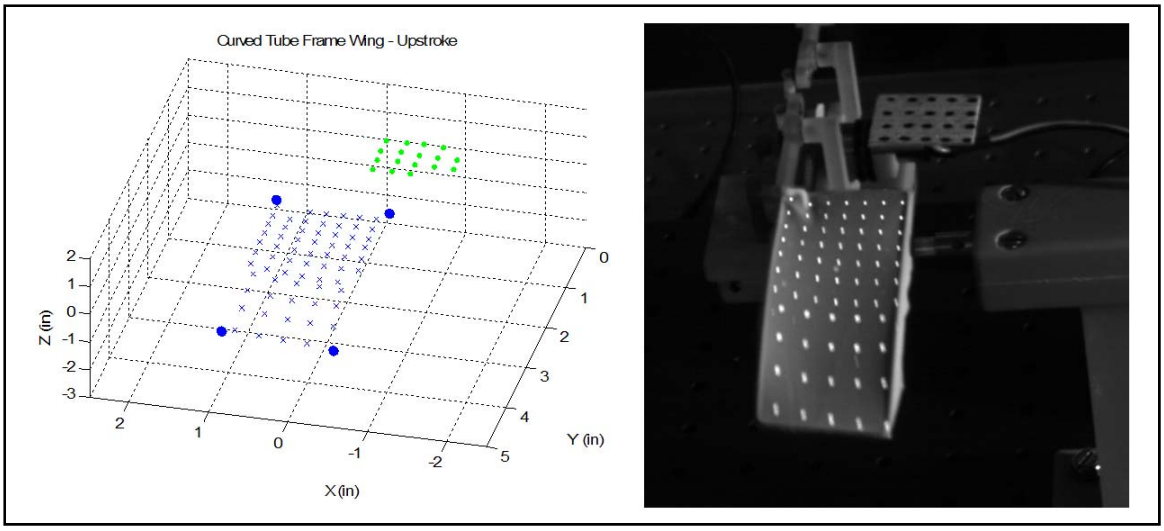


**Figure 64: Example Photogrammetry Results from Curved Tube Frame Wing**

Multiple images from each analyzed section are shown in Figure 65. It is difficult to see from the still images, but when viewing the 3D plots frame-by-frame you will notice that the points representing the laser gird only move significantly in the z direction. This is due to the fact that the lasers are above the wing, shinning down vertically. The only motion of the points in the x and y direction is due to the fact that the grid is not parallel, and the reference grid is not exactly perpendicular to the laser center axis.

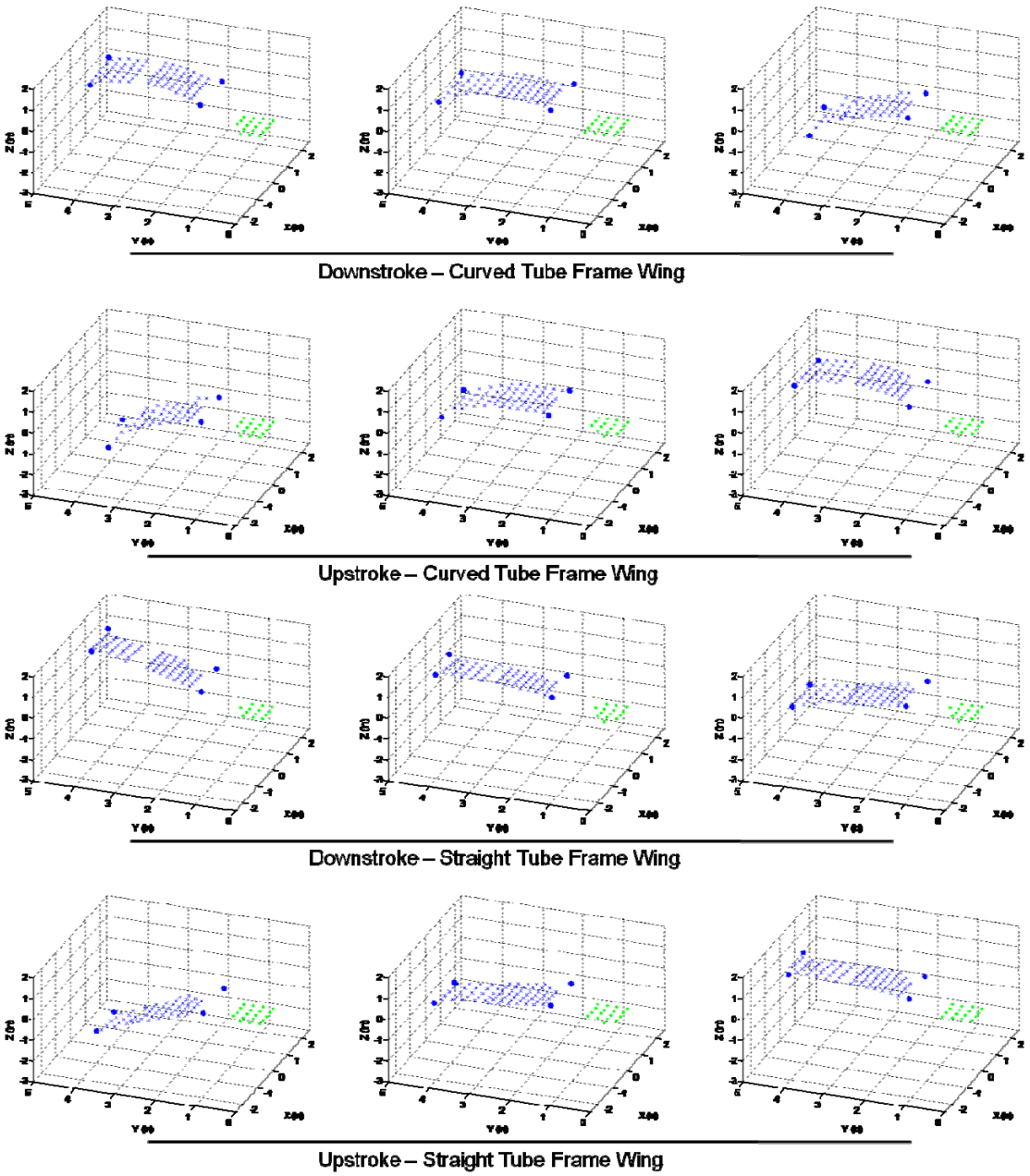


**Figure 65: Photogrammetry Results throughout the stroke for each section analyzed**

Comparison of the straight and the curved tube frame wings when viewed from the front at four different stroke positions during the downstroke is shown in Figure 66. The upstroke comparison is shown in Figure 67. Notice that throughout the downstroke

the curved wing seems to straighten slightly, while during the upstroke it seems to become more curved. This could contribute to the additional lift generation demonstrated by the curved wing. By extending during the downstroke, effectively the wing area perpendicular to the flow is increasing. During the downstroke, the resistance the air provides to the flapping motion is equivalent to lift. Since the wing area perpendicular to the flow is increased, more air must be pushed out of the way, so more lift will be produced. During the upstroke, the opposite occurs; the wing area perpendicular to the flow is decreased causing less negative lift. Since more positive lift is created during the downstroke than negative lift is created during the upstroke, a net lifting force results. These results were demonstrated by Hong and Altman (Hong and Altman ,2006).

To investigate this further, the curvature of the wing was measured by modeling the shape of the wing surface using the radial basis function as discussed in section 3.2.2. An evenly spaced grid of 20 x 40 points along the surface was used, 20 points along the x-direction and 40 points along the y-direction. The distances between each of the points in the rows of 40 were summed to give the distance along the surface. This distance was divided by the straight line distance between the inward and outward most points on the grid. This gave a measure of curvature. Throughout the analyzed portion of the stroke, no significant changes in the curvature were found. For this wing the increased lift likely comes from less drag on upper surface when moving through the air on the upstroke than on the lower surface moving through the air on the downstroke.

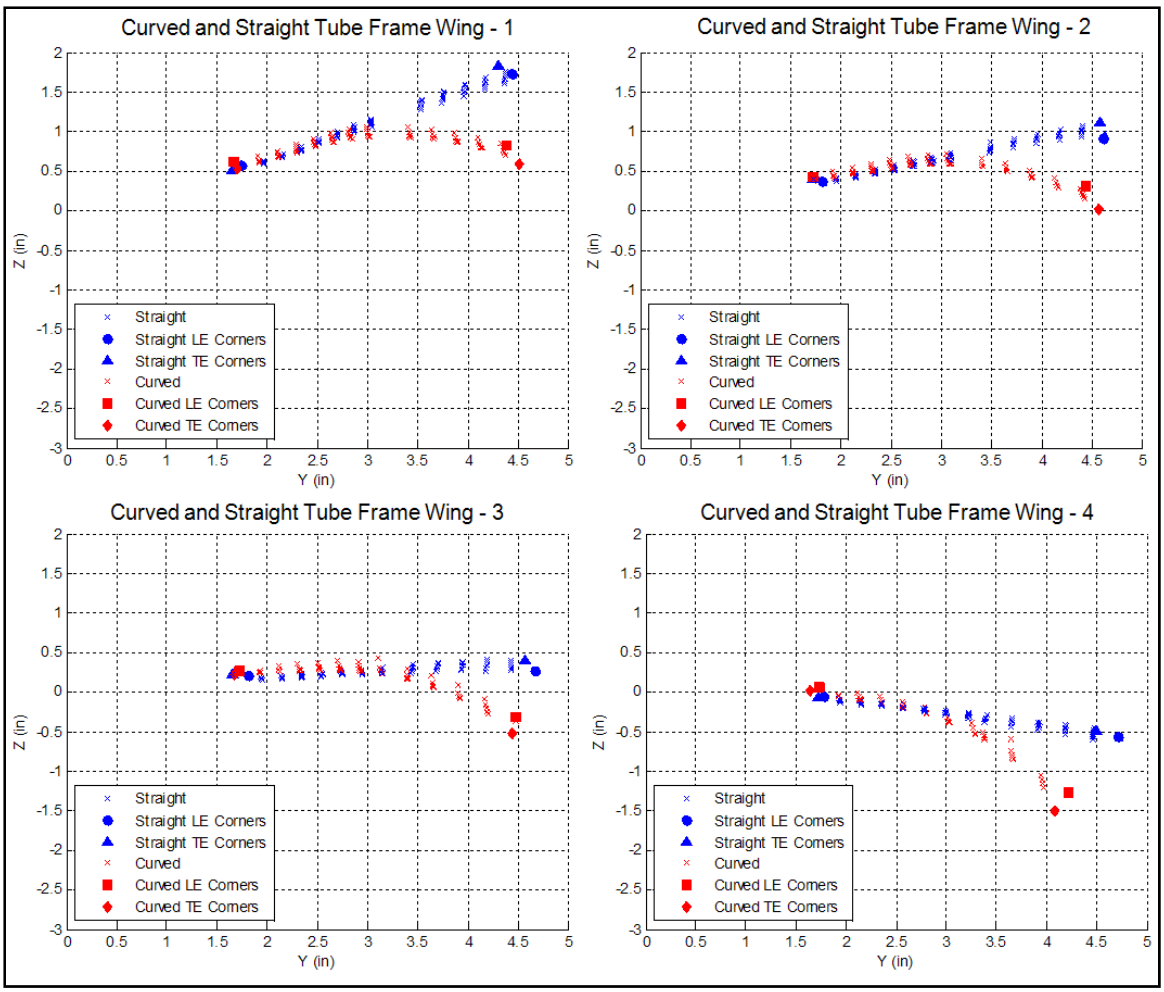


**Figure 66: Front view Comparison of Curved and Straight Tube Frame Wings at four positions during the Downstroke**

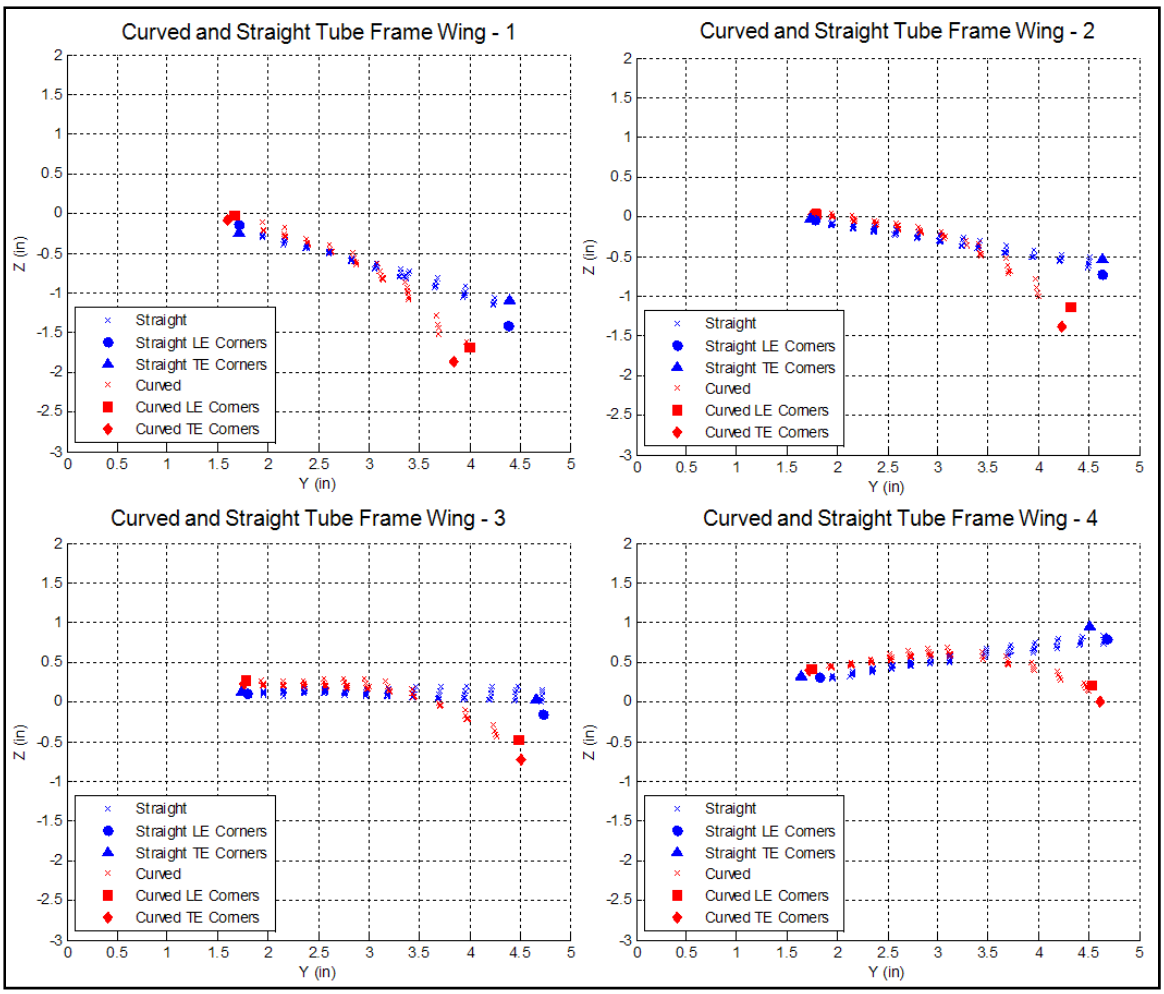


**Figure 67: Front view Comparison of Curved and Straight Wings at four positions during the Upstroke**

As stated, the rigid tube frame wings were initially chosen for analysis because the rigid nature of the wings allowed for easier analysis. Successful analysis led to the desire to look at wings with slightly more flexure. The hybrid straight wing flapping at the same frequency, 6.2 Hz, was analyzed. Images of the wing during flapping, shown in Figure 68, demonstrate that there is noticeable flexure, particularly at the trailing edge of the tip.

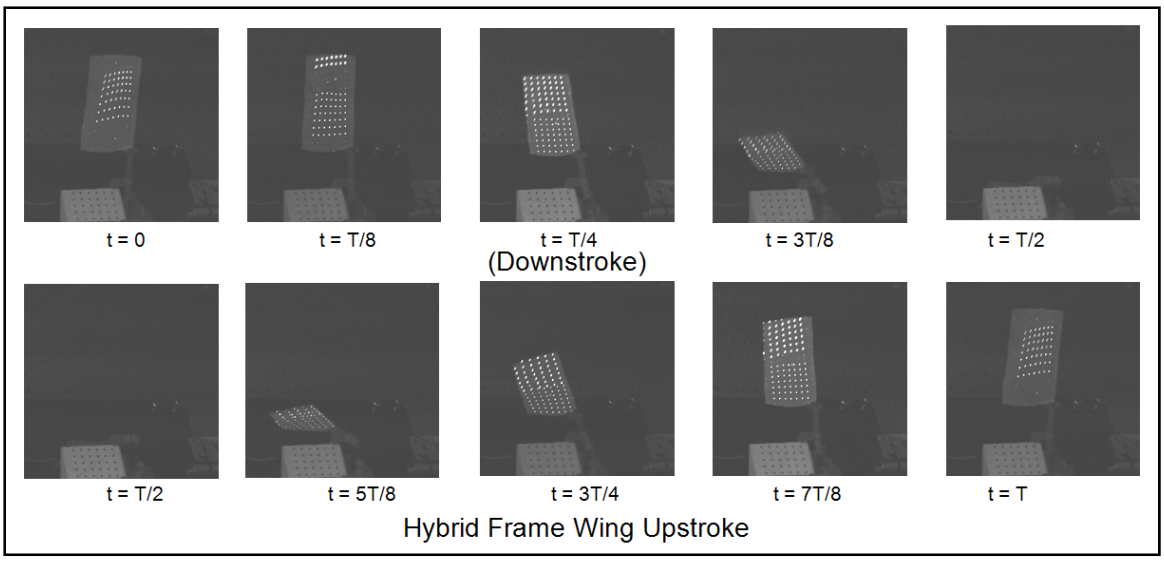


**Figure 68: Hybrid Wing flapping at 6.2 Hz**

Analysis was done on the wing for 30 frames on the upstroke and 30 frames on the downstroke, as shown in Figure 45. A surface was modeled through the wing using the radial basis function method described in section 3.2.2. The rectangular grid used to create the plots of the surface in Figure 69 contains 20 x 40 regularly spaced points on the wing. The boundaries of the grid in the x direction were found by adding 0.1" to the minimum x value on the laser grid and subtracting 0.1" from the maximum x value on the laser grid. The boundaries in the y direction were found by adding 0.2" to the minimum y value on the laser grid and subtracting 0.2" from the maximum y value on the laser grid.

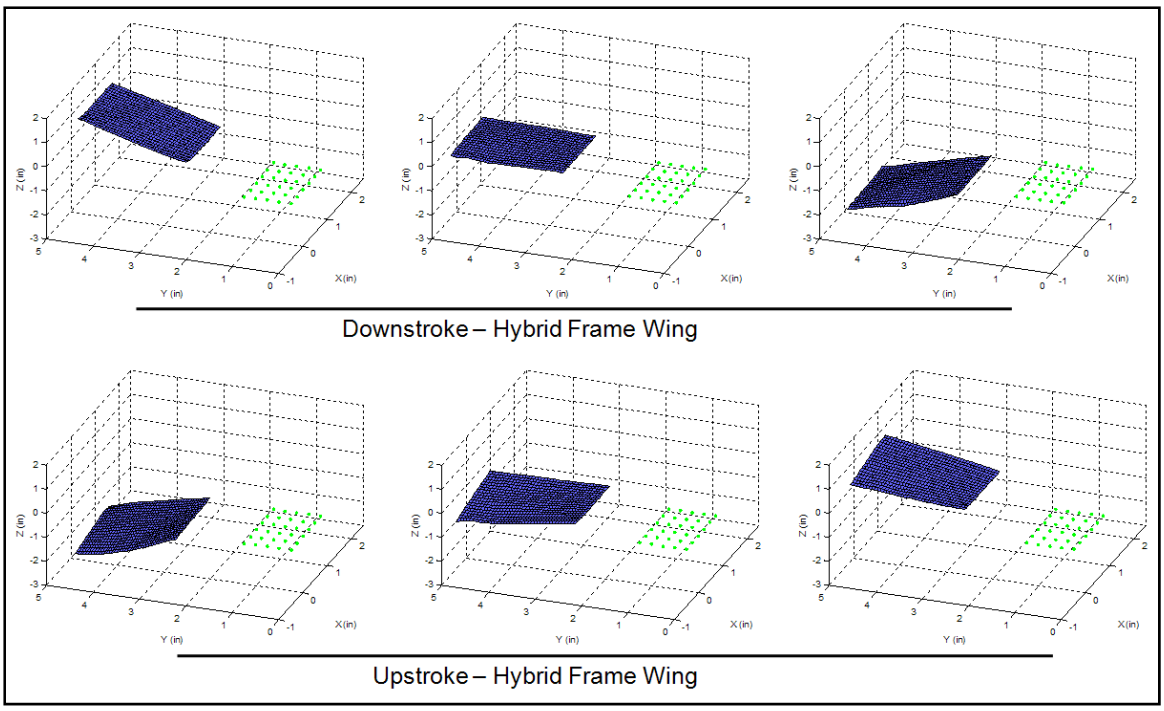


**Figure 69: Surface of Hybrid Wing, blue surface represents the wing surface; green dots represent the reference grid**

Approximations of the pitch angle of the root and the tip of the wing were determined from the surface model. The values of the points on the outermost edge of the rectangular grid were used to determine the tip pitch angle. The points were projected into the x-z plane, ignoring the y component, and the slope of a best fit line was calculated. The arc-tangent of the slope of the best fit line was taken as the tip pitch angle. The root pitch angle was determined in the same way with the innermost edge of the rectangular grid. The twist of the wing is simply the tip pitch angle minus the root pitch angle. This is an approximate method which diminishes in accuracy as the angle of the wing with the horizontal increases.

From Figure 70 and Figure 71 it is evident that the pitching angle and the wing twist is significantly higher during the upstroke than during the downstroke. As

suggested by other research, this flexibility could be what is causing the axial and normal forces shown in Figure 50 (Heathcote, Martin and Gursul, 2004; Ho and others, 2003).

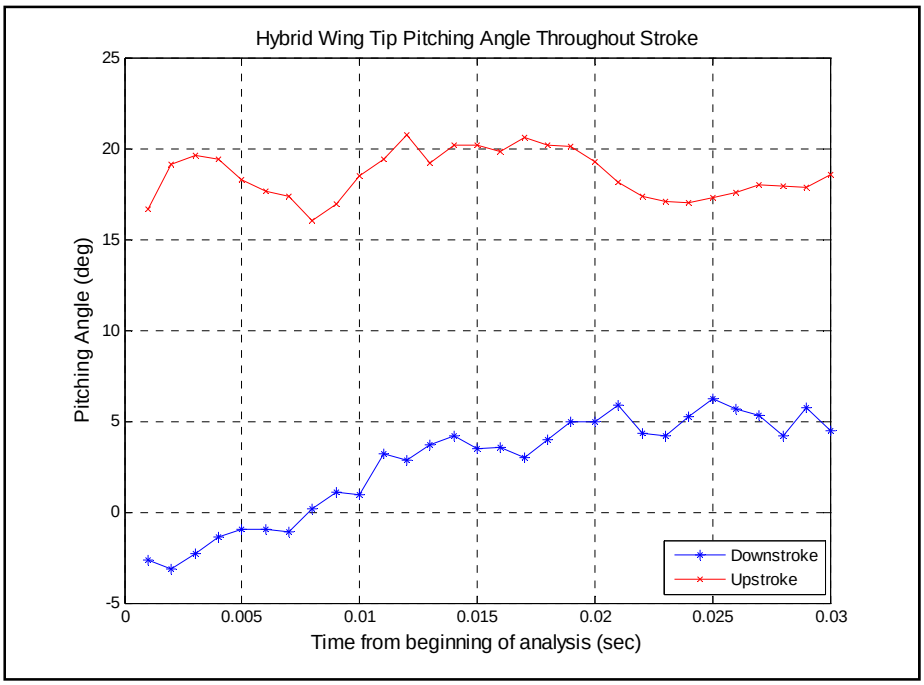


**Figure 70: Pitching Angle throughout Analysis Region for Hybrid Wing**

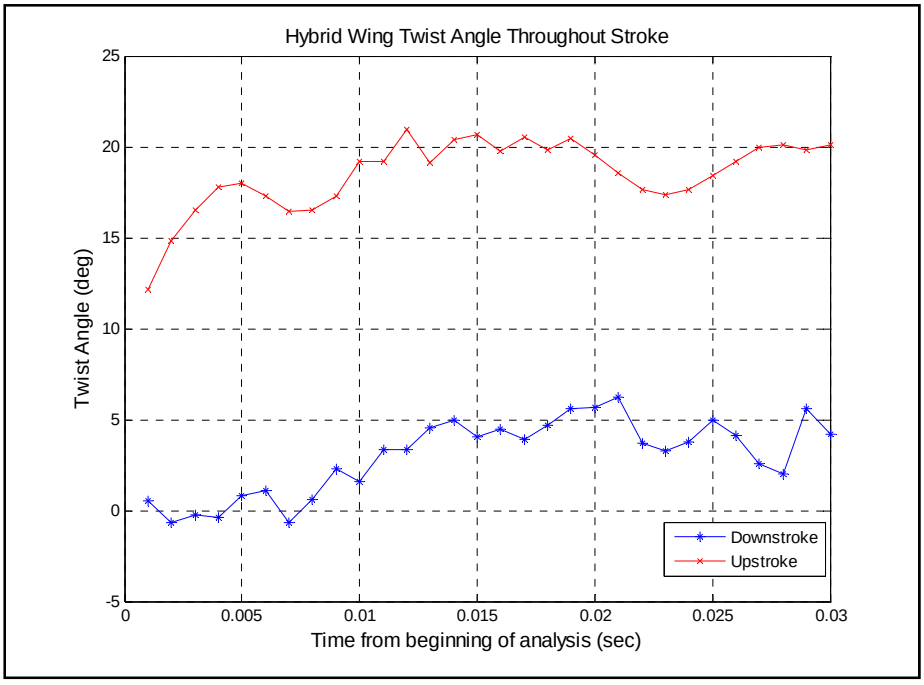


**Figure 71: Wing Twist throughout Analysis Region for Hybrid Wing**

The way the shape of the wing changes throughout the stroke can be difficult to visualize because of the flapping motion of the wing. Stewart and Albertani developed an analysis approach that separates rigid-body-motion of the wing from the deformation of the wing during flapping. They used the VIC system to measure the motion of a flat plate, attached to the inboard section of the wing, during flapping. This motion was used to develop a Homogeneous Transformation Matrix (HTM), which was applied to the motion of the flexible portions of the wing. Applying the HTM to the motion of the flexible portion of the wing yields the deformation without the wing motion (Stewart and Albertani, 2007).

A simplified approach to that of Stewart and Albertani was taken to quantify the deformation of the wing. A surface was modeled for the wing at each point using the RBF method. A linear best fit line, in the y-z plane, was calculated for the points at the forward most edge of the surface grid. Since the leading edge of this particular wing was made of aluminum, there was minimal flexibility in the spanwise direction at the leading edge, therefore the slope of best fit line is a good approximation of the flapping angle. The approximate location of the pivot point for the wing was estimated by averaging the intersection points of the best fit lines from each frame. The pivot point and the flapping angle were used to adjust the y and z values for each grid point to the wing reference frame. The wing reference frame origin is located at the pivot point, and reference frame moves with the wing according to the flapping angle. Finally a surface was modeled to the adjusted grid system. Essentially this method estimates the flapping angle by simulating the wing as a rigid flat plate. The surface in the new reference frame is essentially the difference between the surface formed by a flapping rigid flat plate and the

surface from the actual wing during flapping. Results are shown for one frame during the downstroke and one frame during the upstroke in Figure 72 and Figure 73 respectively. These figures clearly show the difference in pitch and twist between the upstroke and the downstroke. This process isolates the wing deformation by subtracting the flapping angle.

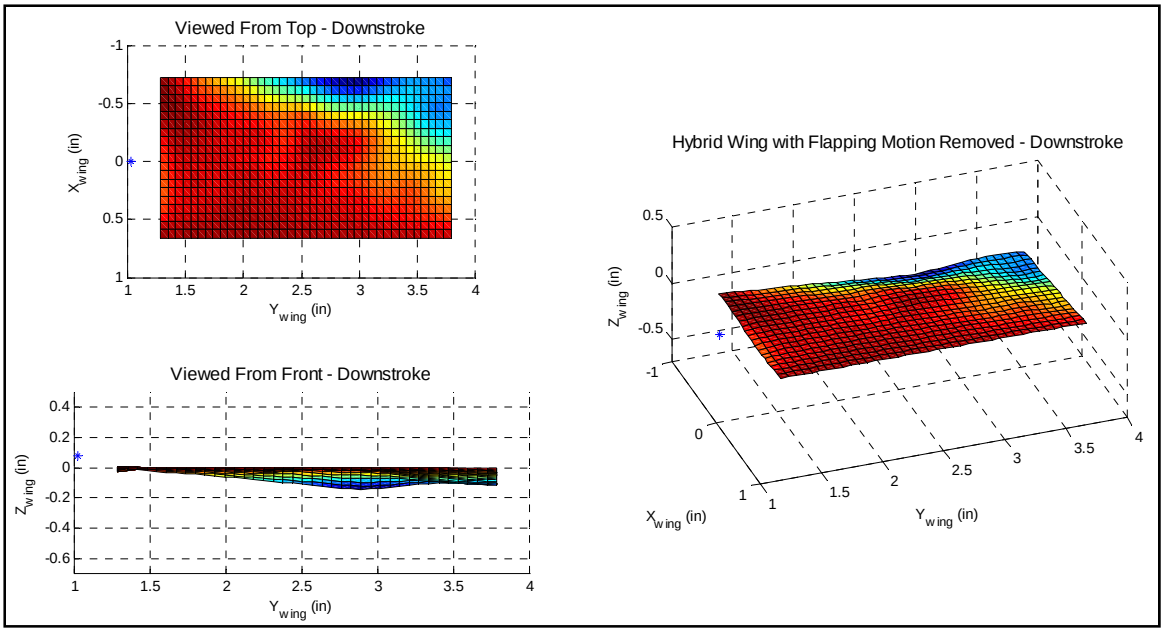


**Figure 72: Deformation of Hybrid Wing during the Downstroke**

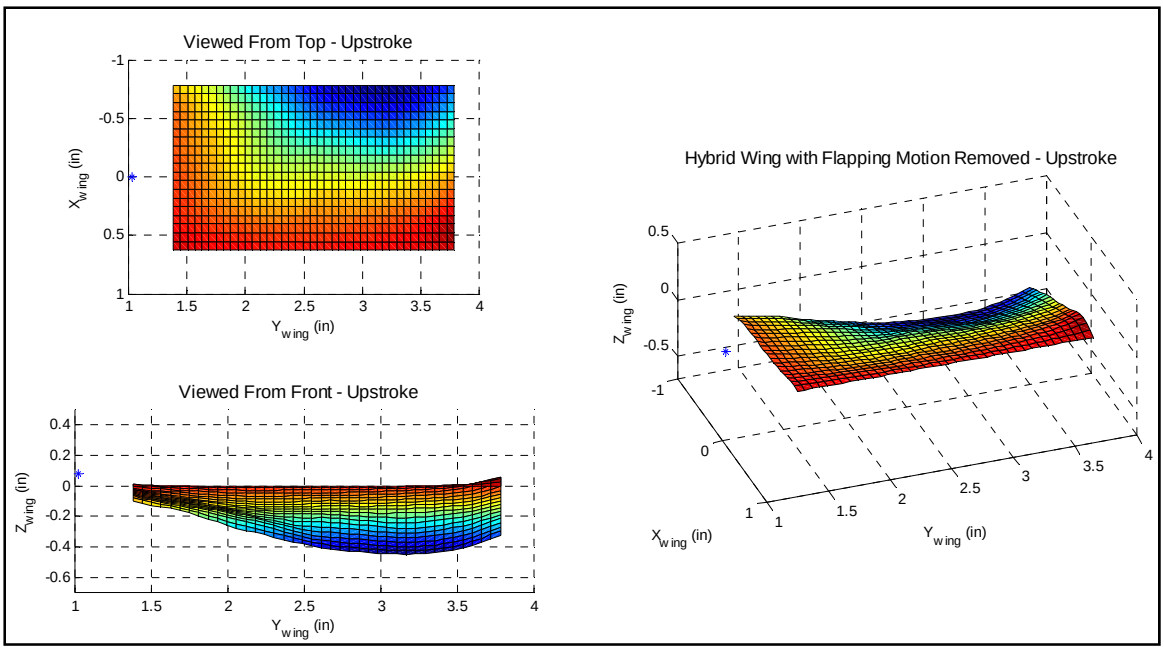


**Figure 73: Deformation of Hybrid Wing during the Upstroke**

Success of the analysis of the hybrid frame wing lead to a desire to relook at the highly flexible wire frame wing. The high speed video of the curved wire frame wing during flapping suggested that the wing was in fact extending on the downstroke and curving inward on the upstroke. To investigate this further, one image set from the downstroke and one image set from the upstroke, representing nearly the same position of the wing root, were analyzed. The results are presented in Figure 74. Figure 74a shows each surface using the radial basis function, while Figure 74b shows a curve that is representative of the leading edge of the surface. The ratio of the length along the surface to the straight line distance between the ends was calculated as a representation of the wing's curvature. The results show that the upstroke had a ratio of 1.095, while the downstroke had a ratio of 1.050. This indicates that the wing is approximately 4% longer on the downstroke than on the upstroke. This could be part of the reason for the

production of normal force, but further investigation would be needed to make any definitive conclusions. This demonstrates the ability to use the laser dot projection photogrammetry method to draw conclusions regarding the reasons for force production.

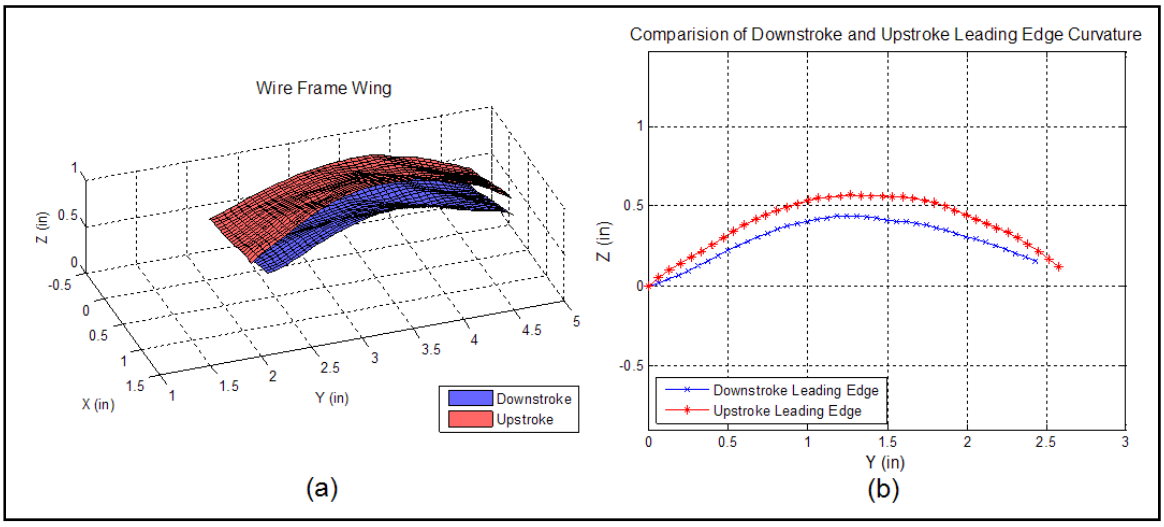


**Figure 74: Analysis of the Curve Wire Frame Wing flapping at 6.2 Hz (a) Surface of Wing (b) Curvature of Leading Edge**

Some synthetic and natural flapping wings utilize a clear membrane. Attempts were made to apply the laser dot projection method to the clear mylar membrane used in experiments conducted by Svanberg. The wing tested is wing number 3 in Figure 75 (Svanberg, 2008). It is has the same dimensions as the other wings tested, but has a carbon fiber frame and clear mylar membrane. The wing was attached to the mechanism, and the lasers were projected onto the surface. Images were taken at 1000 fps while the wing was flapping at approximately 4.7 Hz.

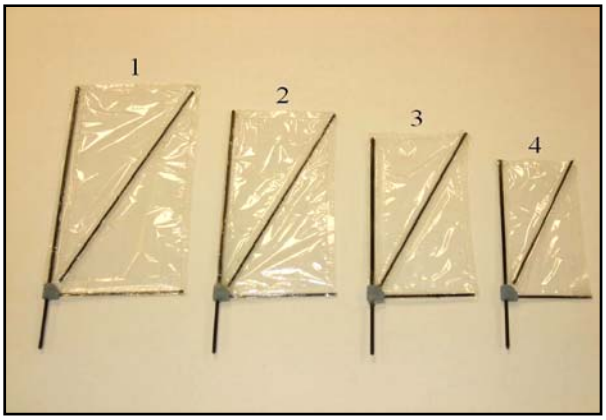


**Figure 75: Carbon Fiber Framed and Mylar Membrane used by Svanberg (Svanberg, 2008)**

Images taken at two different times during flapping are shown in Figure 76. The first set of images represents the image set that shows the best laser dot coverage from cameras 1 and 2, while the second set of images shows the best coverage from cameras 3 and 4. As you can see, only about 20-30 laser dots are visible in each image. Upon closer inspection you will notice that the laser dots visible in one image do not match the laser dots visible in the other image in the set. With minimal dot coverage, and with no matching dots, analysis using photogrammetry would not be possible for this type of membrane material without some kind of systematic improvement. Although the laser dot projection technique shows promise, completely clear membranes may be a case which requires a different method.

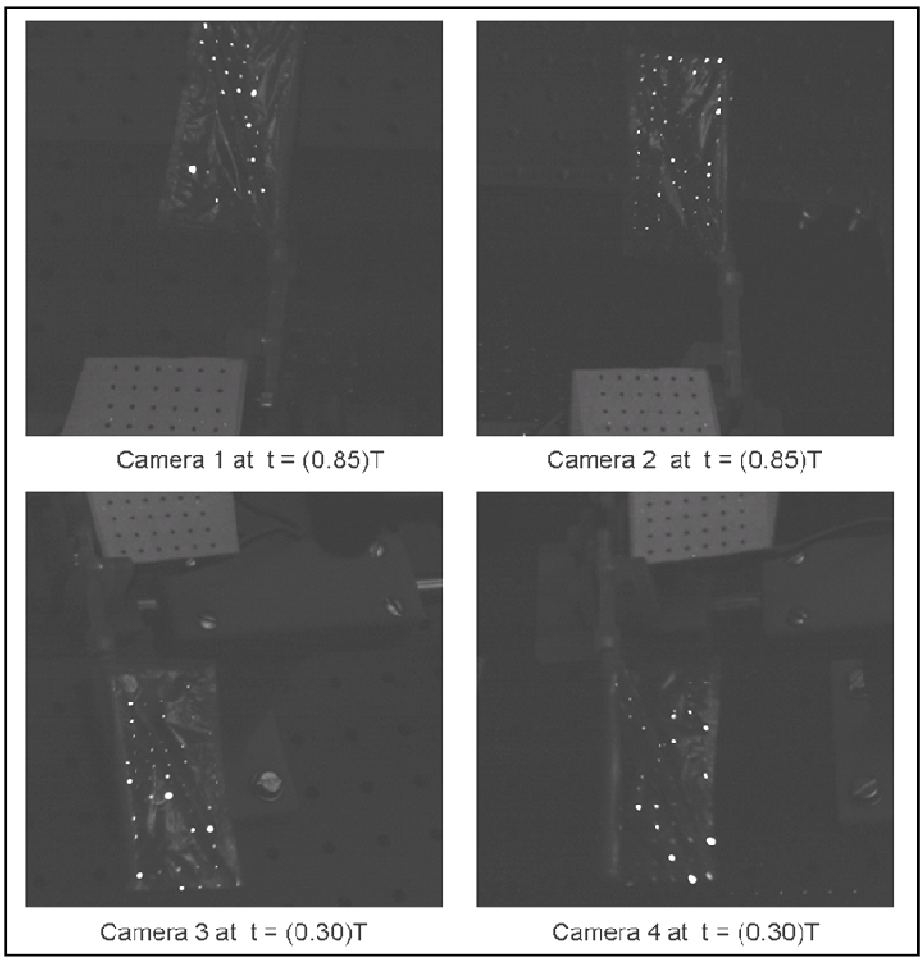


**Figure 76: Images of Laser Grid Projected onto Clear Mylar Membrane Wings at two different locations in the stroke**

# 5. Conclusions

## 5.1 Results Summary and Conclusion

This research aimed to develop tools and methods to be used for the development and analysis of flapping wing MAVs. Methods were developed for studying the forces and moments associated with flapping flight. Laser dot projection photogrammetry was developed as a non-intrusive method of measuring the shape of flapping wings. Wing flexure is often the mechanism for producing the specific forces required for flapping flight. In order to develop wings and mechanisms that produce these forces, the wing flexure required to produce the forces must be measured. It is desired to measure these flexures non-intrusively so that the properties of the wings measured are identical to the properties of the wings used.

Two mechanisms were used in testing. A one degree-of-freedom mechanism capable of flapping only, designed and built by Svanberg, was used for most testing. The two degree-of-freedom mechanism capable of flapping and pitch that was designed by Svanberg was fabricated (Svanberg, 2008). Each mechanism was mounted to a force balance for testing. These mechanisms were designed for use in this bench test set-up, but were not designed to be capable of flight.

A data acquisition system was developed in LabView for measuring the voltage output from the six cannels of a six component force balance capable of detecting very small loads. The normal force, axial force, side force, pitch moment, roll moment, and yaw moment were all measured. Post processing techniques were developed that apply

the interaction matrix to the measurements and convert the voltage to force or moment units.

Two laser diodes were used to project a grid of 14 x 14 laser dots onto flapping wings. Four high speed digital cameras were used to capture images of the laser grid projected on the wings during flapping. PhotoModeler 6 software was used to analyze the images and to produce 3D position data for each of the laser grid dots on the wing.

The majority of tests were performed using the one degree-or-freedom mechanism (Svanberg, 2008; Curtis, Reeder, Svanberg and Cobb, 2009). Different wing types were developed to study the effect of flexibility, and the effect of spanwise curvature on force production, as well as to serve as a test bed for the measurement methods described above. Two different frame materials were used. Aluminum tubing was used to produce a rigid frame, while stainless steel wire was used to produce a flexible frame. Latex material was used for the membrane of the wings. Straight wings and wings with spanwise curvature were tested for each frame material. Wings were flapped at multiple frequencies within each run, and multiple runs were accomplished. Time averaged axial and normal forces were determined for each wing. Force balance data indicate that the flexible wings produce benefits to thrust production while the wings with spanwise curvature produce benefits to lift production when the one degree-of-freedom flapping mechanism was used. The rigid tube frame wings were tested in the two degree-of-freedom mechanism. Pitching the wings such that the angle of attack was always positive generated axial force as anticipated. Force measurement results from both mechanisms were largely as expected based on literature (Ho and others, 2003; Heathcote, Martin, and Gursul, 2004; Hong and Altman, 2006; Isaac, Colozza, and

Rolwes, 2006; Birch and Dickinson, 2003; Jadhav and Massey, 2007; Wilson and Wereley, 2007).

A validation of the laser dot projection method was done by marking the curved tube frame wing with marker dots in a grid with approximately the same spacing as the laser grid. Images were taken from the four cameras of the still wing with the marker dots, then the laser grid was projected on to the wing and images were taken. The two sets of images were analyzed. A radial basis function method was used to model the shape of the wing. The average difference between the two shapes from the two different target types provides assurance that the laser dot projection approach is appropriate.

Laser dot projection images were taken for each of the four wings described above while flapped at 6.2 Hz. Synchronized high-speed imaging showed the highly flexible nature of the wire frame wings. The wire frame straight wing showed flexibility that could have contributed to the increased thrust production. The tube frame wing sets were found to be fairly rigid which accommodated good coverage by the laser dot grid throughout the stroke. The tube frame wing sets were analyzed using PhotoModeler 6 photogrammetry software. The 3D position data gained from the photogrammetry accurately tracked the kinetic motion of the wing.

A hybrid wing was developed in order to demonstrate the ability of the laser dot projection in studying flexibility. The hybrid wing was designed so that the overall planform would remain relatively constant while the trailing edge, particularly at the tip, would deform. The frame was a combination of the aluminum tube and the stainless steel wire used in the first set of wings. Laser dot projection analysis was done on the hybrid wing. A shape was modeled to the wing, and the pitch of the wing throughout the stroke

was investigated. The wing was found to have a pitching angle of approximately 15$^{o}$ higher for the upstroke than for the downstroke. Analysis of two image sets from the curved wire frame wing demonstrated that the flexible wire frame wing was 4% longer during the downstroke as compared to the same location during the upstroke. A simple method of subtracting the flapping motion of the wing from the photogrammetry results in order to view only the shape change of the wing was developed. The ability to study the changing shape of a flexible wing using the laser dot projection photogrammetry method was demonstrated.

## 5.2 Desired Impact of this Research

The information presented here should give an introductory look to some measurement techniques involved in the study of flapping wing models. The techniques presented should give the ability to analyze certain aspects of flapping flight. The dot projection technique gives a tool that can be used to study the shape deformation for both man-made and natural flyers. The Air Force may need to decide between many different avenues for the development of its arsenal of MAVs. Although flight testing will be required, the bench test set-up developed should provide a means of evaluating overall MAV designs. The techniques developed here should provide AFRL with a tool to use in the development and analysis of MAVs for use on the future battlefield.

## 5.3 Recommendations for Future Experimentation

Further work should be done to investigate improvements on the measurement techniques presented. A full dynamic calibration of the force balance should be performed to ensure the accuracy of dynamic measurements and to determine a maximum sample frequency for which data remains accurate. Integrating the force balance data acquisition system with control inputs on a flapping wing mechanism would be the first step in development of control algorithms for MAVs. Developing a method utilizing the data acquisition system to record a real-time measurement of the flapping frequency would provide increased accuracy.

The development of a vacuum chamber should be continued. Force measurements taken in a vacuum provide a means of differentiating inertial forces from aerodynamic forces. High speed images and photogrammetry of wings flapping in a vacuum could also help determine the main factor causing deformation for different wing types.

The laser dot projection technique should be further validated by comparison to other photogrammetry techniques during flapping. Filters could be added to two of the cameras, filtering out the laser light. Traditionally marked targets could be added to the wings. When flapped, two of the cameras capture the marker dots while two capture the laser dots. Photogrammetry could be performed on the images using the two different methods and results compared. Another area for improvement of laser dot projection would be in collimating the laser grid. By shining the grid through a lens, the laser beams making up the grid could be made parallel to one another, decreasing the problem of variable coverage at different locations in the stroke.

Finally, efforts should be made to synchronize the force data acquisition system with the camera system. A method of measuring forces and deformations at the same point in time would be a valuable tool.

# Appendix A: Interaction Matrix

**MODERN MACHINE AND TOOL CO., INC.** **BALANCE AFIT-2 SENSITIVITIES AND INTERACTIONS** **2/23/2005**

Calibration Date: 1/26/05 Calibration done at Modern Machine & Tool Company, Inc.

Full Scale Output and Sensitivity

| COMPONENT | NF | AF | PM | RM | YM | SF |
|---|---|---|---|---|---|---|
| FS LOAD (lb or in-lb) | 4 | 2 | 2 | 4 | 2 | 2 |
| FS OUTPUT (μV/5V) | 10,244 | 5,160 | 5,688 | 6,688 | 5,639 | 5,085 |
| Sens (lb/μV/5V or in-lb/μV/5V) | 3.9049E-04 | 3.8758E-04 | 3.5162E-04 | 5.9812E-04 | 3.5470E-04 | 3.9335E-04 |

Interactions

| COMPONENT | NF | AF | PM | RM | YM | SF |
|---|---|---|---|---|---|---|
| NF | 0 | -9.8200E-04 | -4.5914E-03 | -1.8831E-03 | -1.9326E-03 | -2.6620E-02 |
| AF | 4.0364E-03 | 0 | 5.3239E-03 | -4.9923E-02 | -1.7946E-03 | -1.4880E-03 |
| PM | -1.4210E-04 | -1.3796E-02 | 0 | 4.4506E-03 | -2.8202E-02 | -3.3929E-02 |
| RM | 1.6056E-02 | -2.7212E-02 | 1.1391E-02 | 0 | 3.7648E-03 | -1.0506E-02 |
| YM | -5.6915E-02 | 1.2368E-02 | -3.3847E-02 | -4.0162E-02 | 0 | -1.8475E-02 |
| SF | -2.8098E-02 | 6.3108E-03 | -4.1308E-02 | 2.2944E-02 | 1.4452E-04 | 0 |
| NF^2 | -1.3575E-05 | -1.1569E-03 | -9.4049E-05 | 1.3643E-04 | 2.3149E-05 | 1.6806E-05 |
| NF x AF | 6.6844E-04 | 1.0983E-03 | 9.0964E-04 | -2.4576E-04 | 1.7087E-04 | 8.2732E-05 |
| NF x PM | -3.4434E-05 | 1.5658E-03 | 2.2929E-04 | -1.5111E-04 | 1.6772E-05 | -3.8831E-06 |
| NF x RM | -1.4442E-04 | 2.4386E-05 | -1.4136E-04 | 5.7654E-04 | 1.6126E-03 | 2.3815E-03 |
| NF x YM | 3.3197E-04 | -9.7730E-05 | -7.0785E-06 | 1.0694E-05 | -5.5412E-05 | -1.1832E-04 |
| NF x SF | -5.1739E-04 | 1.1125E-05 | -1.3779E-04 | -2.6345E-04 | 1.6767E-04 | 8.7998E-05 |
| AF^2 | -1.0314E-04 | -2.0009E-04 | -9.3024E-05 | -1.7987E-05 | -8.0068E-05 | -1.6157E-04 |
| AF x PM | -1.4852E-03 | -1.3440E-04 | -1.1694E-03 | 6.3079E-05 | 6.7649E-05 | 1.2623E-04 |
| AF x RM | -1.1651E-05 | -4.4228E-05 | -1.3036E-04 | -1.9758E-04 | 3.2008E-05 | 7.5776E-05 |
| AF x YM | 2.2410E-05 | -2.0896E-04 | -5.0139E-06 | 1.7849E-04 | -1.0735E-03 | -1.6223E-03 |
| AF x SF | 1.3133E-04 | 8.3974E-05 | -2.9065E-04 | 1.5426E-04 | 6.0137E-04 | 5.1139E-04 |
| PM^2 | -6.2911E-05 | 2.5039E-04 | 1.1296E-05 | 1.1556E-04 | 1.0606E-05 | -1.1225E-05 |
| PM x RM | -2.0788E-05 | -1.4530E-05 | -2.1725E-05 | 3.1471E-04 | 8.8043E-04 | 7.9956E-04 |
| PM x YM | 1.4223E-04 | 1.7694E-06 | 4.6984E-04 | -1.0829E-04 | -8.8270E-05 | -7.7069E-05 |
| PM x SF | 1.7598E-05 | 5.3935E-05 | 1.2506E-04 | 5.1264E-05 | -2.8207E-06 | -3.2062E-06 |
| RM^2 | -1.2169E-04 | 1.8673E-03 | -1.3745E-04 | -2.4819E-04 | 1.6052E-05 | 3.1980E-06 |
| RM x YM | -6.4215E-04 | -3.0232E-03 | -7.1087E-04 | 2.3627E-04 | -3.9151E-05 | -7.9646E-05 |
| RM x SF | -2.3835E-03 | -4.8573E-05 | -1.6618E-03 | -1.3475E-06 | 3.5097E-05 | 1.8341E-04 |
| YM^2 | 1.2492E-04 | -1.4548E-04 | 4.6417E-05 | 3.4109E-04 | 9.3630E-07 | -8.5041E-05 |
| YM x SF | 1.4960E-04 | 1.6775E-03 | 7.5723E-05 | -2.4115E-04 | 3.9263E-05 | 2.0146E-04 |
| SF^2 | 8.1356E-05 | -1.0137E-03 | 2.1101E-04 | 2.0419E-04 | 2.1320E-04 | -1.7357E-04 |

Example Units

All interactions are in engineering units

NF interaction on PM is -4.5914E-03 (in-lb. of PM / lb of NF)

## Appendix B: Radial Basis Function Code (Wiens, 2008)

This code determines the weights from the known data points:

train_thin_plate_spline.m

```
function [a, xc]=train_thin_plate_spline(x,y)
%[a, xc]=train_thin_plate_spline(x,y)
%Trains a thin plate spline Radial Basis Function Network.
%Inputs:
% x - network input formatted as N_dimension rows and N_points columns
% y - desired network output. Row vector with N_points columns
%Outputs:
% a - basis function weights.
% x_c - basis function centres formatted as N_dimension rows and
N_centres columns.  This will be equal to x

%Copyright Travis Wiens 2008
% This program is free software: you can redistribute it and/or modify
% it under the terms of the GNU General Public License as published by
% the Free Software Foundation, either version 3 of the License, or
% (at your option) any later version.
%
% This program is distributed in the hope that it will be useful,
% but WITHOUT ANY WARRANTY; without even the implied warranty of
% MERCHANTABILITY or FITNESS FOR A PARTICULAR PURPOSE.  See the
% GNU General Public License for more details.
%
% You should have received a copy of the GNU General Public License
% along with this program.  If not, see <http://www.gnu.org/licenses/>.
%
% If you would like to request that this software be licensed under a
less
% restrictive license (i.e. for commercial closed-source use) please
% contact Travis at travis.mlfx@nutaksas.com

xc=x;%basis function centres
N=size(x,2);%number of points
r=zeros(N);%basis function radii
for i=1:N
    for j=1:N
        r(i,j)=sqrt(sum((xc(:,i)-x(:,j)).^2));
    end
end

E=r.^2.*log(r);%apply thin plate spline RBF
E(find(r==0))=0;%avoid -inf

a=y/E;%use mrdivide to solve system of equations. For large systems it
may
%make more sense to use an online method such as recursive least
squares
%(RLS)
```

This code uses the weights to determine the dependant variable for any combination of independent variables.

sim_thin_plate_spline.m

```
function y_hat=sim_thin_plate_spline(x,x_c,a);
%y_hat=sim_thin_plate_spline(x,x_c,a);
%This simulates a thin plate spline radial basis function.
%Inputs:
% x - network input formatted as N_dimension rows and N_points columns
% x_c - basis function centres formatted as N_dimension rows and
N_centres
%   columns
% a - basis function weights.  Row vector with N_centres columns

%Copyright Travis Wiens 2008
% This program is free software: you can redistribute it and/or modify
% it under the terms of the GNU General Public License as published by
% the Free Software Foundation, either version 3 of the License, or
% (at your option) any later version.
%
% This program is distributed in the hope that it will be useful,
% but WITHOUT ANY WARRANTY; without even the implied warranty of
% MERCHANTABILITY or FITNESS FOR A PARTICULAR PURPOSE.  See the
% GNU General Public License for more details.
%
% You should have received a copy of the GNU General Public License
% along with this program.  If not, see <http://www.gnu.org/licenses/>.
%
% If you would like to request that this software be licensed under a
less
% restrictive license (i.e. for commercial closed-source use) please
% contact Travis at travis.mlfx@nutaksas.com

N_c=size(x_c,2);%number of RBF centres
N_p=size(x,2);%number of points

r=zeros(N_c,N_p);%basis function radii
for i=1:N_c
    for j=1:N_p
        r(i,j)=sqrt(sum((x_c(:,i)-x(:,j)).^2));
    end
end

E=r.^2.*log(r);%thin plate spline radial basis function
E(find(r==0))=0;%avoid -inf

y_hat=a*E;%apply weights
```

## Bibliography


AFRL Air Vehicles Directorate. "M.A.V. Micro Air Vehicles" Informational Video. Produced by General Dynamics Media Communications, Dayton, OH. 2008

Albertani, Roberto. Research Assistant Professor, Department of Mechanical and Aerospace Engineering, University of Florida-REEF, Shalimar FL. Personal Interview. 30 October 2007.

Ansari, S. A., R. Zbikowski, and K. Knowles. "Non-linear unsteady aerodynamic model of insect-like flapping wings in hover. Part 1: methodology and analysis," *Journal of Aerospace Engineering*, 220 Part G: 61-83 (2006).

Ansari, S. A., R. Zbikowski, and K. Knowles. "Aerodynamic modeling of insect-like flapping flight for micro air vehicles," *Progress in Aerospace Sciences*, 42: 129-172 (2006).

Banala, Sai K. and Sunil K. Agrawal. "Design and Optimization of a Mechanism for Out-of-Plane Insect Winglike Motion With Twist," *Journal of Mechanical Design*, 127: 841-844 (July 2005).

Barlow, Jewel B.; William H. Rae, Jr.; and Alan Pope. *Low-Speed Wind Tunnel Testing* (Third Edition). New York: John Wiley & Sons Inc., 1999.

Birch, James M. and Michael H. Dickinson. "The influence of wing-wake interaction on the production of aerodynamic forces in flapping flight," *Journal of Experimental Biology*, 206: 2257-2272 (March 2003).

Carruthers, Anna C., Graham K. Taylor, Simon M. Walker, and Adrian L. R. Thomas. "Use and Function of a Leading Edge Flap on the Wings of Eagles," *Proceedings of the 45th AIAA Aerospace Sciences Meeting and Exhibit.* Reno, Nevada: September 2007.

Chakravarthy, Animesh, Roberto Albertani, Nicholas Gans, and Johnny Evers. "Experimental Kinematics and Dynamics of Butterflies in Natural Flight," *Proceedings of the 47th AIAA Aerospace Sciences Meeting Including The New Horizons Forum and Aerospace Exposition*. Orlando, Florida: Jan. 2009.

Combes, S. A. and T. L. Daniel. "Into Thin Air: Contributions of Aerodynamics and Inertial-Elastic Forces to Wing Bending in the Hawkmoth Manduca Sexta," *Journal of Experimental Biology*, 206: 2999-3006 (18 May 2003).

Curtis, David H., Mark F. Reeder, Craig E. Svanberg, and Richard G. Cobb. "Flapping Wing Micro Air Vehicle Bench Test Set-up," *Proceedings of the 47th AIAA Aerospace Sciences Meeting Including The New Horizons Forum and Aerospace Exposition*. Orlando, Florida: Jan. 2009.

Dudley, Robert. *The Biomechanics of Insect Flight: Form, Function, Evolution.* Princeton: Princeton University Press, 2000.

Ellington, C. P. "The Novel Aerodynamics of Insect Flight: Applications to Micro-Air Vehicles," *Journal of Experimental Biology*, 202: 3439-3448 (15 September 1999).

Ellington, C. P., "The Aerodynamics of Hovering Insect Flight. III. Kinematics," *Philosophical Transactions of the Royal Society, Series B*, 305: 41-78 (1984).

Heathcote, S., D. Martin, and I. Gursul. "Flexible Flapping Airfoil Propulsion at Zero Freestream Velocity," *AIAA Journal*, 42 No. 11: 2196-2204 (November 2004).

Ho, S., H. Nassef, N. Pornsinsirirak, Y. Tai, and C. M. Ho. "Unsteady Aerodynamics and Flow Control For Flapping Wing Flyers," *Progress in Aerospace Sciences*, 39: 635-681 (2003).

Hong, YoungSun and Aaron Altman, "An Experimental Study of Lift Force Generation Resulting from Spanwise Flow in Flapping Wings," *Proceedings of the 44th AIAA Aerospace Sciences Meeting and Exhibit*. Reno, Nevada: September 2006.

Hu, Hui, Anand Gopa Kumar, Gregg Abate, and Roberto Albertani. "An Experimental Study of Flexible Flapping Wings in Flapping Flight," *Proceedings of the 47th AIAA Aerospace Sciences Meeting Including The New Horizons Forum and Aerospace Exposition*. Orlando, Florida: January 2009.

Isaac, K. M., Anthony Colozza, and Jessica Rolwes. "Force Measurements on a Flapping and Pitching Wing at Low Reynolds Numbers," *Proceedings of the 44th AIAA Aerospace Sciences Meeting and Exhibit.* Reno, Nevada: September 2006.

Jadhav, Gautam and Kevin Massey. "The Development of a Miniature Flexible Flapping Wing Mechanism for Use in Robotic Air Vehicle," *Proceedings of the 45th AIAA Aerospace Sciences Meeting and Exhibit*. Reno, Nevada: January 2006.

Jones, T. W. and R. S. Pappa. "Dot Projection Photogrammetric Technique for Shape Measurements of Aerospace Test Articles," *Proceedings of the 40th AIAA Applied Aerodynamics Conference*. Reno, Nevada: January. 2002.

Lunsford, Nathan and Jamey D. Jacob. "High Speed Videogrammetry of Flexible Wings in Flapping Flight," *Proceedings of the 47th AIAA Aerospace Sciences Meeting Including the New Horizons Forum and Aerospace Exposition*. Orlando, Florida: January 2009.

McMichael, J., and Francis, C., "Micro Air Vehicles - Toward a New Dimension of Flight", Technical report, DARPA, 1997.

Pappa, Richard S., Jonathan T. Black, Joseph R. Blandino, Thomas W. Jones, Paul M. Danehy, and Adrian A. Dorrington. "Dot-Projection Photogrammetry and Videogrammetry of Gossamer Space Structures," *Journal of Spacecraft and Rockets*, 40 No. 6: 858-867 (November-December 2003).

Pennycuick, C. J. "Span-Ratio Analysis used to Estimate Effective Lift:Drag Ratio in the Double-Crested Cormorant *Phalacrocorax Auritus* from Field Observations," *Journal of Experimental Biology*, 142: 1-15 (1989).

Press, William H.; Saul A. Teukolsky; William T. Vetterling; and Brian P. Flannery. *Numerical Recipes, The Art of Scientific Computing* (Third Edition). Cambridge: Cambridge University Press, 2007.

Shkarayev, Sergey and Dmitro Silin, "Aerodynamics of Flapping-Wing Micro Air Vehicles," *Proceedings of the 47th AIAA Aerospace Sciences Meeting Including the New Horizons Forum and Aerospace Exposition*. Orlando, Florida: January 2009.

Singh, Beerinder and Inderjit Chopra. "Dynamics of Insect-Based Flapping Wings: Loads Validation," *Proceedings of the 47th AIAA/ASME/ASCE/AHS/ASC Structures, Structural Dynamics, and Material Conference.* Newport, Rhode Island: May 2006.

Singh, Beerinder, and Inderjit Chopra. "Insect-Based Hover-Capable Flapping Wings for Micro Air Vehicles: Experiments and Analysis," *AIAA Journal*, 46, No. 9: 2115-2135 (September 2008).

Stewart, Kelly and Roberto Albertani. "Experimental Elastic Deformation Characterization of a Flapping-Wing MAV Using Visual Image Correlation," *Proceedings of the Critical Technology Development for Micro Munition Vehicles TTCP Meeting*. Aberdeen Proving Ground, Maryland: 16-17 October 2007.

Svanberg, Craig E. *Biometric Micro Air Vehicle Testing Development and Small Scale Flapping Wing Analysis*. MS Thesis, AFIT/GAE/ENY/08-M27. Graduate School of Engineering and Management, Air Force Institute of Technology (AU), Wright-Patterson AFB OH, March 2008 (ADA478940).

Wiens, Travis. "Thin Plate Spline Network with Radiohead Example," MatLab script available at <www.mathworks.com>. 22 July 2008

Wilson, Nicholas L. and Norman Wereley. “Experimental Investigation of Flapping Wing Performance in Hover”, *Proceedings of the 48th AIAA/ASME/ASCE/AHS/ASC Structures, Structural Dynamics, and Materials Conference*. Honolulu, Hawaii: 23-26 April 2007.

Zbikowski, Rafal, Cezary Galinski, and Christopher B. Pedersen. “Four-Bar Linkage Mechanism for Insectlike Flapping Wings in Hover: Concepts and an Outline of Its Realization,” *Journal of Mechanical Design*, 127: 817-824 (July 2005).

# REPORT DOCUMENTATION PAGE

*Form Approved*
*OMB No.0704-0188*



| **1. REPORT DATE** *(DD-MM-YYYY)* | **2. REPORT TYPE** | **3. DATES COVERED** *(From – To)* |
|---|---|---|
| 26-03-2008 | Master's Thesis | Sep 2008 – Mar 2009 |

**4. TITLE AND SUBTITLE**

Laser Dot Projection Photogrammetry and Force Balance Measurement Techniques For Flapping Wing Micro Air Vehicles

**5a. CONTRACT NUMBER**

**5b. GRANT NUMBER**

**5c. PROGRAM ELEMENT NUMBER**

**6. AUTHOR(S)**

Curtis, David H., First Lieutenant, USAF

**5d. PROJECT NUMBER**

**5e. TASK NUMBER**

**5f. WORK UNIT NUMBER**

**7. PERFORMING ORGANIZATION NAMES(S) AND ADDRESS(S)**
Air Force Institute of Technology
Graduate School of Engineering and Management (AFIT/EN)
2950 Hobson Street, Building 642
WPAFB OH 45433-7765

**8. PERFORMING ORGANIZATION REPORT NUMBER**

AFIT/GAE/ENY/09-M05

**9. SPONSORING/MONITORING AGENCY NAME(S) AND ADDRESS(ES)**
Air Force Research Labs Air Vehicles Directorate Structures Division
Attn: Parker, Gregory H. Maj
2210 Eighth St.
WPAFB, OH 45433 (Gregory.Parker@WPAFB.AF.MIL)

**10. SPONSOR/MONITOR'S ACRONYM(S)**
AFRL/RBSD

**11. SPONSOR/MONITOR'S REPORT NUMBER(S)**

**12. DISTRIBUTION/AVAILABILITY STATEMENT**
APPROVED FOR PUBLIC RELEASE; DISTRIBUTION UNLIMITED.

**13. SUPPLEMENTARY NOTES**

**14. ABSTRACT**

The purpose of this research was to develop testing methods capable of analyzing the performance of a miniature flapping-wing mechanism that can later be adapted to a flapping wing micro air vehicle (MAV). A previously designed and built flapping only mechanism was used for testing, while a previously designed flapping and pitch mechanism was fabricated utilizing an Objet Eden 500V 3-dimensional printer and its operation demonstrated. The flapping mechanism was mounted on a six component force balance. Force and moment data were collected for a variety of wing sets at different flapping frequencies. The testing was conducted using wings composed of aluminum tubing and/or stainless steel wire for frame material, and thin latex as membrane material. The normal and axial force averages were taken with the force balance and compared. The axial force measurement was verified using an air bearing table and a load cell as a secondary means of measurement. Time accurate force data was also taken. A non-intrusive photogrammetry method using laser dot projection was developed allowing for the shape of the wing during flapping to be measured. The result was that approximately 98 data points representing wing shape and orientation were collected at 1000 Hz. Comparisons were made between laser dot projection photogrammetry and a more a traditional method using potentially intrusive marked targets for photogrammetry, with good correspondence. Differences in force data were then analyzed with the insight gained regarding wing shape. This research demonstrates the capability to study the forces and moments involved in flapping flight as well as shape changing of wings during flapping flight.

**15. SUBJECT TERMS**
MAV, Flapping Wing, MAV Testing, Micro Air Vehicle, Photogrammetry, Laser Dot Projection

| **16. SECURITY CLASSIFICATION OF:** | | | **17. LIMITATION OF ABSTRACT** | **18. NUMBER OF PAGES** | **19a. NAME OF RESPONSIBLE PERSON** |
|---|---|---|---|---|---|
| **1. REPORT** | **2. ABSTRACT** | **c. THIS PAGE** | | | Dr. Mark F. Reeder |
| **U** | **U** | **U** | **UU** | 135 | **19b. TELEPHONE NUMBER** *(Include area code)* (937) 255-3636, x4530 e-mail: mark.reeder@afit.edu |

**Standard Form 298 (Rev. 8-98)**
Prescribed by ANSI Std. Z39-18